New Tools for Studying Nanoscale Electrochemical Phenomena

Christopher G. Gunderson

A dissertation

submitted in partial fulfillment of the

requirements for the degree of

Doctor of Philosophy

University of Washington

2017

Reading Committee:

Bo Zhang, Chair

Robert Synovec

Bruce Robinson

Program Authorized to Offer Degree:

Chemistry

University of Washington

Abstract

New Tools for Studying Nanoscale Electrochemical Phenomena

Christopher G. Gunderson

Chair of the Supervisory Committee:

Professor Bo Zhang

Department of Chemistry

This dissertation focuses primarily on the fabrication of micro and nanoscale electrochemical structures such as electrodes, electrode arrays, and nanopores. It also discusses the use of these tools in studying nanoscale electrochemical processes such as geometric considerations in redox molecule diffusion to nanoscale electrodes, confined diffusion within electrode arrays, nanoparticle transport, and emulsion droplet transport and agglomeration. There is an introduction to electrochemistry followed by considerations to make when studying electron transfer at the nanoscale using voltammetric and amperometric measurements.

Chapter 2 discusses three types of new nanoelectrodes that have been developed. These nanoelectrodes are different from previous nanoelectrodes in their materials and fabrication methods. Chapter 3 introduces the reader to electrode arrays and their properties. A new way of fabricating microelectrode arrays with high density and a nearly 100% success rate in terms of electrode activity is presented. In Chapter 4 a new electrochemical imaging technique developed

in our lab is introduced. This new technique requires bipolar electrode arrays, new variants of which are fabricated using several methods which are discussed. Chapter 5 moves away from Faradaic current measurements toward ionic current measurements of nanoparticles. Emulsified oil droplets are monitored with ionic current measurements and fluorescence imaging to reveal their interactions at a nanopore. In Chapter 6 a new method for fabricating nanopores is outlined along with substantial experiments and finite element simulations to describe their properties. The ability of this new nanopore to measure nanoparticles is illustrated through resistive-pulse sensing. These new nanopores are compared with another type of nanopore using both experiment and simulation.

Table of Contents

List of Schemes

List of Figures

Acknowledgements

I would first like to thank my advisor, Professor Bo Zhang, for his guidance through my graduate career. He has helped me to learn about nanoscale electrochemistry, scientific research, and also about persistence and communication. I would also like to thank my committee members, Professor Rob Synovec, Professor Bruce Robinson, and Professor Lih Lin for their support. I am also grateful to the department for supporting me through my graduate career and granting me the Excellence in Chemistry Graduate Fellowship Award and the Basil G. and Gretchen F. Anex Endowed Fellowship in Chemistry.

I am grateful to Stephen Percival for his guidance through graduate school, and I learned a considerable amount about electrochemistry, electrocatalysis, and microfabrication from him. He was a patient teacher and a mentor to everyone in lab, including me. I would also like to extend gratitude toward Marissa Wood for her company in lab and help with nanopores. Finally, I would like to thank Chadd Armstrong for company and for being genuinely interested in the pursuit of science regardless of assigned credit and other formalities associated with professional science. I learned a lot about programming, signal analysis, and instrumental analysis from working with Chadd. I would also like to thank him for convincing me to take a class in programming that I thoroughly enjoyed and helped my research considerably, however late in my graduate career it may have been.

Chapter 1. Introduction

1.1 Electrochemistry

Electrochemistry is the study of chemical reactions involving charge transfer, typically at a solid-liquid interface such as a metal electrode in an electrolyte solution. The study of electrochemistry is pertinent to many subfields such as energy storage,[1] sensing,[2,3] and synthesis.[4] In recent years, electrochemistry has shrunk to the nanoscale.[5] This dissertation focuses on the sensing aspect of electrochemistry at the nanoscale. New nanoelectrodes, electrode arrays, and nanopores are discussed and their properties outlined.

When a metal electrode is placed in an electrolyte solution an electrical double layer forms at the electrode-solution interface.[6] This double layer consists of an inner layer, called a Stern layer, and an outer layer, called a diffuse layer.[7] For a positively charged electrode the Stern layer is a monolayer of anions coating the electrode surface with successive layers having decreasing concentrations of anions. This ion gradient decreases exponentially into the diffuse layer toward the bulk layer where the gradient is zero. When the metal electrode is polarized the ion gradient within the double layer shifts. The concentration of ions within the double layer causes the voltage applied to the electrode to be essentially confined to the electrode surface. The degree to which the voltage enters solution is determined by the concentration of electrolyte. A high concentration of electrolyte creates a higher gradient which lowers the penetration of the voltage into solution. Theoretically this is known as the Debye length with the voltage falling to $1/e$, or approximately 37%, of its value within a single Debye length. A typical Debye length for a 100 mM salt solution is 1 nm.[8] With a voltage of 1 V applied to the electrode this creates an electric field approaching 10^9 V/m at the electrode surface.

Electrochemical cells require at least two electrodes. These two electrodes are called the reference electrode and the working electrode. At each electrode an electrochemical half-reaction will occur. The reference electrode is of constant composition and serves as a reference to which other electrochemical half-reactions occur. When a threshold voltage is approached and crossed, both electrochemical half-reactions occur simultaneously.

Electrochemical reactions in solution are typically studied using a two or three electrode system consisting of a working electrode, reference electrode, and a counter electrode. The working electrode is where the electrochemical reaction of interest occurs. It is polarizable within a certain voltage range, called a potential window. Outside of this range reactions involving the electrode material can occur, such as the oxidation of the metal. There is also a potential window of the electrolyte solution used where breakdown reactions such as water splitting occurs. The reference electrode is the electrode to which the potential of the working electrode is referenced. Knowing the voltage applied to the working electrode is meaningless without knowing the electrochemical reaction occurring at the reference electrode which completes the electrochemical cell. The counter electrode, sometimes called an auxiliary electrode, is the electrode through which most of the current flows. This electrode is typically made of a noble metal, such as gold or platinum, to prevent the counter electrode from losing material quickly through reactions. The environment of the electrochemical reaction at the reference electrode is preserved by passing most of the current through the counter instead of the reference. An instrument which controls this three-electrode system is called a potentiostat and controls the potential between the working and reference electrodes by passing current through the counter electrode. In the case of a two-electrode system, the electrode other than the working electrode is effectively the reference and

counter electrode. This is an effective alternative in low-current electrochemistry where there is little risk of altering the composition of the reference electrode.[6]

1.2 Ultramicroelectrodes

Ultramicroelectrodes (UMEs) are typically defined as electrodes with a critical dimension of 25 µm or less and have many important analytical and practical advantages over larger electrodes. The concept of the double layer and Debye length is increasingly important as the dimensions of an electrode is shrunk. As the dimensions of the electrode approach that of the double layer new phenomena occur, such as ion enrichment within the double layer,[9,10] electrode passivation from effects such as bubble formation,[11] as well as enhanced sensitivity to nanoparticle blocking[12] and enhancement[13] of Faradaic current at the electrode. As the dimension of an electrode approaches the dimension of the diffusion layer there is also enhanced mass transport to the electrode surface.[14] As a result, UMEs reach a diffusion-limited state faster than their larger counterparts. Faster electron transfer rates can be measured when mass transport is no longer limiting at low scan rates. Additionally, UMEs have smaller capacitive and Faradaic currents. This allows UMEs to be used in higher resistance solutions because of a smaller potential drop and they do not require a counter electrode, as the currents passed are small enough to not significantly alter the reference electrode. Smaller capacitive currents resulting from a smaller electrode-solution interface permit higher scan rates to be used.[14]

The most common geometry of a UME is that of a planar disk in an insulator. Typically, this is a platinum wire that has been sealed in a glass capillary and pulled to a fine tip. The glass is then polished back to reveal the sharp tip of the pulled wire, which can be as small as a few nanometers. New ways of making UMEs more consistently, and from materials other than platinum, are outlined in Chapter 2.

The difference in diffusion profiles at a UME from a typical macroelectrode give rise to different voltammetric responses. Most importantly, the current-voltage response appears as a sigmoid shape as the diffusion changes from planar to radial.[14] Because of their small dimensions and unique diffusion properties UMEs have opened up the field of electrochemical imaging.[2,15]

1.3 Electrode Arrays

Another common tool in the electrochemist's arsenal is the electrode array. Arrays of ultramicroelectrodes can exhibit several diffusion profiles based on the length of the voltage applied to the array.[16] Electrode arrays can be constructed from tens of thousands of UMEs and share properties between UMEs and macroelectrodes. Electrode arrays generate the Faradaic response of a larger electrode of the same geometric area as the array.[17,18] This lends them to use in measuring low concentrations of analyte species that do not produce a large signal with a single UME. Signal-to-noise during voltammetry is improved with an array because Faradaic current scales with the geometric dimensions of the array while capacitive current scales with electroactive area.[19] These properties of electrode arrays have caused their extensive use for applications including the testing of biologically important molecules[20,21] and heavy metals in polluted water.[22,23] Individually-addressable UME arrays are particularly useful for monitoring electrochemically active events, such as secretion of neurotransmitters from a single cell.[24] A new fabrication procedure for electrode arrays is discussed in Chapter 3. In Chapter 4, a new type of electrode array for electrochemical imaging is discussed with various methods of fabrication showcased.

1.4 Nanopores

An electrochemical oxidation is the removal of an electron from a chemical species in solution at one electrode. In a two-electrode setup this half-reaction is coupled with the

simultaneous introduction of an electron at the other electrode. The charge in solution is balanced overall, however the charge is spatially balanced through the movement of ions in the solution from one electrode to the other. This ionic current is typically uninteresting as it is not the limiting process in conventional electrochemistry. However, one can make this ionic current the limiting factor by greatly increasing the size of both electrodes and introducing a solution bottleneck, such as a pore of small dimensions approaching the nanoscale, between the two electrodes through which all ionic current must pass. In this situation, anything that perturbs the flow of ions at this bottleneck will be evident in an electrical recording of the ionic current over time. Particles and molecules entering the pore will displace the electrolyte solution, causing a transient increase in the resistance of the pore. The height and length of this resistive-pulse reveals properties of either the particle or pore.[25] A pore of known size can be used for sizing passing particles of unknown size just as a particle of known size and composition reveals information about the pore such as the electric field distribution or pore size. These principles have been used in the size measurement of micro and nanoparticles in a device known as a Coulter counter.[26] Recently, as biological nanopores have come into use they have also been used for the identification of individual nucleobases of DNA molecules translocating through a protein ion channel.[27] In Chapter 5 there is a new application of resistive-pulse sensing toward emulsion agglomeration.

When the ionic current is constricted to a nanopore there becomes an intense electric field concentrated to the nanopore orifice. This electric field is geometry dependent and can approach 10^6 V/m as determined through finite element simulations.[28] The properties of the nanopore are central to its sensing capabilities. The size of the pore dictates the maximum particle size allowed through the pore while also determining the ratio of electrolyte solution displaced from a translocating particle to the overall pore solution volume. The nanopore's surface charge is

determined by material and pH, an important consideration at the nanoscale because of double layer effects interacting with translocating particles. Additional phenomena arise such as ionic current rectification.[29]

The concentrated electric field interacts with nanoparticles that are near and within the nanopore. Two main effects arise from this; electroosmosis and electrophoresis, in addition to Brownian motion outside the confines of the concentrated electric field. A nearby nanoparticle, with its surface charge and zeta potential, is acted upon by these forces within the electric field. One can obtain information about the nanoparticle such as shape, [28] electrophoretic mobility, [30] charge, [31] zeta potential,[32] and size.[33] Chapter 6 finishes the dissertation with the outline of a new type of glass nanopore sensor. Its advantages over conventional nanopores in terms of geometric variation and nanoparticle characterization are demonstrated through experiment and simulation.

1.5 References

(1) Goodenough, J. B.; Park, K.-S. *J. Am. Chem. Soc.* **2013**, *135*, 1167-1176.

(2) Liu, H.-Y.; Fan, F.-R. F.; Lin, C. W.; Bard, A. J. *J. Am. Chem. Soc.* **1986**, *108*, 3838-3839.

(3) Guerrette, J. P.; Percival, S. J.; Zhang, B. *J. Am. Chem. Soc.* **2013**, *135*, 855-861.

(4) Moeller, K. D. *Tetrahedron* **2000**, *49*, 9527-9554.

(5) Oja, S. M.; Fan, Y. S.; Armstrong, C. M.; Defnet, P.; Zhang, B. *Anal. Chem.* **2016**, *88*, 414-430.

(6) Bard, A. J.; Faulkner, L. R. Electrochemical Methods, 2nd ed.; John Wiley & Sons: New York, 2001.

(7) P. H. Rieger, Electrochemistry, p. 215-223, Chapman & Hall, Inc., New York, (1994).

(8) Yusko, E. C.; An, R.; Mayer, M. *ACS Nano*, **2010**, *4*, 477–487.

(9) Lu, J.; Zhang, B. *Anal. Chem.* **2017**, *89*, 2739-2746.

(10) Chen, Q.; McKelvey, K.; Edwards, M. A.; White, H. S. *J. Phys. Chem. C* **2016**, *120*, 17251-17260.

(11) Luo, L.; White, H. S. *Langmuir* **2013**, *29*, 11169-11175.

(12) Boika, A.; Thorgaard, S. N.; Bard, A. J. *J. Phys. Chem. B* **2013**, *117*, 4371-4380.

(13) Xiao, X. Y.; Bard, A. J. *J. Am. Chem. Soc.* **2007**, *129*, 9610-9612.

(14) Heinze, J. *Angew. Chem. Int. Ed. Engl.* **1993**, *32*, 1268-1288.

(15) Bard, A. J.; Fan, F.-R. F.; Kwak, J.; Lev, O. *Anal. Chem.* **1989**, *61*, 132-138.

(16) Davies, T. J.; Ward-Jones, S.; Banks, C. E.; del Campo, J.; Mas, R.; Muñoz, F. X.; Compton, R. G. *J. Electroanal. Chem.* **2005**, *585*, 51–62.

(17) Penner, R. M.; Martin, C. R. *Anal. Chem.* **1987**, *59*, 2625–2630.

(18) Amatore, C.; Savéant, J. M.; Tessier, D. *J. Electroanal. Chem.* **1983**, *147*, 39–51.

(19) Menon, V. P.; Martin, C. R. *Anal. Chem.* **1995**, *67*, 1920–1928.

(20) Moretto, L. M.; Pepe, N. Ugo, P. *Talanta* **2004**, *62*, 1055–1060.

(21) Ugo, P.; Pepe, N.; Moretto, L. M.; Battagliarin, M. J. *Electroanal. Chem.* **2003**, *560*, 51–58.

(22) Feeney, R.; Kounaves, S. P. *Anal. Chem*. **2000**, *72*, 2222–2228.

(23) Jena, B. K.; Raj, C. R. *Anal. Chem*. **2008**, *80*, 4836–4844.

(24) Abe, H.; Ino, K.; Li, C. Z.; Kanno, Y.; Inoue, K. Y.; Suda, A.; Kunikata, R.; Matsudaira, M.; Takahashi, Y.; Shiku, H.; Matsue, T. *Anal. Chem*. **2015**, *87*, 6364–6370.

(25) Luo, L.; German, S. R.; Lan, W.-J.; Holden, D. A.; Mega, T. L.; White, H. S. *Annu. Rev. Anal. Chem.* **2014**, *7*, 513-535.

(26) Coulter, W. H. *Means for Counting Particles Suspended in a Fluid* **1953**, US Patent No. 2656508.

(27) Bayley, H.; Martin, C. R. *Chem. Rev.* **2000**, *100*, 2575-2594.

(28) Lan, W.-J. Holden, D. A.; Zhang, B.; White, H. S. *Anal. Chem.* **2011**, *83*, 3840-3847.

(29) Wei, C.; Bard, A. J. *Anal. Chem.* **1997**, *69*, 4627-4633.

(30) Qiu, Y.; Hinkle, P.; Yang, C.; Bakker, H. E.; Schiel, M.; Wang, H.; Siwy, Z. S. *ACS Nano* **2015,** *9* (4), 4390-4397.

(31) Lan, W. J.; Kubeil, C.; Xiong, J. W.; Bund, A.; White, H. S. *J. Phys. Chem. C* **2014,** *118* (5), 2726-2734.

(32) Davenport, M.; Healy, K.; Pevarnik, M.; Teslich, N.; Cabrini, S.; Morrison, A. P.; Siwy, Z. S.; Létant, S. E. *ACS Nano* **2012**, *9*, 8366-8380.

(33) Edwards, M. A.; German, S. R.; Dick, J. E.; Bard, A. J.; White, H. S. *ACS Nano* **2015,** *9* (12), 12274-12282.

Chapter 2. Novel Nanoelectrodes

2.1 Introduction

The most popular method for producing ultramicroelectrodes requires sealing a platinum wire in a glass capillary.[1] The capillary and platinum wire are then heated and pulled to create a nanoscopic tip that is revealed through polishing. This method often produces electrodes that are larger than desired, and many replicates are required to produce nanoelectrodes of small enough dimensions. This process requires a skilled operator and success rates for a novice are typically low. Each step in this process requires a fine degree of control as something can go wrong during each. During the loading of the capillary with platinum wire, the wire must be seated correctly in the middle of the capillary. During the heating and pulling process the wire can be broken, leading to an electrical disconnect between the electrode at the tip of the wire and the connection to the potentiostat at the back.

Here we demonstrate several methods of fabricating nanoelectrodes of reproducibly small dimensions. These nanoelectrodes are shown to have a diffusion limited current that accurately represents their nanoscale dimensions. Additionally, these nanoelectrodes can be milled into unique band geometries of varying aspect ratios. These nanoelectrodes are fabricated for a fraction of the cost of the current state-of-the-art pulled platinum nanoelectrodes and have a higher success rate upon completion.

2.2 Experimental

2.2.1 Chemicals and Materials

Chemicals used were sulfuric acid (H_2SO_4, 95-98%, J. T. Baker), hydrochloric acid (HCl, 36.5-38.0%, J. T. Baker), hydrogen peroxide (H_2O_2, 30%, J. T. Baker), photoresist AZ1512 with AZ351 developer (AZ Corporation, developer diluted 1:5 developer:DI H_2O), ferrocene methanol

(FcMeOH, Sigma-Aldrich 97%), potassium chloride (KCl, 99%+, Fisher Scientific), 2-allylphenol (Sigma-Aldrich 98%), and potassium hydroxide (KOH, 85%, Fisher Scientific).

Double sided polish 500 +/- 25 µm thick <100> silicon wafers coated on both sides with 50 nm of LPCVD silicon nitride were purchased from Rogue Valley Microdevices. Evaporation materials used were gold pellets (99.999%, Kurt J. Lesker) and chromium coated tungsten rods (99.999%, Kurt J. Lesker). Gold wires of 0.025 mm diameter were from Alfa-Aesar. Ag/AgCl quasi-reference electrodes (QRE) were prepared by immersing 0.5 mm diameter silver wire from Alfa-Aesar into Tough Guy brand ultra-bleach until the wire turned a noticeable shade of purple-grey.

A FEI XL830 Dual Beam scanning electron microscope (SEM) / focused ion beam (FIB) was used for milling and imaging pyramid nanoelectrodes. A Vision parallel plate reactive ion etcher (RIE) was used with a CHF_3/CF_4 recipe to etch silicon nitride.

2.2.2 Fabrication of Carbon and Gold Nanoelectrodes

5 µm diameter carbon fibers and 25 µm diameter gold wires were both electrochemically etched to a nanoscopic tip using a platinum ring as a counter electrode. Carbon fibers were electrochemically etched in a 1 M KOH solution using a 10 Hz, 4 V_{pp} square wave. Gold wires were electrochemically etched in a saturated KCl solution with a 10 Hz, 2 V_{pp} square wave. In both cases the tip of the substrate to be etched was threaded through the platinum ring and positioned at the surface of the etching solution. The carbon or gold substrate was then retracted a few mm to form a meniscus around the tip to be etched. The carbon fiber and gold wire etching setup is shown in **Scheme 2.1**. Upon application of the voltage the substrate began to etch, causing the meniscus to fall toward solution. This dynamic process creates a taper with a fine point at the

end pointed toward the solution when etching is complete. Etching was determined to be finished when the solution and substrate were no longer in physical or electrical contact.

Both carbon and gold etched substrates were electrochemically insulated with polyphenol. To begin, the substrate was threaded through a platinum ring counter electrode and submerged in 20 mL of a 0.2 M 2-allylphenol 50%/50% methanol/water solution adjusted to pH 9.2 with NH_4OH. A 4 V DC anodic potential was applied to the etched substrate for 10 minutes to electro-oxidize the allylphenol onto the substrate. The substrate was removed and placed for 30 minutes in an oven set to 160 °C to cross-link the electrodeposited polyphenol.

2.2.3 Fabrication of Pyramid Nanoelectrodes

A double-side polished 500 +/- 25 µm thick <100> silicon wafer coated on both sides with 50 nm of LPCVD silicon nitride was spin coated with AZ 1512 that was spun at 4000 rpm for 60 s and then prebaked at 110 °C for 60 s on a hotplate. Following this the photoresist was exposed with 60 mJ/cm^2 at 405 nm with a Mylar photomask (CAD Art Services) that had circles in it with a diameter that would produce a pyramid that terminates inside the wafer at a depth of 410 µm when the silicon was etched with KOH. The photoresist was developed with 1:4 AZ 340:DI water for 60 s and then rinsed and dried. The wafer was then dry etched in a Vision Reactive Ion Etcher (RIE) using a CHF_3/CF_4 recipe until the silicon nitride was removed. The photoresist was then stripped in DuPont EKC photoresist remover and the wafer was placed in a 30% KOH bath at 80 °C for 6 hours until the etching terminated inside of the wafer. Following this the wafer was placed in a 49% HF bath until the remaining silicon nitride was removed, leaving a bare silicon wafer with inverted pyramids inside. This bare wafer was then placed in a tube furnace and oxidized for 1 hour at 1000 °C until approximately 250 nm of silicon oxide had grown over the silicon. A 200 nm thick gold layer with a 20 nm chromium adhesion layer was then deposited in 2.5 x 2.5 mm^2

patches over each inverted pyramid using a stainless steel shadow mask (Photo Etch Technology). The other side of the wafer was then etched using a deep reactive ion etcher (DRIE) until the pyramids were approximately 70 µm proud of the surface.

After wafer processing the electrodes were cut from the wafer using a diamond scribe. Each electrode was then inspected for quality before being brought to the FIB to have the apex milled off, exposing a gold electrode. Substrates were stuck to a conductive chuck with conductive carbon tape to allow conduction of electrons and to minimize vibrations during milling. Following FIB milling the gold was contacted through the back with a tungsten wire and silver epoxy. A nitrile O-ring was then fastened around the pyramid on the top of the chip with epoxy to isolate the electrode.

2.2.4 Electrochemical Measurements

All nanoelectrodes were electrochemically tested in various redox solutions using cyclic voltammetry. Pyramid nanoelectrodes specifically were tested by placing a 30 µL droplet of redox solution along with a platinum reference electrode into the O-ring isolating the electrode from the rest of the chip. Steady-state voltammograms were recorded using a PC-controlled Dagan Chem-Clamp (Dagan Corporation, Minneapolis, MN) voltammeter and data was recorded using an in-house virtual instrumentation program written in LabView (National instruments) on a Dell PC equipped with a PCI-6251 (National Instruments) data acquisition card.

2.2.5 Finite Element Analysis

A band electrode was simulated using COMSOL Multiphysics version 3.4 software installed on a Dell Precision T7400 (Intel Xeon E5430 dual die quad core, 1333MHz FSB, 2.66 GHz, 8 GB DDR2 SDRAM). A band electrode with an electroactive area of 1300 nm x 50 nm and a surrounding insulating area extending 300 nm from every side on top of a pyramid was simulated.

The pyramid was 71 µm tall and had a base of 100 µm x 100 µm. There was a surrounding solution volume of 5000 x 5000 x 5000 μm^3 into which the electrode pyramid was placed. The sides next to and opposite the pyramid had a concentration set to the bulk concentration, C_b. Every other side except the electrode surface was set to have no flux.

To simulate CVs the Nernst equation, $E = E^0 + (RT/nF)\ln(C_o/C_R)$, was rearranged to obtain

$$C_R = \frac{C_b}{\left(1 + \exp\left[\frac{nF}{RT}(E(t) - E^0)\right]\right)}$$

Where C_b is the bulk concentration, n is the number of electrons transferred in the redox reaction, F is the Faraday constant, R is the universal gas constant, T is the absolute temperature in Kelvin, E^0 is the formal redox potential, and E(t) is a triangular potential waveform generated from the parameters of initial and final potential, V_i and V_f, as well as the scan rate *v*. To match our experimental conditions the parameters were set as follows: C_b = 1 mM, D = 0.67 x 10^{-5} cm^2/s, n = 1 mol, F = 96485 C/mol, R = 8.31 J/mol·K, T = 298 K, V_i = -0.2 V, V_f = 0.6 V, v = 10 mV/s, and E^0 = 0.232 V. The rearranged equation was used as the boundary condition at the electrode surface. Following simulation, the potential values of the simulated CVs were adjusted by -0.1 V to account for the experimental CVs having a platinum reference electrode instead of a Ag/AgCl reference electrode.

2.3 Results and Discussion

2.3.1 Fabrication of Carbon and Gold Nanoelectrodes

Carbon fibers and gold wires were electrochemically etched to a fine point using a method commonly used for producing scanning tunneling microscope tips.[2,3] Etching was confirmed by looking at the subsequent wire under an optical microscope at a magnification of 20x where the point was clearly visible and distinguishable from the previous wire or fiber. Different etch

geometries can result, from sharper points to duller points and to completely sheared fibers that were etched to a square profile.

The final profile of the etched fiber or wire was independent of square wave frequency. Frequencies from 10 kHz to 10 Hz were tested with no difference in individual results or statistical variation. A frequency of 10 Hz was chosen to more easily monitor Faradaic oxidation current in the absence of fast charging current that was present at higher square wave frequencies.

The peak-to-peak voltage of the square wave had a large effect on the wire and fiber etching. The etching of the substrate is a Faradaic oxidation process and therefore requires a threshold potential to be applied before electron transfer can occur. This was different between the substrates with $Au \rightarrow AuCl_4^- + 3\ e^-$ occurring at +1.002 V vs NHE.[4] An anodic square wave voltage that was significantly below the threshold potential caused no etching while being near the threshold caused slow etching. This slow etching is theoretically preferable as it will produce the sharpest point. This is due to material being evenly removed from the tip and the sides of the tip during the etching process instead of being focused at the tip. For example, etching a gold wire at +1 V vs NHE could take upward of 30 minutes. More importantly, it was found that this methodical approach was unnecessary, with gold nanoelectrodes with radii of sub 10 nm being produced from wires that were etched at 2 V or higher, which only took a few minutes.

Another important factor in substrate etch profile was the counter electrode. If the substrate was not centered in the platinum ring there would be a higher current density on one side of the substrate relative to the other when the voltage was turned on. This results in an uneven etch rate and produced etched fibers and wires that tapered at an angle, rather than staying in parallel with the axis of the main fiber or wire. In most instances, this variation was the hardest to control for

and therefore was the main culprit behind variation in etch profiles rather than square wave frequency or potential.

Polyphenol deposition was adapted from previous reports.[5] Polyphenol electrodeposition and curing parameters had to be optimized to enable polymer pull-back from the substrate tip. The pull-back was theorized to occur based on previous reports using electrophoretic paint.[6] Four factors were involved in the polymer deposition and curing: 1) deposition solution pH, 2) deposition time, 3) curing oven temperature, and 4) curing time. A higher deposition solution pH created a thicker polyphenol film on the electrode. It was beneficial to have a thicker film to prevent formation of pinholes during curing however too thick of a film would prevent polymer pull-back from the tip during curing. A pH of 9.2 was found to be optimal in terms of balancing these two concerns, however it could likely be optimized more in conjunction with other factors. Likewise, a longer deposition time created a thicker film more likely to be free from pinholes, and deposition times of 4, 6, 8, 10, and 12 minutes were tested. 10 minutes was found to be optimal because it produced a 60% success rate in terms of electrochemical response, with each successful electrode having a critical electroactive dimension below 500 nm. Times lower than 10 minutes produced more successful electrodes but with larger dimensions and 12 minutes produced no successful electrodes, likely due to a complete insulation of the etched wire or fiber.

Polyphenol cross-linking during oven curing was critical to the formation of an insulating film free of pinholes. Oven curing temperatures of 110 and 160 °C were used to control polymer pull-back and cross-linking. The lower temperature of 110 °C was found to insufficiently cross-link the polymer, resulting in overly large Faradaic currents during electrochemical testing and thus a curing temperature of 160 °C was used. Likewise, curing times of 10 and 30 minutes were

used with 10 minutes being too low to complete cross-linking on the electrode which gave large electrochemical currents when measured.

SEM imaging was also employed to examine the pull-back of the polymer from the sharp fiber or wire tip. **Figure 2.1** shows an example of an etched gold wire before and after insulation with polyphenol. Unlike insulation on an unetched substrate, the polymer has pulled back from the tip during curing, exposing an electroactive area which is frequently on the nanometer scale. We believe this pull-back occurs during the oven heating process, when the polymers are being cross-linked and dried.

2.3.2 Electrochemical Measurements of Carbon and Gold Nanoelectrodes

To examine the insulating properties of polyphenol a carbon fiber was insulated with polyphenol and tested electrochemically. This carbon fiber was not etched, but was instead left with a large 100 μm length fiber protruding from the laser pulled glass. This was insulated with polyphenol in the same manner as the nanoelectrodes and tested. There was no Faradaic current in FcMeOH solution after insulation. The fiber was then cut with a scalpel to expose an uninsulated disk at the end of the insulated fiber which was then tested in FcMeOH which produced an electrochemical response. The CVs of the before and after cutting the fiber are shown in **Figure 2.2**.

Carbon and gold nanoelectrodes were fabricated down to several nanometers in radius as measured electrochemically as shown in **Figure 2.3**. These electrodes sometimes gave extremely small diffusion limited currents of only a few pA. In these cases, the concentration of redox mediator was increased to see a corresponding increase in current to verify that there was Faradaic current. The extremely small nature of these electrodes suggests that the electrodeposited polyphenol insulator was pinhole free, or that perhaps there was a single pinhole which was giving

the electrochemical response. The wire or fiber was also submerged in the redox solution to various depths to examine whether there were pinholes in the insulating film. The electrochemical response was the same regardless of the length of wire or fiber submerged, suggesting that the exposed electrode was localized at or near the etched tip.

The size of nanoelectrodes was measured by taking the diffusion limited Faradaic current and calculating the radius. The equation used was for a disk in an infinite insulating plane.[7]

$$i_{ss} = 4rnFDC$$

Where i_{ss} is the steady-state, or diffusion limited current, r is the radius of the ultramicroelectrode, n is the number of electrons transferred in the redox reaction, F is the Faraday constant, D is the diffusion coefficient, and C is the concentration of redox mediator.

2.3.3 Fabrication of Pyramid Nanoelectrodes

Three wafers were processed in parallel and were inspected after each step to ensure quality. An image of a patterned wafer awaiting the final DRIE etch step is shown in **Figure 2.4**. FIB milling produced gold nanoelectrodes with square and band geometries with a higher rate of success than conventionally fabricated pulled platinum nanoelectrodes. The overall success rate for the 26 electrodes fabricated was 58% with 15 out of the 26 producing a cyclic voltammogram in FcMeOH. SEM images of a pyramid nanoelectrode throughout the FIB milling process are shown in **Figure 2.5**. The fabrication process for pyramid nanoelectrodes was based on previous reports from other groups.[8,9]

The large etch depth of 410 μm and the large patterned area on the surface of the chip resulted in some pyramid electrodes having a band shape instead of a fine point. Some pyramid electrodes were fabricated with a band structure. The shape of the electrode can be controlled through milling with resolution below 100 nm.

2.3.4 Electrochemical Measurements of Pyramid Nanoelectrodes

Pyramid nanoelectrodes showed steady-state CVs when measured in FcMeOH regardless of variation in band length or width as shown in **Figure 2.6**. Pyramid nanoelectrodes displayed large amounts of capacitive current. The exposed pyramid was a large parallel-plate capacitor, with a pyramid of gold hidden under a thin layer of insulation. The charging current could be reduced through a lower scan rate or during fabrication by increasing the thickness of insulator deposited onto the pyramid. The large capacitive current did not interfere with measurements and was only evident during voltammetry. During constant potential amperometry there was no change in potential and thus no capacitive current. The eventual intended purpose of these electrodes is for use in constant potential scanning electrochemical microscopy and the capacitive current seen during voltammetry would not interfere with that.

Square pyramid nanoelectrodes often displayed smaller amounts of current than were predicted from their size. Square electrodes typically had an edge length of around 150 nm as measured with SEM. To predict the current for the square pyramid nanoelectrodes we equated the square area with the area of a circle and used the equivalent radius to solve for the diffusion limited current of a disk electrode. We found this to be an adequate assumption with predictions being within 30% of experimental results. We suggest this is due to the uncertainty involved in measuring the electrode area with SEM. Electrons from an electron microscope can penetrate thin layers and reveal information below a top insulating layer. An empirical equation exists for the calculation of the penetration depth of an electron beam.[10]

$$X(\mu m) = \frac{0.1E^{1.5}}{d}$$

Where X is the penetration depth in μm, E is the energy of the accelerated electrons in keV, and d is the density of the material in g/cm^3. For an electron energy of 5 keV and a density of 3.17 g/cm^3

for silicon nitride, this corresponds to a penetration depth of 350 nm. It is therefore reasonable, given that the insulator is at most 200 nm thick, to assume that the apparent area of the electrode will always appear larger than it actually is.

In addition to square pyramid nanoelectrodes, pyramid nanoband electrodes were also fabricated. These showed a close correlation with band electrode theory.[11,12]

$$i = 2\pi nFDCl\left(\frac{1}{\ln(4\theta)}\right)$$

Where F is the Faraday constant, D is the diffusion coefficient, C is the concentration of redox molecule, l is the length of the band, and $\theta = Dt/r^2$ with r being the radius of a hemi cylinder of equivalent area and t being the characteristic time scale of the cyclic voltammogram. In this case r = w/4 with w being the width of the band electrode. In 60% of the cases the band theory current and experimental current were within 30% of each other. A tabular and graphical representation of pyramid nanoband electrodes is shown in **Figure 2.7**.

2.3.5 Finite Element Analysis

To verify the nanoband electrode theory we used a finite element simulation of a pyramid nanoband electrode. Dimensions measured from SEM were used to construct the pyramid nanoband with a high degree of accuracy as seen in **Figure 2.8**. This is reflected in the correlation between the simulated and experimental electrochemical response. Capacitive current was not modeled and is therefore missing from the simulated CV.

2.4 Conclusions

Nanoelectrodes are useful tools with many electroanalytical applications such as scanning probe microscopies or coupled electrochemical-spectroscopic imaging. To date, nanoelectrodes have been mainly limited to laser-pulled platinum nanoelectrodes, however this method is not

capable of producing carbon or gold nanoelectrodes. Other nanoelectrode fabrication methods exist for producing nanoelectrode geometries with these materials but they are not conducive to many applications because they lack a focused tip. We have presented reproducible methods for fabricating nanoelectrodes from these materials in geometries that would be useful for these applications. Carbon and gold nanoelectrodes with a sharp tip can be fabricated from etched carbon fibers and gold wires that are then insulated with an electrodeposited polymer. Gold nanopyramid electrodes with inorganic insulators are made which are useful for coupled Raman-electrochemical measurements. These can be fabricated with a square or band geometry using standard microfabrication techniques in a cleanroom.

2.5 Schemes and Figures

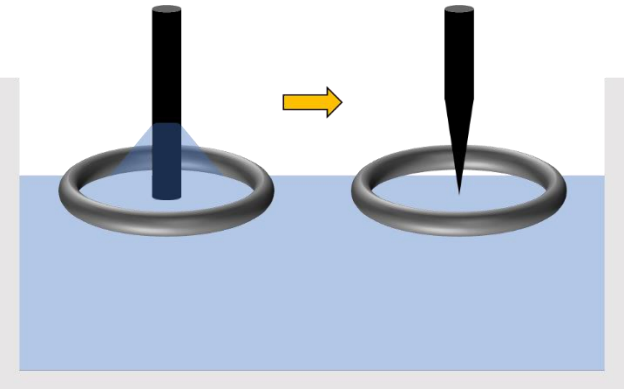

Scheme 2.1. Carbon Fiber and Gold Wire etching setup.

A carbon fiber (or gold wire) is threaded through a platinum wire ring counter electrode at the surface of an electrochemical etching solution. The carbon fiber, controlled by a micromanipulator, is first pushed into then retracted from the solution. This creates a meniscus of solution around the end of the carbon fiber. The etching voltage waveform is then applied between the carbon fiber and platinum ring and the carbon fiber etches to a fine point as the solution pulls back from the tip during etching.

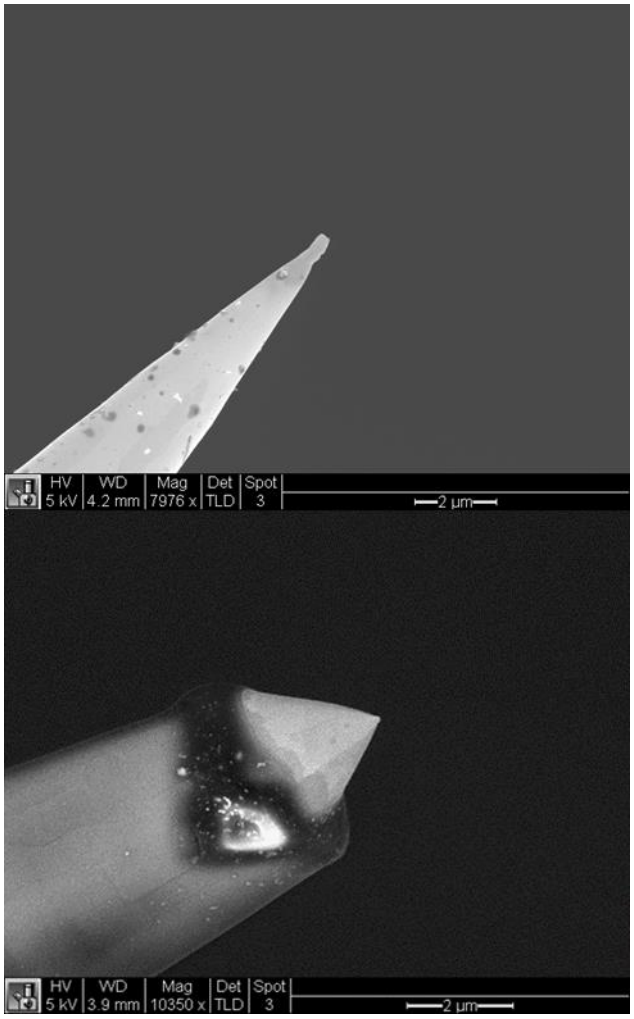

Figure 2.1. SEM images of polyphenol-insulated gold nanoelectrodes.

(Top) A gold wire that has been etched to a fine pont. (Bottom) An etched gold wire that has been insulated with polyphenol then cured, exposing the tip.

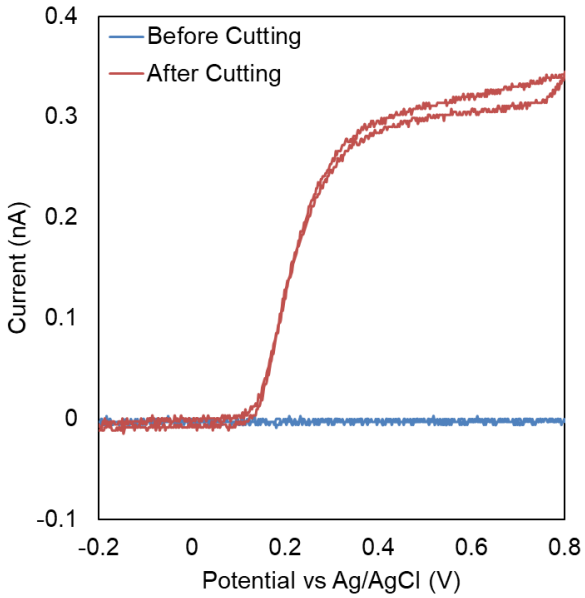

Figure 2.2. Polyphenol-insulated carbon fiber electrode before and after cutting with a scalpel.

CVs were taken in 100 µM dopamine and 100 mM $HClO_4$ at 50 mV/s.

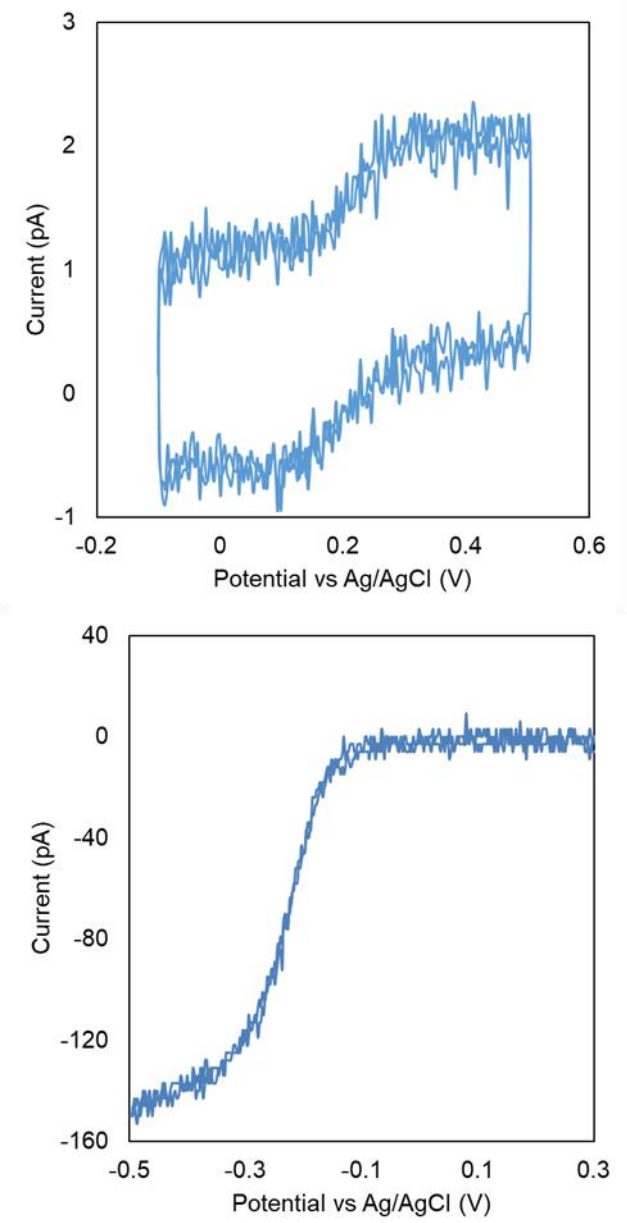

Figure 2.3. CVs of gold and carbon nanoelectrodes.

(Top) CV of a 4-nm-radius gold nanoelectrode in 1 mM FcMeOH and 100 mM KCl at 100 mV/s. (Bottom) CV of a 58-nm-radius carbon nanoelectrode in 10 mM $Ru(NH_3)_6Cl_3$ and 500 mM KCl at 200 mV/s.

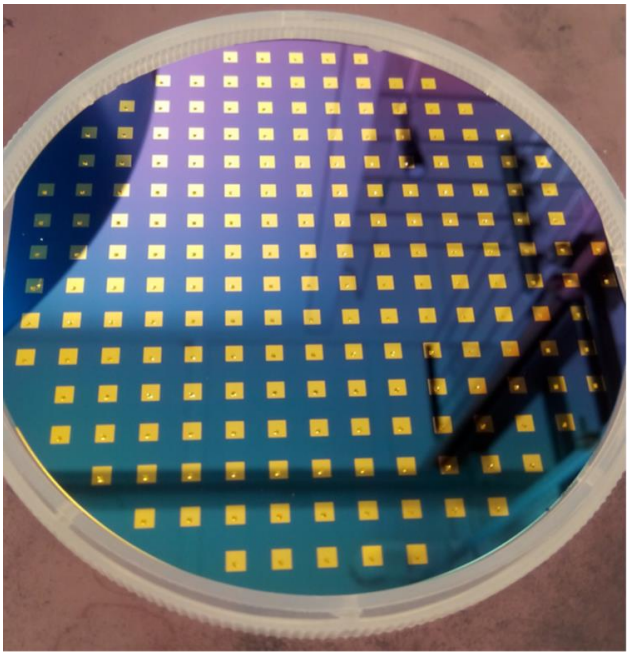

Figure 2.4. Wafer containing pyramid nanoelectrodes prior to final batch process.

A 100 mm wafer containing inverted pyramids that will become pyramid nanoelectrodes. Each inverted pyramid had a gold pad of 2 x 2 mm^2 evaporated over it as masked by a stainless steel shadow mask.

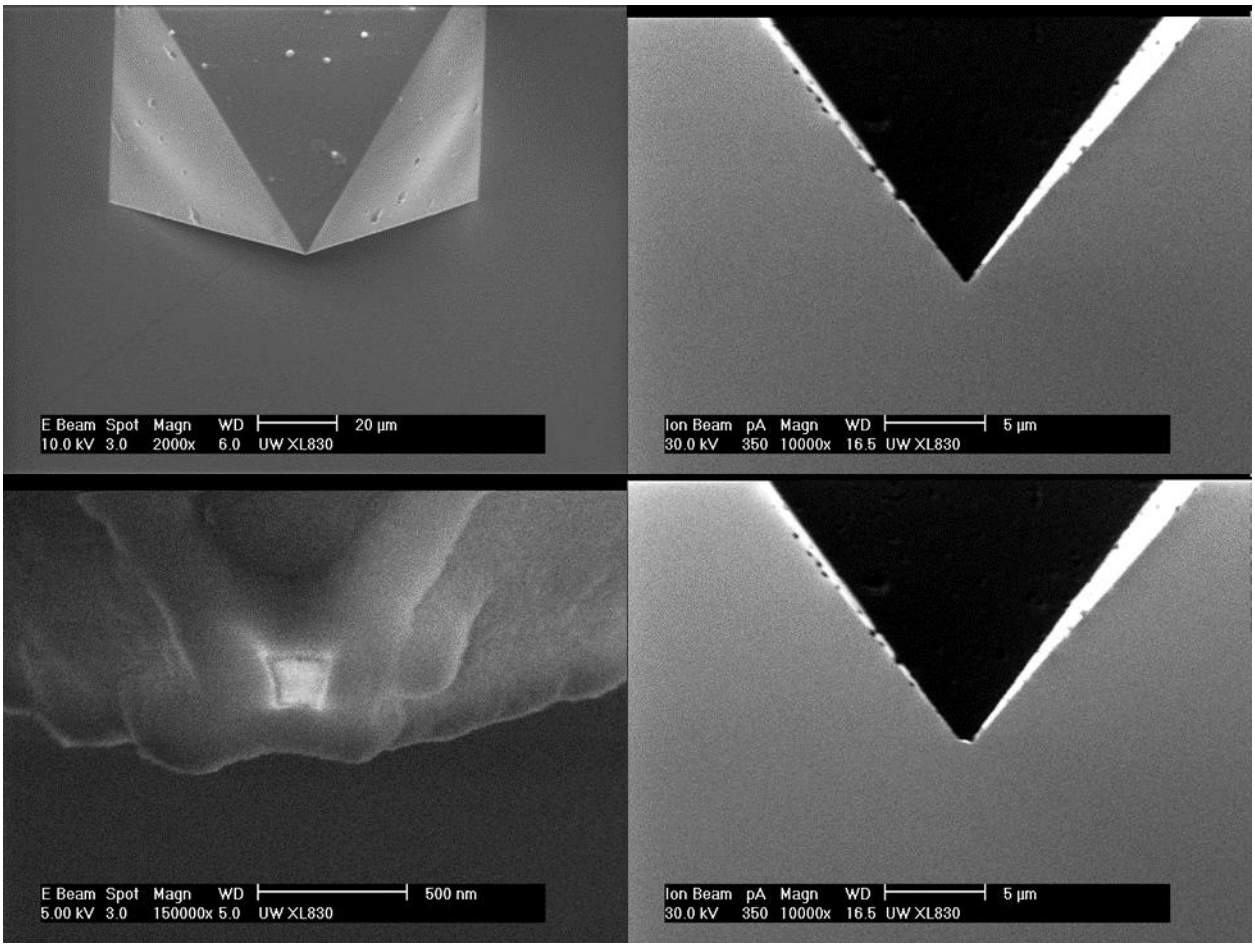

Figure 2.5. SEM images of pyramid nanoelectrode throughout fabrication.

Counterclockwise from the top left: SEM image of pyramid on chip surface, ion beam image of pyramid before FIB milling, ion beam image of pyramid after FIB cutting of the tip, and SEM image of exposed gold nanoelectrode at tip of the pyramid.

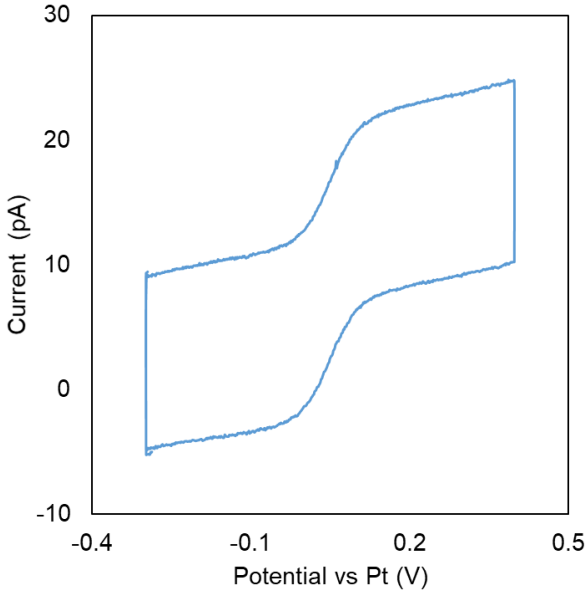

Figure 2.6. CV of a gold pyramid nanoelectrode.

The equivalent radius of this square nanoelectrode is 50 nm. CV was taken in 1 mM FcMeOH and 100 mM KCl at 10 mV/s.

Length (nm)	Width (nm)	Predicted Current (pA)	Experimental Current (pA)
445	127	20	8
680	80	28	20
615	128	28	27
641	130	30	80
846	180	42	45
1000	128	46	35
1016	129	47	45
1304	43	48	45
1320	38	48	26
1196	98	52	100
1100	55	43	23

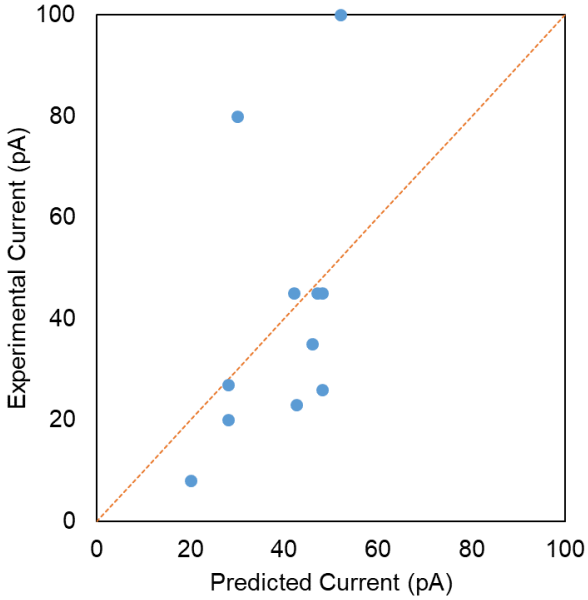

Figure 2.7. Comparison of experimental diffusion limited currents with theory.

(Top) Table of fabricated pyramid nanoband electrodes with band length, width, experimental diffusion limited current, and theoretical diffusion limited current as predicted from Equation 2. (Bottom) Plot of experimental diffusion limited currents versus predicted. The orange dashed line is the line of equivalence. Most pyramid nanoband electrodes had a lower experimental diffusion limited current than predicted.

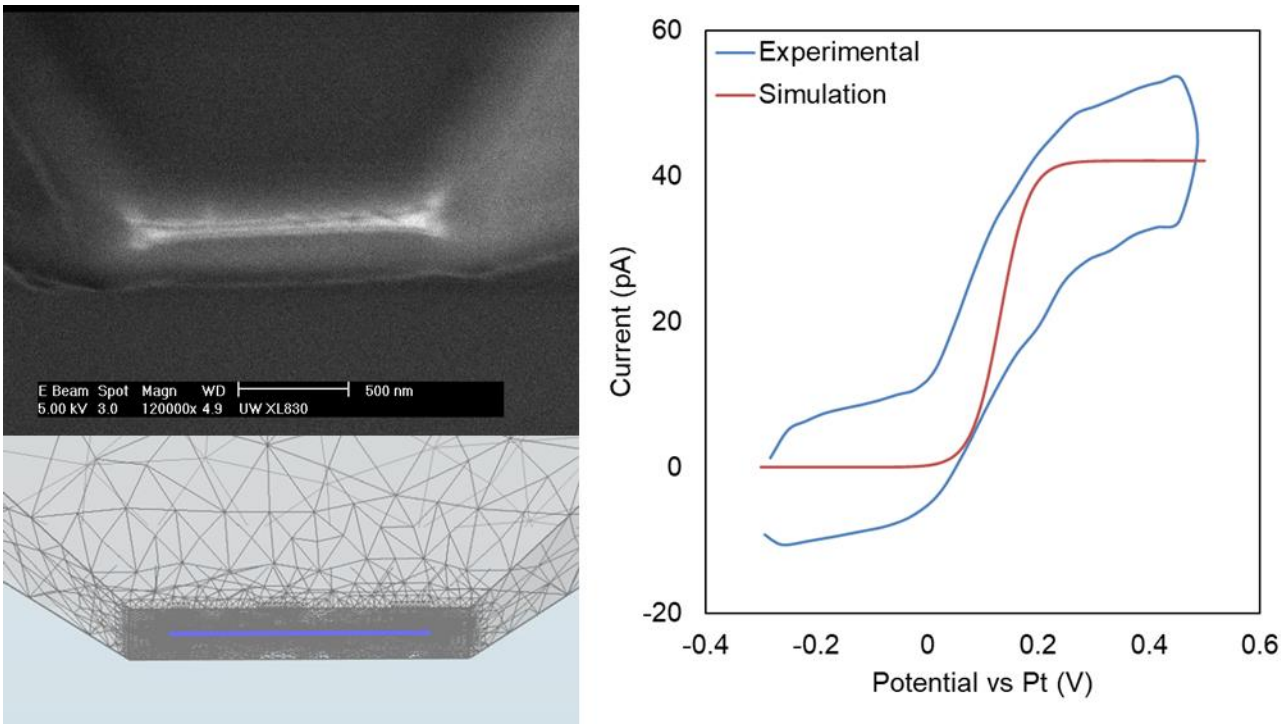

Figure 2.8. Finite element analysis of pyramid nanoband electrodes.

(Top left) SEM image of pyramid nanoband electrode. (Bottom right) FEA simulation geometry of pyramid nanoband electrode. (Right) Comparison of experimental and simulation CVs of the pyramid nanoband electrode. CVs taken and simulation in 1 mM FcMeOH and 100 mM KCl at 10 mV/s.

2.6 References

(1) Shao, Y. H.; Mirkin, M. V.; Fish, G.; Kokotov, S.; Palanker, D.; Lewis, A. *Anal. Chem.* **1997**, *69*, 1627-1634.

(2) Chen, S.; Kucernak, A. *Electrochem. Commun.* **2002**, *4*, 80-85.

(3) Sripirom, J.; Noor, S.; Köhler, U.; Schulte, A. *Carbon* **2011**, *49*, 2402-2412.

(4) Bard, A. J., Parsons, R., and Jordan, J. *Standard Potentials in Aqueous Solutions*, Marcel Dekker: New York, 1985.

(5) Strein, T. G.; Ewing, A. G. *Anal. Chem.* **1992**, *64*, 1368-1373.

(6) Chen, S.; Kucernak, A. *J. Phys. Chem. B* **2002**, *106*, 9396-9404.

(7) Bard, A. J.; Faulkner, L. R. *Electrochemical Methods*, 2nd ed.; John Wiley & Sons: New York, 2001.

(8) Pust, S. E.; Salomo, M.; Oesterschulze, E.; Wittstock, G. *Nanotechnology* **2010**, *21*, 105709-105721.

(9) Salomo, M.; Pust, S. E.; Wittstock, G.; Oesterschulze, E. *Microelectron. Eng.* **2010**, *87*, 1537-1539.

(10) Potts, P. J. *A Handbook of Silicate Rock Analysis*; Chapman and Hall: London, 1987.

(11) Wehmeyer, K. R.; Deakin, M. R.; Wightman, R. M. *Anal. Chem.* **1985**, *57*, 1913-1916.

(12) Amatore, C.; Fosset, B. *Anal. Chem.* **1996**, *68*, 4377-4388.

Chapter 3. Massive, Microfabricated Arrays of Ultramicroelectrodes

3.1 Introduction

Ultramicroelectrodes (UMEs) are key electroanalytical tools and have major advantages over larger electrodes in numerous fundamental and practical applications.[1,2] One of the greatest advantages is the reduced capacitive charging current on arrays of UMEs and nanoelectrodes, which can be useful for designing highly sensitive electroanalytical sensors, as previously reported by Martin and Penner.[3] As the dimension of an electrode approaches the thickness of the diffusion layer, one can expect to see enhanced mass transport to the electrode surface. As a result, UMEs reach a diffusion-limited state faster than larger electrodes.[4,5] Faster electron transfer rates can be measured when mass transport is no longer limiting at very small electrodes, e.g., electrodes below 100 nm.[6,7] Additionally UMEs have smaller capacitive and faradaic currents allowing them to be used in solutions of higher resistance because of a smaller *iR* drop across the solution.[8,9,10] At these conditions, a counter electrode may become unnecessary, as the currents passed are insufficient to cause significant potential drift on the reference electrode. Smaller capacitive currents resulting from a smaller electrode-solution interface permits higher scan rates, as high as 10^6 V/s, to be used in voltammetric measurements.[11,12]

Arrays of UMEs, when constructed carefully, have the properties associated with individual UMEs but generate the faradaic response of a larger electrode of the same geometric area as the array.[13,14,15] This is important when measuring low concentrations of analyte species that may not produce a large enough signal with a single UME. Signal-to-noise is also improved

---

This chapter is adapted with permission from Gunderson C. G. and Zhang, B. "Massive, Microfabricated Electrochemical Arrays of Ultramicroelectrodes" *J. Electroanal. Chem.* **2016**, *781*, 174-180.

in an array because faradaic current scales with the size of the array and capacitive current scales with electrode area.[16] These useful properties of UME arrays have led to their extensive use for applications including the testing of biologically important molecules[17,18] and heavy metals in polluted water.[19,20] Individually-addressable UME arrays are particularly useful for spatially and temporally monitoring electrochemically active redox events, such as secretion of neurotransmitters molecules from a single cell.[21]

Depending on the size and geometry of the UMEs, and whether or not electrodes are electrically connected or individually addressed, microelectrode arrays can be prepared by several methods. First, individually addressable UME arrays can be prepared on a glass micropipette probe which can be very useful to probe release of electroactive neurotransmitters from individual biological cells. To this end, Ewing's group has reported the fabrication and use of arrays of carbon-fiber microelectrodes (CFEs) and carbon rings on single PC12 cells.[22] His group[23,24] and others[25,26,27,28] have also used photolithography to prepare larger arrays with more uniform UMEs. Photolithography has been previously employed to fabricate large arrays of UMEs however this usually results in some amount of dead electrodes.[29,30] In addition to producing dead electrodes, some of the previous fabrication processes can be time-consuming and often involve multiple alignment, deposition, and etching steps requiring a wide variety of microfabrication tools.[30] Other methods involving printing[31] and microchips[32] have been used and there exists many different fabrication methods for creating electrochemical arrays.[33]

Here we present a method for fabricating massive arrays of highly uniform UMEs in a simple three-step process. The fabrication uses photoresist polymer as the insulating matrix which defines the position and area of UMEs. This method results in a nearly 100% success rate of electrode activity after fabrication. We tested the adhesion of the photoresist to our gold surface

by examining the capacitive current of different sized electrode arrays. The adhesion was also verified with electrodeposition of copper onto the electrodes. The electrodeposition of copper also served as a useful means to prove the electrochemical activity of each electrode in the array. Cyclic voltammograms (CVs) were taken and the peak heights compared with the empirical Randles-Ševčík equation and numerical simulation.

3.2 Experimental Section

3.2.1 Chemicals and Materials

All aqueous solutions were prepared using 18.2 MΩ deionized water obtained from a Barnstead Nanopure water purification system. All chemicals were used as received from manufacturers: acetone (Mallinckrodt Baker), isopropyl alcohol (Mallinckrodt Baker), potassium chloride (KCl, 99%+, Fisher Scientific), ferrocene methanol (FcMeOH, 97%, Sigma-Aldrich), photoresist AZ1512 and developer AZ351 (AZ Corporation, developer diluted 1:4 AZ351:DI water), copper sulfate pentahydrate ($CuSO_4 \cdot 5H_2O$, 98%, Sigma-Aldrich), sulfuric acid (H_2SO_4, 95-98%, J. T. Baker), hydrogen peroxide (H_2O_2, 30%, J. T. Baker), gold pellets (99.999%, Kurt J. Lesker) and chromium coated tungsten rods (99.999%, Kurt J. Lesker).

3.2.2 Array Fabrication

Massive electrochemical arrays of uniform UMEs were fabricated using standard photolithography techniques. A 4-inch silicon wafer was coated with 100 nm thermally evaporated gold with a 5-nm chromium adhesion layer. Prior to spin coating, the wafer was placed in 110 °C piranha (4:1 H_2SO_4:H_2O_2) for 10 min, rinsed in DI water, and spin dried. **CAUTION:** piranha solution reacts violently with organic species. Piranha solution should be used in ventilation hood with proper personal protection and extra care. The wafer was then dehydrated on a hot plate at 110 °C for 60 s and then immediately spin coated with AZ 1512 (Clariant) at 4000 rpm to a final

thickness of ~1.2 µm. The photoresist-coated wafer was photo masked with an array pattern and exposed to 60 mJ/cm^2 at 405 nm. The array patterns were designed in house and made in a chromium-on-quartz photo mask prepared by Photosciences Inc. UME arrays containing circular electrodes with diameters of 2, 3, or 4 µm were each made with an edge-to-edge electrode spacing of 1 µm in a square arrangement. After fabrication, electrical contact was made to the UME array by a tungsten wire and silver paste and fastened with epoxy. The dimensions of each array were 1 × 1 mm^2. The 4-µm-diameter electrode arrays had 40,000 electrodes, the 3-µm-diameter electrode arrays had 62,500 electrodes, and the 2-µm-diameter electrode arrays had 110,889 electrodes. UME arrays were inspected using a JEOL JSM-6400F scanning electron microscope (SEM) and an Olympus BX51 microscope in reflection mode.

3.2.3 Copper Deposition

Copper was electrochemically deposited into the electrodes of the array to evaluate the activity of the electrodes as well as photoresist adhesion to the gold. Copper was deposited from a 0.24 M $CuSO_4$ and 1.8 M H_2SO_4 solution by scanning between 0 and -0.2 V using a copper wire as the counter electrode at a scan rate of 20 mV/s for two scans.

3.2.4 Electrochemical Measurements

CVs were taken using a Pine bipotentiostat Model AFCBP1 and recorded using a homemade LabView (National Instruments) program. The potentiostat was interfaced to a Dell PC through a National Instruments 6251 DAQ card and a National Instruments BNC-2090 breakup box. A platinum counter electrode and an Ag/AgCl reference electrode (BASi) were used in a three-electrode setup with the array as the working electrode. All experimental CVs were taken in 1 mM FcMeOH with 100 mM KCl as the supporting electrolyte. A single drop of FcMeOH solution was placed onto the array and a platinum counter electrode and silver/silver chloride

reference electrode were positioned into the droplet. CVs were collected at scan rates of 50 mV/s, 100 mV/s, 200 mV/s, and 500 mV/s with solution being replaced between each scan.

3.2.5 Finite Element Analysis

All simulations were performed on a 24-core workstation using COMSOL Multiphysics software (version 4.3a, COMSOL Inc., Burlington, MA).

3.3 Results and Discussion

3.3.1 Array Fabrication

Massive electrochemical arrays containing up to 110,000 uniform circular gold UMEs were fabricated using standard photolithography techniques and the process is illustrated in **Scheme 3.1**. The use of silicon-based microfabrication facilities ensures that massive UME arrays can be batch prepared with high reproducibility and fidelity. For example, the process used in this work allows us to prepare >200 nearly identical UME arrays on a 4-inch silicon wafer. The actual diameter of the electrodes in the array is about 10% smaller than they are nominally. When optimizing the exposure conditions, small unwanted features were observed in the photoresist between adjacent electrodes that were likely generated from over exposure. This is explained by the close spacing of electrodes in the mask leading to increased exposure of the photoresist between the neighboring electrodes. The exposure dosage was further lowered until these unwanted features disappeared and the electrodes became circular, which also resulted in decreased size of the electrodes. A 1-μm electrode spacing was used for all the arrays fabricated in this work. However, if a new mask is designed with more spacing between electrodes, these inter-electrode artifacts will disappear. The decrease in electrode size does not cause any difference in the faradaic current at the scan rates used in this study due to strong overlap in the diffusion layer at adjacent electrodes.

Figure 3.1 displays SEM images of microfabricated electrochemical arrays having 4, 3, and 2 μm electrodes (from top to bottom). The images on the right are zoom out view of the same arrays on the left. The SEM images in **Figure 3.1** clearly demonstrate the exceedingly high uniformity of electrodes made in this work. One can see that the UMEs fabricated in each array have nearly identical size and shape over large areas (1×1 mm^2). Individual gold UMEs are defined by a thin layer of AZ 1512 photoresist spin-coated on the gold film. The film thickness was around 1.2 μm which gives slightly recessed geometry to the gold electrodes in the array. The spacing between adjacent UMEs was 1 μm for all the arrays in **Figure 3.1**.

For our electrochemical experiments, it is important to ensure that the photoresist polymer layer adheres strongly to the gold substrate and there is no leakage current or crosstalk between adjacent electrodes. The AZ 1512 photoresist is a general-purpose photoresist designed with stability in mind and its stability is well characterized and is stable in most aqueous solutions. The exception to this is in extremely basic solutions (in which photoresist is typically developed) and in solutions of oxidizing acids. This stability can be enhanced through crosslinking the photoresist polymers at elevated temperatures of 120 °C or higher. As is shown below, our tests demonstrated that the use of AZ 1512 forms a leak free and stable insulating layers in the UME arrays. In fact, we tested the stability of our arrays in a solution of 1.8 M sulfuric acid, an oxidizing acid, during the deposition of copper.

We have carried out two separate experiments to test the adhesion strength of the polymer to the gold surface. In the first test experiment, we deposited metal on each UME and microscopically checked for possible deposition at areas initially covered by photoresist. The use of metal deposition is an important procedure to examine electrochemical activity on microstructures such as graphene and carbon nanotubes.[34,35] Here, we electrochemically deposited

cupper onto gold UMEs in the array, dissolved the polymer layer, and imaged the resulting gold surface with SEM.

The UME arrays were examined with SEM after copper deposition and removal of the photoresist with acetone. **Figure 3.2** shows an SEM of the 4 μm UME array after copper deposition. Copper was electrochemically deposited into the slightly recessed electrodes of the array from a 0.24 M $CuSO_4$ solution containing 1.8 M H_2SO_4 by scanning the electrode potential between 0 and -0.2 V using a copper wire as the counter electrode. As one can see from **Figure 3.2**, copper was deposited uniformly on the electrodes covering the entire gold surface in the exposed areas. One can see that nanoparticles of copper were formed and evenly distributed on the surface of gold electrode during the electrodeposition process. Importantly, copper metal can only be found on the initially exposed gold but not on the polymer-covered areas indicating excellent adhesion property of photoresist on gold. Moreover, no inactive electrodes could be identified over large areas on the array. The copper electrodeposition demonstrates that nearly 100% of the electrodes in the array are active. This is important because one did not need to compensate for the inactivity of electrodes within the array during quantitative analysis of their electrochemical response and numerical simulation as every electrode that we inspected after copper electrodeposition contained uniform copper. The results shown in **Figure 3.2** demonstrate that the photoresist indeed insulates the inter-electrode volume.

In a second experiment, we examined the capacitive charging current for the different sized electrode arrays to further test polymer adhesion. The capacitive charging current is proportional mainly to the area of electroactive surface exposed,[36]

$$i_c = C_{dl} \times \nu \qquad [1]$$

where i_c is the charging current, C_{dl} is the double layer capacitance, and ν is the voltammetric scan rate (mV/s). To find the fraction of electrode surface area relative to total array area, we divide the total area electrode area by the geometric area of the array. The percent of electrode area exposed is 35%, 44%, and 50% for the 2 µm, 3 µm, and 4 µm electrode diameter arrays, respectively. When the uncorrected peak heights are plotted versus scan rate, as shown in **Figure 3.3**, the larger capacitive current for the larger exposed fraction arrays is apparent. In addition, the measured charging currents on these MEA arrays are comparable to that estimated based on their exposed area and the charging current measured on a 1-mm diameter gold macroelectrode in similar conditions.

3.3.2 Electrochemical Measurements

Peak-shaped voltammograms were observed at the scan rates used because of heavily overlapping diffusions layers leading to a planar diffusion of redox molecules from bulk to the surface of the array. Peak-shaped CVs were expected considering the small spacing of the arrays, which is smaller than the diffusion layer thickness estimated based on the scan rates used in this work. For example, the diffusion thickness can be estimated according to the following equation,

$$\delta = \sqrt{2D\tau} \qquad [2]$$

Where δ (cm) is the thickness of the diffusion layer, D (cm^2/s) is the diffusion coefficient for the redox molecule, and τ is the characteristic time duration of the voltammetric experiment and is estimated from $RT/\nu F$, where R is the gas constant, and T is temperature, and F is the Faraday's constant. The estimated τ is 2.6 s assuming a scan rate of 10 mV/s and the estimated diffusion layer thickness is 112 µm (assuming typical diffusion coefficient of 10^{-5} cm^2/s and T = 298 K). Since δ

= 112 μm is much greater than the 1 μm electrode spacing, there is significant overlapping of diffusion layer between adjacent electrodes in the array leading to the peak-shaped voltammetric response.

Figures 3.4a-c show a series of CVs taken at 4 different scan rates, 50 mV/s (yellow), 100 mV/s (blue), 200 mV/s (green), and 500 mV/s (red), from three different arrays (a) 2 μm, (b) 3 μm, and (c) 4 μm in 1 mM FcMeOH and 100 mM KCl. The scan rates used were in order from lowest to highest anodic peak current. Nearly ideal peak-shaped CVs were obtained for all three different arrays and the peak separations were between 65 and 70 mV for each array. The shape of the CV and the small peak separation both indicate excellent voltammetric performance and confirmed the planar diffusion resulting from strong diffusion overlap. Importantly, all the arrays had similar corrected peak currents (**Figure 3.6a**). This is expected as the geometric area of the array determines the total faradaic current assuming that diffusion layers overlap sufficiently. It is also noteworthy that even at an edge-to-edge spacing of 1 μm the photoresist adheres well and we obtain the capacitive current expected of an array. The arrays were meticulously cleaned with piranha solution as previously described and care was taken to not contaminate the gold surface afterward. Interestingly, the peak separation became smaller at higher scan rates, suggesting stronger contribution from FcMeOH molecules either trapped in the shallow polymer recess or adsorbed to the gold electrodes. One can anticipate that the voltammetric response will slowly transit to a thin-layer type response when scan rate is further increased similar to that observed for a glass nanopore electrode.[37,38]

We also compared our CV peak heights in **Figures 3.4a-c** with those predicted by the Randles-Ševčík equation,[39,40]

$$i_p = 0.4463nFAC\left(\frac{nF\nu D}{RT}\right)^{1/2} \qquad [3]$$

where *n* is the number of electrons transferred, *A* is the geometric area of the electrode, *C* is the concentration of redox molecule, and with other parameters previously defined. After correcting for capacitive charging current, the experimental CVs agree with the Randles-Ševčík prediction to within 5% for all arrays and scan rates. Some of this difference may be partly due to the use of the Randles-Ševčík equation for a disc electrode whereas our array geometry is square and the electrodes are slightly recessed.

3.3.3 Finite Element Analysis

The electrochemical response of the 2 µm UME arrays was first simulated in a 2D geometry using the diffusion domain approximation as well as a 3D geometry. The diffusion domain approximation secludes each electrode in the array into its own diffusion volume.[9] This single electrode and its volume were then simulated and the resulting voltammetric response was multiplied by the number of electrodes in the array. The difference in peak current height between the 2D and 3D simulations at all scan rates for the 2 µm simulations was less than 2%. All subsequent simulations were performed as 2D simulations. The 2D and 3D simulation geometries are shown in **Figure 3.5**.

The electrochemical reaction was modeled as a one electron oxidation of $R \rightarrow O + e^-$ occurring at a potential of $E^0 = 0.23$ V. Convection and migration were assumed to be insignificant compared to diffusion due to the presence of a large concentration of supporting electrolyte. The diffusion coefficient of the reduced and oxidized species of FcMeOH was assumed to be the same and was used as $D = 6.7 \times 10^{-6}$ cm^2 s^{-1}.[41] The potential waveform was modeled as a step-wise triangle function with a starting potential of -0.2 V, a switching potential of 0.6 V, and a frequency

that was dependent on the scan rate *v*. The simulation was run for one period of this waveform. The boundary condition at the electrode was

$$C_R = \frac{C_b}{\left(1+\exp\left(\frac{nF}{RT}\left(E(t)-E^O\right)\right)\right)} \qquad [4]$$

as previously described elsewhere[41] where C_R is the concentration of the reduced redox molecule, C_b is the bulk concentration, $E(t)$ is the step-wise triangle waveform described previously, and other parameters were previously defined.

Side 1 in **Figure 3.5a** is the electrode with a length equal to the radius of the electrode, either 1 μm, 1.5 μm, or 2 μm. This electrode is recessed by 1.2 μm, the thickness of the spun photoresist. This recessed electrode is placed into a confined diffusion volume. Side 1 has a boundary condition of the time dependent concentration as described in Eq. 1. Side 2 has a length equal to the radius of the electrode plus half a micrometer to simulate the individual diffusion volume of that electrode. Side 2 has the boundary condition of bulk concentration. Side 3 is the axis of the symmetry and has a length equal to the recess and an additional 1 mm to simulate the height of the drop of solution placed onto the array. All other sides in the 2D geometry have a boundary condition of no flux. In **Figure 3.5b** the 3D geometry has a boundary condition at the blue top of bulk concentration. The time dependent concentration Eq.1 is the boundary condition at the electrode surface at the bottom of the well. All other sides have the boundary condition of no flux.

Figures 3.4d-f are simulated CVs of the arrays in 1 mM FcMeOH using a 2D geometry. One can see that the simulation CVs are also peak-shaped and the shape matched quite well with

the experimental CVs. **Figure 3.6** shows a comparison of the experimental and simulated CV peak currents of all the arrays in 1 mM FcMeOH and 100 mM KCl at all four scan rates. Simulated peak heights show excellent agreement with experiment and prediction from the Randles-Ševčík equation at low scan rates but fall to ~75% of the theoretical and experimental values at 500 mV/s which suggests a shortcoming of the simulation method. Since the simulated currents are below the experimental, it is possible that the difference in redox current is due to underestimated redox flux at the edge electrodes. However, the exact reasons are still being investigated.

3.4 Conclusions

In summary, we have demonstrated the fabrication and voltammetric characterization of massive electrochemical arrays containing as many as 110,000 uniform ultramicroelectrodes. The photolithography-based fabrication method employed in this work is simple, fast, and reliable. Electrode size, shape, and spacing can be systematically varied to generate massive electrochemical arrays with controlled geometry. All electrodes examined were found to be active through copper electrodeposition. Voltammetric response of such arrays was found to be dominated by a planar diffusion resulting from heavily overlapping diffusion profiles of nearly electrodes. Their CVs have peak currents that matched very closely with the prediction using Randles-Ševčík equation. The voltammetric response was further verified by numerical simulation and the simulation matched well with the experimental at slow scan rates. The larger difference at higher scan rates were likely due to increasing edge effects and the details will be investigated in the future. This method should prove useful in creating uniform, active, and massive arrays of microelectrodes of any geometry for electroanalytical studies.

3.5 Schemes and Figures

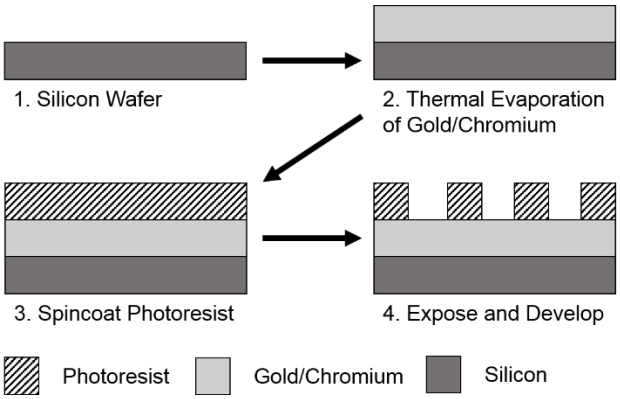

Scheme 3.1. Fabrication of massive electrochemical arrays.

A bare silicon wafer is coated with chromium as an adhesion for a subsequent layer of gold. The metal-coated wafer is dehydration baked before being spin coated with photoresist. The photoresist is then exposed with an array pattern and developed.

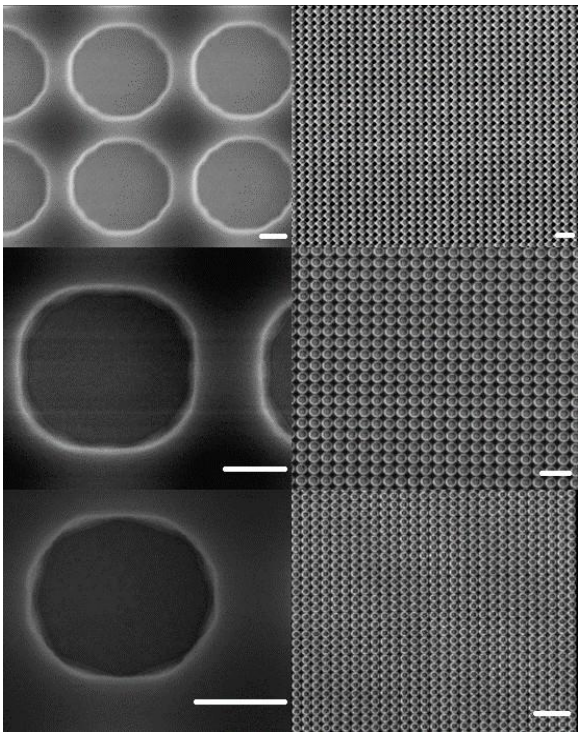

Figure 3.1. SEM images of microfabricated arrays.

(From top to bottom) 4, 3, and 2 μm electrodes in the arrays. The right panel is zoomed out from the left panel. Scale bars on the left side images are 1 μm and scale bars on the right side images are 10 μm.

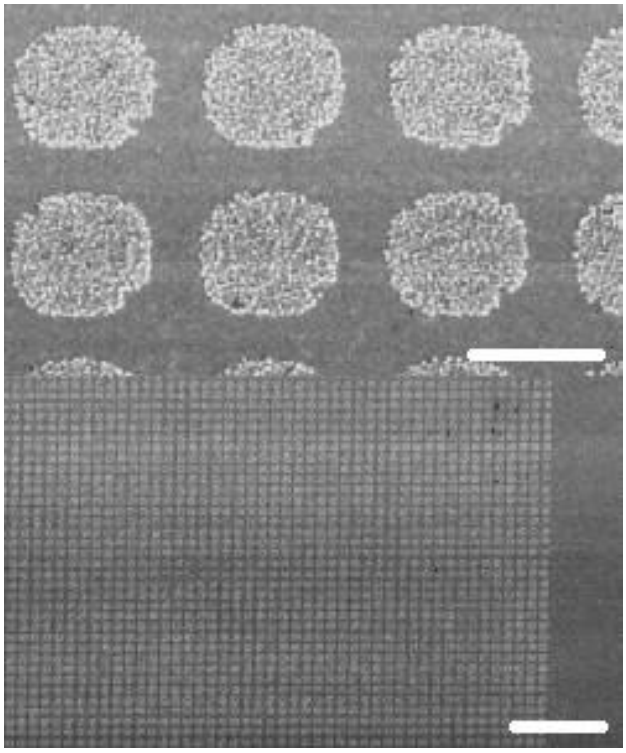

Figure 3.2. Copper deposited onto the UMEs of a 4-µm array.

The photoresist has been stripped with acetone. The bottom image is zoomed out from the top image to show the uniformity of deposition across the array as well as electrode activity. Scale bar is 4 µm in top image and 40 µm in bottom image.

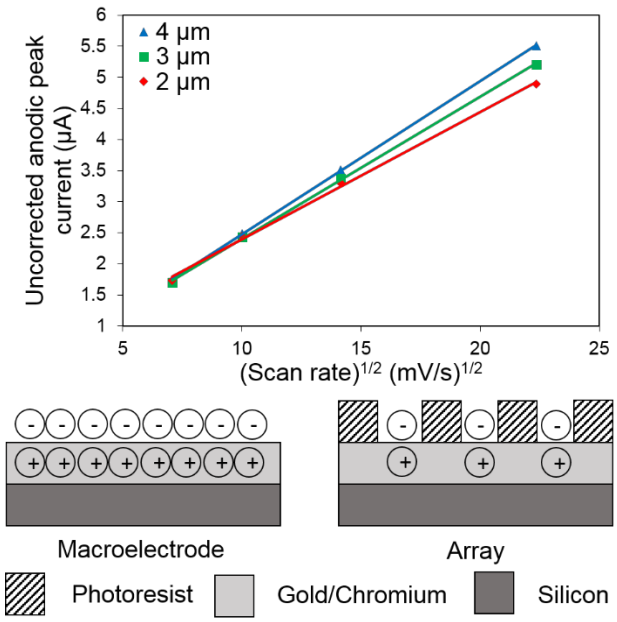

Figure 3.3. Capacitive current analysis of array voltammetry.

(Top) Uncorrected anodic peak current of the UME arrays in 1 mM FcMeOH and 100 mM KCl plotted against the square root of scan rate to show the additional capacitive current seen in arrays with a larger fraction of metal exposed. (Bottom) Illustration of the difference in capacitive current between a macroelectrode and an array of equivalent area.

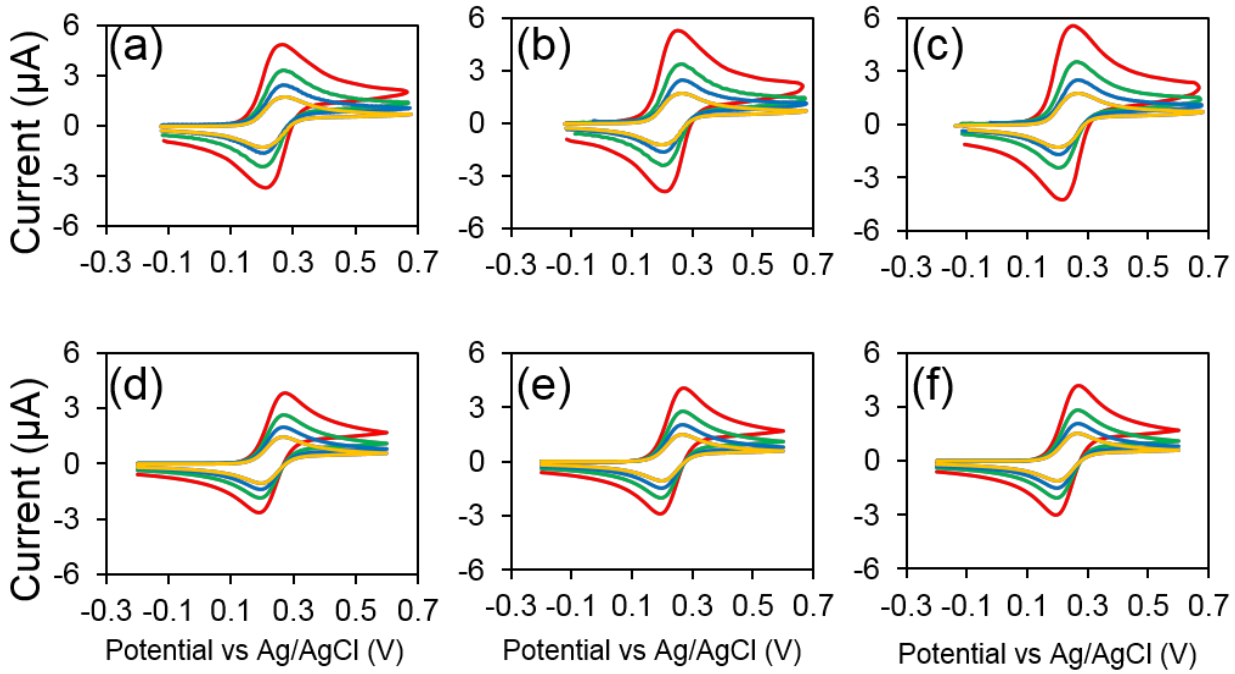

Figure 3.4. Experimental and simulated cyclic voltammetry of arrays.

Experimental CVs of the (a) 2 μm, (b) 3 μm, and (c) 4 μm arrays in 1 mM FcMeOH and 100 mM KCl. (d-f) Simulated CVs of the (d) 2 μm, (e) 3 μm, and (f) 4 μm arrays in 1 mM FcMeOH using a 2D geometry. The scan rates used are 50 mV/s, 100 mV/s, 200 mV/s, and 500 mV/s in order from lowest to highest anodic peak current.

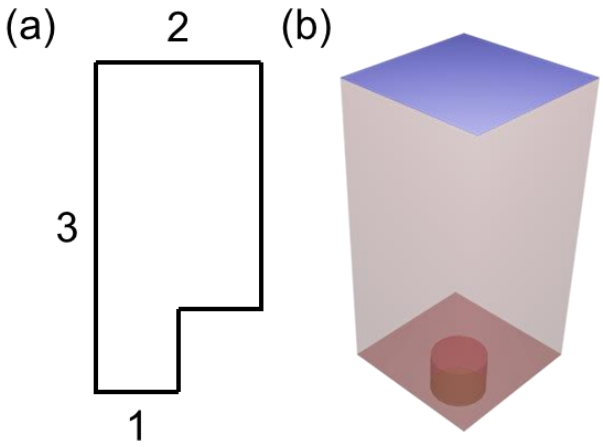

Figure 3.5. Simulated array geometries.

(a) Simulated 2D geometry. Side 1 is the time dependent concentration equation, side 2 is the bulk concentration C_b, and side 3 is the axis of rotational symmetry. All other sides are insulators with no flux. Not drawn to scale (b) Core electrode. The top blue side is the bulk concentration C_b, the disk at the bottom of the well is the time dependent concentration equation, all other red sides are insulators with no flux. Not drawn to scale.

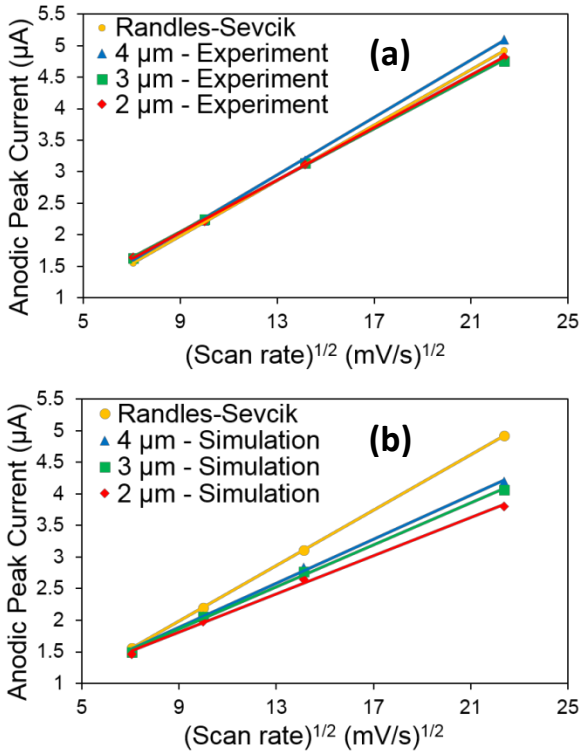

Figure 3.6. Randles-Sevcik analysis of array voltammograms.

(a) Experimental and (b) simulated CV peak currents of arrays in 1 mM FcMeOH and 100 mM KCl. Scan rates are 50 mV/s, 100 mV/s, 200 mV/s, and 500 mV/s.

3.6 References

(1) Oja, S. M.; Fan, Y.; Armstrong, C. M.; Defnet, P.; Zhang, B. *Anal. Chem.* **2016**, *88* 414–430.

(2) Arrigan, D. W. *Analyst*, **2004**, *129*, 1157–1165.

(3) Penner, R. M.; Martin, C. R. *Anal. Chem.* **1987**, *59*, 2625–2630.

(4) P. H. Rieger, Electrochemistry, p. 215-223, Chapman & Hall, Inc., New York, (1994).

(5) Heinze, J. *Angew. Chem. Int. Ed. Engl.*, **1993**, *32*, 1268–1288.

(6) Watkins, J. J.; Chen, J.; White, H. S.; Abruña, H. D.; Maisonhaute, E.; Amatore, C. *Anal. Chem.* **2003**, *75*, 3962– 3971.

(7) Mirkin, M. V.; Bard, A. J *Anal. Chem.* **1992**, *64*, 2293– 2302.

(8) Howell, J. O.; Wightman, R. M. *Anal. Chem.* **1984**, *56*, 524–529.

(9) Amatore, C.; Deakin, M. R.; Wightman, R. M. *J. Electroanal. Chem.* **1987**, *220*, 49–63.

(10) Oldham, K. B. *J. Electroanal. Chem.* **1992**, *337*, 91–126.

(11) Andrieux, C. P.; Garreau, D.; Hapiot, P.; Savéant, J. M. *J. Electroanal. Chem.* **1988**, *248*, 447–450.

(12) Amatore, C.; Maisonhaute, E. *Anal. Chem.* **2005**, *77*, 305A–311A.

(13) Penner, R. M.; Martin, C. R. *Anal. Chem.* **1987**, *59*, 2625–2630.

(14) Amatore, C.; Savéant, J. M.; Tessier, D. *J. Electroanal. Chem.* **1983**, *147*, 39–51.

(15) Davies, T. J.; Ward-Jones, S.; Banks, C. E.; del Campo, J.; Mas, R.; Muñoz, F. X.; Compton, R. G. *J. Electroanal. Chem.* **2005**, *585*, 51–62.

(16) Menon, V. P.; Martin, C. R. *Anal. Chem.* **1995**, *67*, 1920–1928.

(17) Moretto, L. M.; Pepe, N. Ugo, P. *Talanta* **2004**, *62*, 1055–1060.

(18) Ugo, P.; Pepe, N.; Moretto, L. M.; Battagliarin, M. J. *Electroanal. Chem.* **2003**, *560*, 51–58.

(19) Feeney, R.; Kounaves, S. P. *Anal. Chem*. **2000**, *72*, 2222–2228.

(20) Jena, B. K.; Raj, C. R. *Anal. Chem*. **2008**, *80*, 4836–4844.

(21) Abe, H.; Ino, K.; Li, C. Z.; Kanno, Y.; Inoue, K. Y.; Suda, A.; Kunikata, R.; Matsudaira, M.; Takahashi, Y.; Shiku, H.; Matsue, T. *Anal. Chem*. **2015**, *87*, 6364–6370.

(22) Zhang, B.; Adams, K. L.; Luber, S. J.; Eves, D. J.; Heien, M. L.; Ewing, A. G. *Anal. Chem.* **2008**, *80*, 1394–1400.

(23) Wang, J.; Trouillon, R.; Lin, Y.; Svensson, M. I.; Ewing, A. G. *Anal. Chem*. **2013**, *85*, 5600–5608.

(24) Wang, J.; Ewing, A. G. *Analyst* **2014**, *139*, 3290–3295.

(25) Hafez, I.; Kisler, K.; Berberian, K.; Dernick, G.; Valero, V.; Yong, M. G.; Craighead, H. G.; Lindau, M. *Proc. Natl. Acad. Sci. U. S. A.* **2005**, *102*, 13879–13884.

(26) Gosso, S.; Turturici, M.; Franchino, C.; Colombo, E.; Pasquarelli, A.; Carbone, E.; Carabelli, V. *J. Physiol.*, **2014**, *592*, 3215–3230.

(27) Wigström, J.; Dunevall, J.; Najafinobar, N.; Lovrić, J.; Wang, J.; Ewing, A. G.; Cans, A.-S. *Anal. Chem.* **2016**, *88*, 2080–2087.

(28) Nam, Y.; Chang, J. C.; Wheeler, B. C.; Brewer, G. J. *IEEE Trans. Biomed. Eng.* **2004**, *51*, 158−165.

(29) Menshykau, D.; Huang, X-J.; Rees, N. V.; del Campo, F. J.; Muñoz, F. X.; Compton, R. G. *Analyst* **2009**, *134*, 343–348.

(30) Huang, X-J.; O'Mahony, A. M.; Compton, R. G. *Small* **2009**, *5*, 776–788.

(31) Lesch, A., Momotenko, D.; Cortés-Salazar, F.; Wirth, I.; Tefashe, U.M.; Meiners, F.; Vaske, B.; Girault, H.H.; Wittstock, G. *J. Electroanal. Chem*. **2012**, *666*, 52–61.

(32) Lima, A. E. B.; Luz, G. E.; Batista, N. C.; Longo, E.; Cavalcante, L. S.; Santos, R. S. *Electroanal*. **2015**, *28*, 985–989.

(33) Spira, M. E.; Hai, A. *Nat. Nanotechnol*. **2013**, *8*, 83–94.

(34) Day, T. M.; Unwin, P. R.; Macpherson, J. V. *Nano Lett.* **2007**, *7*, 51–57.

(35) Quinn, B. M.; Dekker, C.; Lemay, S. G. *J. Am. Chem. Soc*. **2005**, *127*, 6146–6147.

(36) Bard, A. J.; Faulkner, L. R. Electrochemical Methods. 2nd ed.; John Wiley & Sons: New York, 2001.

(37) Zhang, B.; Zhang, Y.; White, H. S. *Anal. Chem*. **2004**, *76*, 6229–6438.

(38) Zhang, B.; Zhang, Y.; White, H. S. *Anal. Chem*. **2006**, *78*, 477–483.

(39) Randles, J. E. B. *Trans. Faraday Soc*. **1948**, *44*, 322–327.

(40) Ševčík, A. *Collect. Czech. Chem. Commun*. **1948**, *13*, 349–377.

(41) Guerrette, J. P.; Percival, S. J.; Zhang, B. *Langmuir* **2011**, *27*, 12218–12225.

Chapter 4. Bipolar Ultramicroelectrode Arrays for Fluorescence Enhanced Electrochemical Microscopy

4.1 Introduction

Electrochemical imaging is a useful technique for probing electron transfer on heterogeneous surfaces. Traditional electrochemical imaging techniques are scanning probe microscopies where the electrode is used as an electrochemically active probe that is scanned over a surface. [1, 2] During this technique, called scanning electrochemical microscopy, the electrochemical current at the probe is modulated by its distance from the surface being scanned. This arises from a reduction in the volume from which redox mediators can diffuse to the electroactive area of the probe. There can be positive or negative feedback to the electrochemical current depending on the properties of the scanned surface.[3] Another variant of this technique is scanning ion conductance microscopy, where ionic current passing through a nanopore is used as the sensing element.[4] These techniques, like many probe microscopies, have their drawbacks in resolution and acquisition time. The dimensions of the probe electrode directly affect the resolution of the scanned image. The resolution is also affected by scan time and the number of data points taken during each scan across the surface. Large surfaces of several square micrometers can take minutes to image with adequate resolution.[5] These limitations prevent the simultaneous acquisition of electrochemical data with sub-micron resolution with millisecond time resolution.

Other techniques using microelectrode arrays have been employed, namely in the detection of cell exocytosis from model neurons such as PC12 cells.[6] These cells emit packets of an electrochemically active neurotransmitter, dopamine, when stimulated with a high K^+ concentration solution. Electrochemical arrays have been used to not only measure different regions of a PC12 cell with high spatial resolution, but also to perform high throughput measurements of multiple cells simultaneously.[7] These arrays share a common reference/counter

electrode with multiple working electrodes, each of which must be electrically measured separately. Because of this limitation the technique does not scale well, with state-of-the-art electrode arrays typically numbering in the hundreds of individually addressable electrodes.

Recently, we have developed a technique that couples electrochemical and optical signals. This method allows us to monitor electrochemical signals with a camera.[8] This approach, called fluorescence enhanced electrochemical microscopy, or FEEM, couples the electron transfer from a redox molecule of interest to that of a fluorescent redox molecule. When the half-reactions couple, the fluorescent redox molecule is reduced or oxidized from a non-fluorescent state into a fluorescent one.

This approach is based on a relatively new field of electrochemistry called bipolar electrochemistry.[9] The half-reactions are coupled across a conductor embedded in an insulator that separates two distinct solutions, one containing the redox molecule of interest and the other the fluorescent redox molecule. Into each solution is placed a so-called driving electrode, because it has a large surface area which will not limit the electron transfer of the entire cell. A potential is applied across these driving electrodes which drives the coupling of the half-reactions at the bipolar electrode that bridges the two solutions. In FEEM, this concept is generalized to an array containing hundreds of thousands of electrodes/mm^2, all of which are polarized by a single pair of driving electrodes. The advantage of this compared to a conventional electrode array is a concentration of electrodes several orders of magnitude larger than the state-of-the-art electrode array in which each electrode is individually electrically connected.[7] Additional advantages are found by the manner in which the FEEM electrodes are addressed using optical methods. This optical approach permits the simultaneous electrochemical measurement of thousands of

electrodes without an electrical connection to each. A generalized FEEM scheme is shown in **Scheme 4.1**.

We want to use FEEM to study the communication within neural networks. To this end we have been testing PC12 model neuron cells with single carbon fiber electrode to understand their properties.[10] These model neurons will be used in upcoming FEEM experiments involving new arrays. New arrays are necessary because of the size of individual electrodes in the current arrays. Presently, the electrode arrays are made from 6 μm carbon fibers embedded in an epoxy which are too large to obtain spatial resolution of a single PC12 cell which is typically 10 μm in diameter.[8]

The most important component of a FEEM system is the electrode array. The electrode array is responsible for the electrochemical properties, response, and spatial resolution of the measurement. Previously, the carbon fibers in the electrode array did not extend through the epoxy parallel to each other, and in some cases contacted each other within the epoxy, leading to cross-talk between electrodes. The spacing of carbon fibers within the array are non-uniform which is not ideal for monitoring specific cell regions. The most important issue to be addressed with the fabrication of new arrays is the electrode diameter. By shrinking electrode diameter to 1 μm with a 1 μm edge-to-edge spacing we can fit more than 10 times as many electrodes on a PC12 cell.

Here we present the array fabrication methods employed so far in this pursuit. We present results from each method and give an outlook on their future promise.

4.2 Experimental

4.2.1 Chemicals and Materials

AZ1505 photoresist, AZ1512 photoresist, and AZ 340 photoresist developer, and AZ 300 MIF photoresist developer were from AZ Corporation. Propylene glycol monomethyl ether acetate

(PGMEA, >99.5%) and hexamethyldisilazane (HMDS, 99.9%) were from Sigma-Aldrich. Potassium hydroxide (KOH, 85%) was from Fisher Scientific. $HAuCl_4$ was purchased as a solution of 1% concentration of gold metal as measured by mass from Salt Lake Metals. Orotemp was purchased from Technic, Inc.

4.2.2 Silicon Nitride Window Chip Fabrication

A double-side polished 500 +/- 25 µm thick <100> silicon wafer coated on both sides with 1000 nm of LPCVD silicon nitride was spin coated with AZ 1512 that was spun at 4000 rpm for 60 s and then prebaked at 110 °C for 60 s on a hotplate. Following this the photoresist was exposed with 60 mJ/cm^2 at 405 nm with a chrome-on-quartz photomask (Photosciences) that had the chip and window pattern that would create windowed chips when the silicon was etched with KOH. The photoresist was developed with 1:4 AZ 340:DI water for 60 s and then rinsed and dried. The wafer was then dry etched in a Vision Reactive Ion Etcher (RIE) using a CHF_3/CF_4 recipe until the silicon nitride was removed. The photoresist was then stripped in DuPont EKC photoresist remover and the wafer was placed in a 30% KOH bath at 80 °C for 8 hours until the etching terminated at the silicon nitride window on the other side of the chip. Our fabrication scheme is outlined in **Scheme 4.2**.

4.2.3 Array Patterning

Following chip fabrication, the array was patterned into a resist. All array fabrication methods followed a general methodology as outlined in **Scheme 4.3**. This was performed with different patterns and three different exposure methods: masked photolithography, laser interference (holographic) lithography, and electron beam lithography.

In the case of masked photolithography, the wafer was left intact with a thin (~50 µm) layer of silicon left unetched on the backside of the chip to stabilize the wafer. Photoresist AZ 1512 was

spun at 4000 rpm for 60 s to a thickness of 1.2 µm and then prebaked at 110 °C for 60 s on a hotplate. A chrome-on-quartz photomask with 1, 2, 3, and 4 µm diameter electrodes with a 1 µm edge-to-edge spacing (Photosciences) was applied to the photoresist-coated top wafer surface and aligned with markers on the chip-patterned backside using an EVG 620 aligner. The mask and wafer were exposed with 60 mJ/cm^2 at 405 nm and the photoresist was developed with 1:4 AZ 340:DI water for 60 s and then rinsed and dried. The wafer was then dry etched in a Vision RIE using a CHF_3/CF_4 recipe until the silicon nitride was removed. The photoresist was then stripped in DuPont EKC photoresist remover, readying the chips and wafer for gold electrode fabrication.

For laser interference lithography individual fully-etched silicon nitride window chips were first oxidized with O_2 plasma in a Diener Femto plasma cleaner for 10 minutes. Chips then underwent a dehydration bake for 30 minutes at 200 °C to remove water from the surface immediately prior to spin coating with a 20% v/v solution of HMDS in PGMEA at 4000 rpm for 60 s. Then, a 2:1 PGMEA:AZ 1505 solution was spin coated at 4000 rpm to a thickness of 200 nm and prebaked at 110 °C for 60 s on a hotplate. The photoresist-coated window was then placed in a Lloyd's mirror interferometer and a 325 nm HeCd laser from Kimmon, Inc. was used to illuminate the mirror and substrate. The light from the laser aperture was expanded with a U-13X UV objective and filtered with a 900PH-10 high energy pinhole aperture, both from Newport and held in a Newport Model 900 spatial filter. The expanded and filter light was incident on both the sample and a Thorlabs PFSQ10-03-F01 UV enhanced aluminum mirror. After a typical exposure of 13 mJ/cm^2 the chip was developed in AZ 300 MIF for 60s and then rinsed and dried.

For electron beam lithography patterned arrays, a silicon nitride window chip had a 70 nm layer of aluminum evaporated onto it in a thermal evaporator to act as an etch stop layer for subsequent RIE. After aluminum evaporation, the chip was dehydration baked at 180 °C for 5

minutes then spin coated with a ZEP electron beam resist at 2000 rpm to a 175 nm thickness. After spin coating the chips were prebaked at 180 °C for 3 minutes. A JEOL JBX-6300FS Electron Beam Lithography System was used to pattern the ZEP resist on the chip with 30, 70, and 100 nm diameter electrodes with an equal sized pitch. Exposure dosage was calculate using BEAMER software from GenISys, GmbH. After exposure the chips were developed in amyl acetate for 2 minutes then rinsed in isopropanol before being dried. Following development, the chips were etched in an Oxford ICP Chlorine etcher to transfer the resist pattern to the underlying aluminum.

After patterning, all chips were etched in a Vision RIE using a CHF_3/CF_4 recipe until the array pattern was transferred to the 1000 nm thick silicon nitride window.

4.2.4 Array Fabrication

The transferred array pattern in the silicon nitride window is then filled with gold. There have been several methods which have evolved over the course of the project, including gold electrodeposition, gold galvanic displacement, gold evaporation, gold-titanium-gold evaporation, and combinations thereof.

Gold electrodeposition was performed in Orotemp $AuCN_2$ solution inside of a fume hood to minimize exposure to possibly generated cyanide gas. The reference/counter electrode used was a 250 µm diameter gold wire. Different waveforms were employed such as DC electrodeposition at large overpotentials such as 3 V and pulses between 0 V and a large overpotential at frequencies between 1 and 10 kHz. Depositions typically lasted a minute, but was dependent on the amount of overpotential with more overpotential giving faster deposition.

Gold galvanic displacement was carried out in solutions of dilute HF and $HAuCl_4$. HF concentration was varied between 100 mM and 600 mM to control deposition rate while $HAuCl_4$ was kept constant at 1 mM. The HF/$HAuCl_4$ solution was made in a plastic vial and the array was

submerged and held for 30 – 60 minutes with self-closing plastic tweezers by a ring stand. After the deposition, the array was removed and rinsed in two separate plastic vials containing DI water to ensure full dissolution of HF from the array.

Gold and titanium evaporation was performed in an electron beam evaporator. Two graphite crucibles containing the metal pellets separately were used to deposit gold and titanium sequentially without breaking vacuum. Deposition rates of 1.0 Å/s were used for both metals.

KOH etching following gold electrode fabrication was carried out in 30% w/w% KOH in DI water. A 6-inch glass crystallizing dish was used to contain the solution and individual array chips were submerged into the bath with self-closing plastic tweezers held by a ring stand. A IKA C-MAG HS 7 hot plate with thermometer was used to control heating such that a temperature of 80 °C was maintained. A 2 inch stir bar was used to induce convection within the bath to prevent formation of bubbles which would mask etching. With these bath parameters the etch rate for silicon was 1.25 µm/min and the etching was performed for approximately 75 minutes. After removing the array from the KOH bath, it was rinsed twice in separate DI water containers before being rinsed with isopropanol to hasten drying.

4.2.5 Fluorescence Measurements

Fluorescence imaging of arrays was carried out with an Olympus IX70 inverted microscope with a 20x objective (Olympus LCPlanFl 20X/0.40 Ph1) with an additional 1.5x magnification. Fluorescence was excited with a Thorlabs M530L2 LED and filtered using a HQ535/50 excitation filter, HQ610/75 emission filter, and Q565lp dichroic mirror. Optical data was collected with and Andor iXon+ EMCCD camera and Andor software. Electrical recordings were performed in LabVIEW with a National Instruments PCI-6281 DAQ card. Cyclic voltammetry was performed using analog output with the same National Instruments software and

card with a trigger that initiated optical and electrical recording and output simultaneously. CVs were performed in a two-electrode setup with the array as the working electrode and a Ag/AgCl quasi-reference electrode as a reference/counter. The CV was taken in a solution of 100 µM resazurin with 50 mM phosphate buffered to pH 7.5. CV parameters were an initial potential of 0 V and sweeping to -0.8 V at a scan rate of 200 mV/s.

4.3 Results and Discussion

4.3.1 Silicon Nitride Window Chip Fabrication

The foundation of each bipolar electrode array outlined hereafter is a silicon nitride window chip. This is a 500 µm thick silicon chip, insulated on either side with a thin 50 – 1000 nm layer of silicon nitride, a material with properties similar to silicon oxide, or glass. However, there are notable differences such as chemical resistivity, resistivity, and film stress. For the purposes of array fabrication, the most important difference is the superior resistance to KOH and HF of silicon nitride over silicon oxide.[11] These harsh chemicals are used during the fabrication of the chip and of the subsequent array for which silicon nitride is used instead of silicon oxide.

The silicon nitride window chip, insulated on either side, has a window comprised of the silicon nitride on one side. This is a section of the chip, typically in the middle of the chip, where the underlying silicon has been etched away from the back side of the chip through to the front side. Here the front side of the chip refers to the side with the window. The removal of all silicon leaves just the nanometer-thin layer of silicon nitride suspended across the chip over an area that is typically 50 µm x 50 µm or less. This type of chip is used ubiquitously in the nanoscience field for purposes as varied as a substrate for tunneling electron microscope imaging to a platform for creating nanopores.

4.3.2 Photolithography Array Fabrication

The photomasked array patterns produced the largest electrodes ranging from 1 – 4 μm in diameter with an edge-to-edge spacing of 1 μm. Despite being similar in dimensions to the original carbon fiber electrode arrays they do offer several key advantages over previous arrays in terms of cross-talk, size, and electrode material.

Exposure dosage was critical to the fabrication of photomasked arrays. The close spacing of holes in the photomask created exposure overlap between electrodes. This effect caused trenches to develop between electrodes if the photoresist was overexposed. The overexposure effect differed among different sized electrodes as the larger holes allowed more light to pass than the smaller ones. This meant that the exposure dosage had to be optimized for each differently sized electrode array. With each size being on the same photomask there was then a region of the wafer that came out unusable with some quadrants of the wafer, representing differently sized arrays, being either overexposed or underexposed. However, we believe this method was preferable to making several different masks for each size of electrode array. Each array occupied an area of 1x1 mm^2 which allowed a high density of arrays on each wafer. This created 40 arrays of each size per wafer, a number sufficient for studies. Moreover, each wafer produced usable arrays of different sizes, enabling us to work on differently sized arrays after fabricating just one wafer. The high resolution of the photomask, especially the 1 and 2 μm electrodes, created a high cost associated with its fabrication. Making several photomasks would have tripled or quadrupled this initial cost, amounting to thousands of dollars.

To use the photomask the wafer had to be intact for spin coating and exposure. This allowed us to spin coat and expose over a hundred arrays at once. However, prior to this step the wafer was etched most of the way through, leaving a 75 μm thick silicon backing which connected the chip. This rendered the wafer extremely fragile and had to be treated with care. A vacuum is applied to

the back of the wafer during spin coating and exposure with the mask aligner for immobilization. If the wafer were thinned too much in the previous step this would cause it to shatter upon vacuum application. Additionally, the etched chip pattern prevented a seal on the back of the wafer. Wafer tape was stuck to the back of the wafer and created an air tight seal that allowed the wafer to be held with vacuum.

DC electrodeposition at large overpotentials such as 3 V deposited gold quickly, however this often led to bowl-shaped electrodes which had an increased thickness of gold around the periphery of the electrode as shown in **Figure 4.1**. This electrode profile is a natural consequence of the diffusion of gold ions in solution primarily to the edge of the electrode. This electrode profile could prove beneficial if the electrode were overgrown to form a 'cap' around the surrounding edge of the insulating membrane that prevents it from falling out during later steps. This strategy was attempted but with limited success, primarily due to the stochastic nature of deposition across the array. Deposition across thousands of electrodes was non-uniform and sub-nanometer control over deposition thickness proved too challenging.

The mechanism of galvanic displacement of gold proceeded via the oxidation and displacement of silicon with the reduction of gold ions in solution onto the silicon surface. It occurs via the two following half-cell reactions:[12,13]

$$Si + 6\,F^- \rightarrow SiF_6 + 4\,e^-$$

$$AuCl_4^- + 3\,e^- \rightarrow Au + 4\,Cl^-$$

In addition to solubilizing the silicon oxidation products, HF served to dissolve the passivating silicon oxide layer that forms upon the exposure of silicon metal to air or water.[14] This mechanism can apply to other metals such as Pt. [15] A side effect of the galvanic displacement reactions was the etching of the silicon nitride membrane by the HF, despite its dilute

concentration. Given that the HF was so dilute, we estimate the etching over a 30 minute reaction to be negligible and on the order of 10s of nanometers from the 1000 nm thick window.[11] The results of a gold galvanic displacement in concentration of 100, 300, and 600 mM HF and 1 mM $HAuCl_4$ for 30 minutes is show in **Figure 4.2**. The exposed silicon at the bottom of the patterned and etched array has been converted into gold. This transformation results in a porous and rough gold layer. The dependence on the diffusion of $AuCl_4^-$ ions to the silicon is evident in the accelerated gold growth at the edges of the array and the edges of individual electrodes within the array, similar to the gold electrodeposition showcased in the previous section.

The growth rate of gold in the displacement reactions was dependent on both the concentration of HF and $HAuCl_4$, as well as pH.[12] Additionally, as the growth becomes diffusion limited, convection can be introduced by stirring to increase the growth rate.[16] For our experiments, only stirring and variations in HF concentration were tried. The growth rate of gold increased greatly from 100 mM HF to 300 mM HF as seen in **Figure 4.2**. However, further increase of the HF concentration did not appear to increase the gold growth rate. The likely culprit for this plateau in growth rate is a limitation in the availability of $AuCl_4^-$ ions, the concentration of which was not increased.

Further examination of the SEM images reveals that the slow growth rate associated with the 100 mM HF case did not yield a smoother or more evenly distributed gold film, but in fact appears to grow in the same manner as higher concentration cases. This is a major drawback to the efficacy of this gold growth method, as we were unable to fabricate non-porous, smooth gold electrodes. This is problematic because later electrochemical testing requires a sealed, or closed, bipolar electrode to effectively couple electrochemical reactions.

KOH etching was employed to dissolve the silicon underlying the window, allowing the electrode array to function in a bipolar electrochemical manner. This requires submerging the entire array chip with gold electrodes into an 80 °C KOH bath for over an hour. We found these harsh conditions did not damage the silicon nitride, however all arrays subjected to this process had missing electrodes after finishing the KOH etch. An example of a fully fabricated array is shown in **Figure 4.3**. The galvanic displacement of gold into the bare electrodes is shown in before and after optical images in **Figure 4.3a-b**. We would like to emphasize the uniformity of gold growth at this stage, as nearly all electrodes in the array have gold. It should also be noted that these electrodes individually look whole at the microscopic scale, but at the nanoscopic scale are still porous as shown previously in SEM imaging. Following the galvanic displacement of gold into the electrode recesses the array has been submerged into a KOH bath to remove all underlying silicon.

Optical images in reflection and transmission mode are shown in **Figure 4.3c** and **Figure 4.3d** respectively. The use of both light modes of our microscope allows us to identify features on and in the array, such as filled electrodes, missing electrodes, and aggregated electrodes that have fallen out of their recesses. Filled electrodes appear as golden circles in reflectance mode, and as black circles in transmission mode as they prevent light from passing through to the objective. Missing electrode recesses appear dark in reflectance mode due to the lack of a metallic reflector and appear bright in transmission mode because there is nothing to prevent the passage of light. From the optical images it is clear that a large proportion of the gold electrodes have fallen out, especially in the top right corner of the image which lies furthest away from the array edge. In fact, this was a common result from this fabrication method and most arrays produced in this manner had 10-30% of their electrodes missing.

Missing electrodes were more likely to be found away from the array edge and especially the corners. We again return to the diffusional flux of $AuCl_4^-$ ions to the electrode, which is higher at the edges than in the center. The increased flux results in more gold growth at the edges which is apparent in images of the arrays after growth. This stabilizes the electrodes at the edges of the array by increasing the surface area of gold adhering to the silicon nitride sidewalls. Another likely cause of the increased electrode retention at the array edges is the possibility of gold interconnecting between electrodes, preventing the electrodes from falling out but also making them cross-talk.

The smallest electrode features created with this method were 1 μm in diameter. These holes in the photoresist were transferred into a 1 μm thick silicon nitride window, later creating electrodes with an aspect ratio of 1. Electrodes of larger diameter had an even lower aspect ratio. The lack of a high aspect ratio is considered to be important reason for the gold electrodes falling out of their positions in the array.

Perhaps the most important reason for the failure of these arrays is the lack of an adhesion layer to connect the gold electrodes to the silicon nitride window. As a noble metal, gold does not adhere well to other materials, and this is a notable problem in microfabrication of electrical structures. Typically, an adhesion layer such as chromium or titanium is used between gold and the underlying substrate, as these metals will adhere well with noble metals and other materials such as silicon nitride. For the electrodeposition and galvanic displacement methods used for the photoresist masked array there was never an adhesion layer employed. Later methods involving evaporation will use titanium as a sandwich layer between two gold electrodes on the poles of the array to promote adhesion of gold to the silicon nitride.

4.3.3 Laser Interference Lithography Array Fabrication

Laser interference lithography was carried out in a Lloyd's mirror configuration as shown in **Figure 4.4a**. In this setup, the laser light was spatially filtered and expanded onto a 90° machinist's block holding a mirror and the photoresist-covered substrate. The angle of incidence of laser light onto the exposure setup controlled the interference fringe spacing and eventually the period of the array through the following equation,[17]

$$\Lambda = \frac{\lambda}{2\sin(\theta)}$$

Where Λ is the period of the interference fringe pattern, λ is the wavelength of laser light, and θ is the angle of incidence onto the substrate. The interference pattern could be changed from a fringe pattern to a grid pattern by rotating the substrate 90° mid-exposure as shown in **Figure 4.4b**. In this way, the two fringe patterns would not have enough dosage to create a pattern in the photoresist aside from where they overlap, creating a square grid array like the one shown in **Figure 4.4c**. This was employed to generate the electrode array pattern in a thin photoresist. Other rotations and fractional exposures can produce hexagonal arrays with more densely packed electrodes, but this was not attempted.

Exposure dosage was difficult to control by hand, but use of a timed shutter could produce reproducible results. Because our exposures were carried out by hand it was useful to have a low light intensity at the substrate surface and our experiments typically had a power density of around 100 μW/cm^2 as measured with a power meter. Typical exposure dosages were around 13.0 mJ/cm^2 which resulted in exposure times of two minutes or more. This long exposure time made variations due to human error in shutter control negligible, as a 0.5 s difference from run to run would only amount to an increased exposure dosage of 0.05 mJ/cm^2.

A thin layer of photoresist on the order of 200 nm is required to properly employ laser interference lithography without an anti-reflection coating. While the fringe pattern resulting from interference across the face of the photoresist has been discussed, the interference within the photoresist because of reflection from the underlying material has not. A fringe pattern will result from this interaction if anti-reflection coating is not used, creating a scalloped profile in the electrode holes that rises perpendicular to the surface of the material underlying the photoresist. This scalloped profile is not stable, and will topple during photoresist development. One way to avoid this, and the one employed in our experiments, is to make the photoresist thin enough to be less than the period of the interference pattern resulting from the underlying material reflection.

Centering the expanded laser beam was a critical factor in obtaining reproducible and quality patterns. The Gaussian profile of the expanded laser needed its center to be positioned where the substrate and mirror met to maximize fringe contrast. If the incident laser light or reflected laser light from the mirror were significantly more powerful than the other, there would be poor destructive interference. Experimentally, this results in a poor contrast between the minima, or electrode holes, and maxima, or the space between electrode holes. The difficulty of creating an electrode array from a pattern with poor contrast cannot be overstated, as the already thin photoresist would need to be etched even further to lower the pattern down to the material below. If the difference between maxima and minima is low, as in a case of poor contrast, then this because harder, often requiring control within tens of nanometers.

Another important consideration when using laser interference lithography is the adhesion of photoresist to the underlying material. In our case, the underlying material was silicon nitride, although we are also planning to evaporate chromium onto the silicon nitride before spin coating photoresist for use as an etch mask. We begin first with understanding the surface of the silicon

nitride, which contains some degree of silanol groups due to a few monolayers of silicon oxide that form upon exposure to air. We maximized the density of silanol groups on the silicon nitride surface by oxidizing it in O_2 plasma for 10 minutes. The silicon nitride was then primed with a common chemical used in microfabrication, HMDS. This silazane reacts with silanol groups on the silicon nitride surface, creating a hydrophobic substrate which the photoresist will more robustly adhere to. It is important to realize that HMDS also reacts with water, and that the silanol groups on the surface will also be hydrophilic prior to functionalization and will have a thin layer of moisture adhered to them. The dehydrating bake step to remove this water layer prior to functionalization was critical, to ensure that the HMDS reacted with silanol groups on the silicon nitride surface, and not water molecules.

We found dust contamination of the chip surface to be an annoying, but not unassailable problem associated with fabrication. The laser interference lithography patterning occurred in our lab, outside of a cleanroom, and thus a non-zero quantity of dust did appear on chips. However, this can be mitigated by careful handling of the chip throughout the patterning process, and by covering the chips whenever possible. Dust inevitably was found on our chips, but had a low probability of landing on the 50 x 50 μm^2 window in the center of the chip. The pattern above the window was the only part of the pattern used in array fabrication, and therefore dust elsewhere was disregarded.

4.3.4 Electron Beam Lithography Array Fabrication

Electron beam lithography proved to be the most reproducible patterning method attempted. It also gave the highest resolution patterns, down to well-defined 70 nm diameter electrodes with a 70 nm pitch as shown in **Figure 4.5**. These attributes did not come without cost however, as this method was also the most expensive used, with a cost of several hundred dollars

to pattern a few silicon nitride window chips. This cost could be mitigated by increasing the amount of patterning done during a session, such as by patterning an entire wafer with multiple array patterns and then etching it into individual array chips.

Several problems were encountered during electron beam lithography pattern transfer. The resulting 70 nm electrodes, when fully transferred to the silicon nitride window, would have an aspect ratio of over 10. Etching features with this high of an aspect ratio with RIE is challenging, and other methods such as deep reactive ion etching have been employed. Our attempts at etching these features into the window resulted in a downwardly expanding cone due to heat accumulation in the poorly thermally conductive silicon nitride window. To address this, future arrays will be patterned on smaller windows, and will be etched using lower power plasmas.

4.3.5 Fluorescence Measurements

Of the array patterning methods attempted, only the masked photolithography arrays have made it to a stage where it was possible to test electrochemically and optically. An example of fluorescence imaging using an array is shown in **Figure 4.6**. We could resolve individual electrodes in these arrays down to 1 μm electrode diameter. There is a fundamental limitation to the resolution of these electrode arrays that is higher than the diffraction limit. This limitation is caused by the diffusion of the generated fluorescent product at the electrode. We can calculate that it would approximately take 1 ms for a fluorescent molecule to diffuse from the edge of one electrode to another using the equation $t = \frac{d^2}{2D}$ where d is the distance to diffuse, in this case 1 μm, and D is the diffusion coefficient 4.8×10^{-6} cm^2/s.[18] This 1 ms time frame is beyond our optical time resolution and results in a blurring effect where non-active electrodes in proximity to an active one can appear to have generated fluorescent molecules.

4.4 Conclusions

Electrochemical imaging is a growing field due to its sub-diffraction limit resolution and chemical sensitivity. However, several factors affect its viability such as temporal resolution and field of view. FEEM a new electrochemical imaging technique, was developed in our lab to address these issues and ultimately image neuronal communication between human neurons. Toward this goal we have been developing new arrays of bipolar electrodes that are smaller, more densely packed, and more uniform than previous ones. Several methods have been attempted, with some more successful than others. Development of these new arrays is promising and continues.

4.5 Schemes and Figures

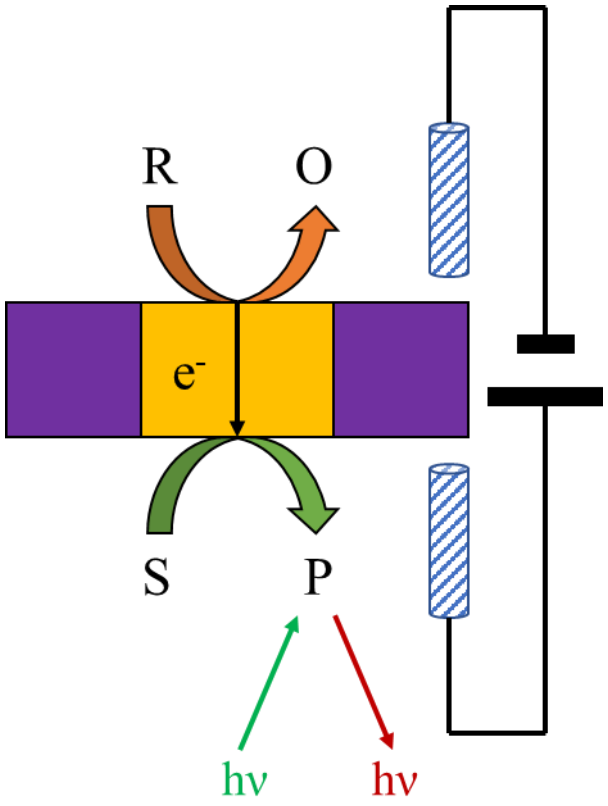

Scheme 4.1. Bipolar electrochemistry and FEEM.

A bipolar electrode is an electrode enclosed within an insulator and exposed to two separate solutions at either of its poles. A pair of driving electrodes, typically Ag/AgCl quasi-reference electrodes, is then placed into either of the solutions. A voltage is applied across the bipolar electrode using the driving electrodes and four electrochemical reactions happen simultaneously within the cell. The Ag/AgCl half-reactions at either driving electrode occur but are not shown above for clarity. An electrochemical oxidation reaction of interest occurs at the top pole and is coupled to an electrochemical reduction reaction of a fluorogenic molecule at the bottom pole. When reduced, this now fluorescent molecule can be excited measured optically with a camera. For FEEM, this is generalized to tens of thousands of closed bipolar electrodes all driven by a single pair of electrodes.

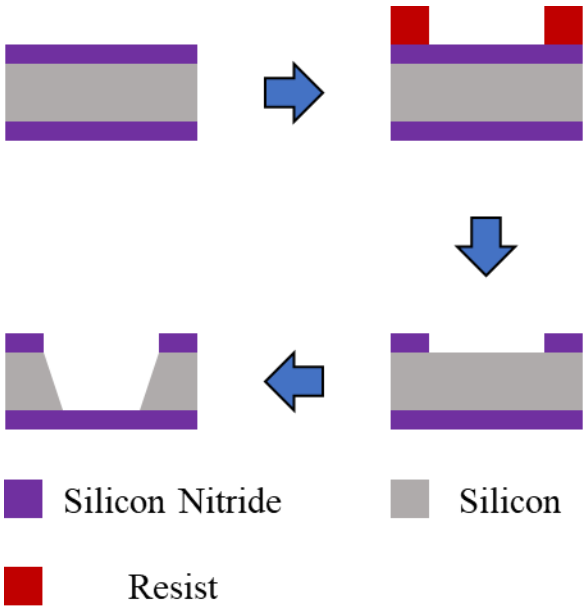

Scheme 4.2. Silicon nitride window chip fabrication.

(Top) Silicon nitride window chip fabrication scheme. (Bottom) Optical image of a fabricated chip.

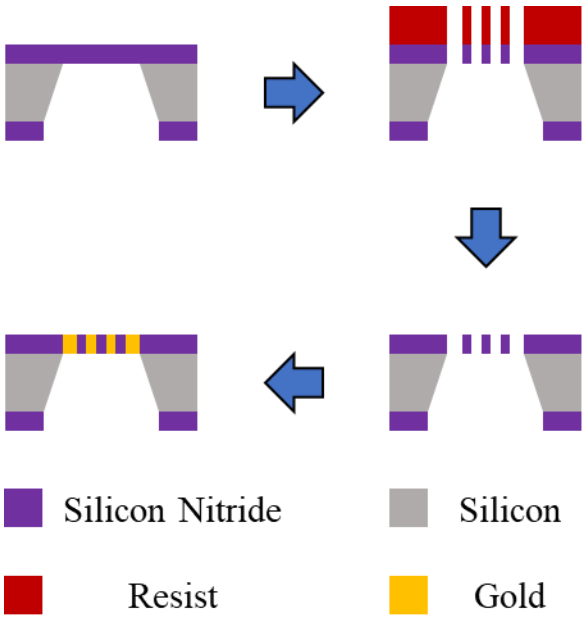

Scheme 4.3. Array fabrication scheme.

All array fabrication begins with a silicon nitride window chip. There were three types of resist patterning methods tried: masked photolithography, laser interference (holographic) lithography, and electron beam lithography. Each patterning step resulted in an array pattern across the window of the chip. The pattern is then transferred to the underlying silicon nitride window through RIE. Finally, the hole pattern is filled with gold to produce gold electrodes using either electrodeposition, galvanic displacement, or evaporation.

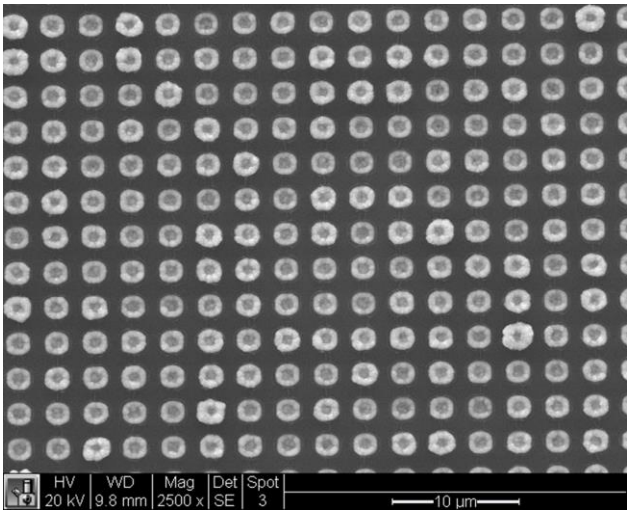

Figure 4.1. Gold electrode arrays after DC electrodeposition.

Example of an array of 2 µm diameter gold electrodes after DC electrodeposition of $HAuCl_4$.

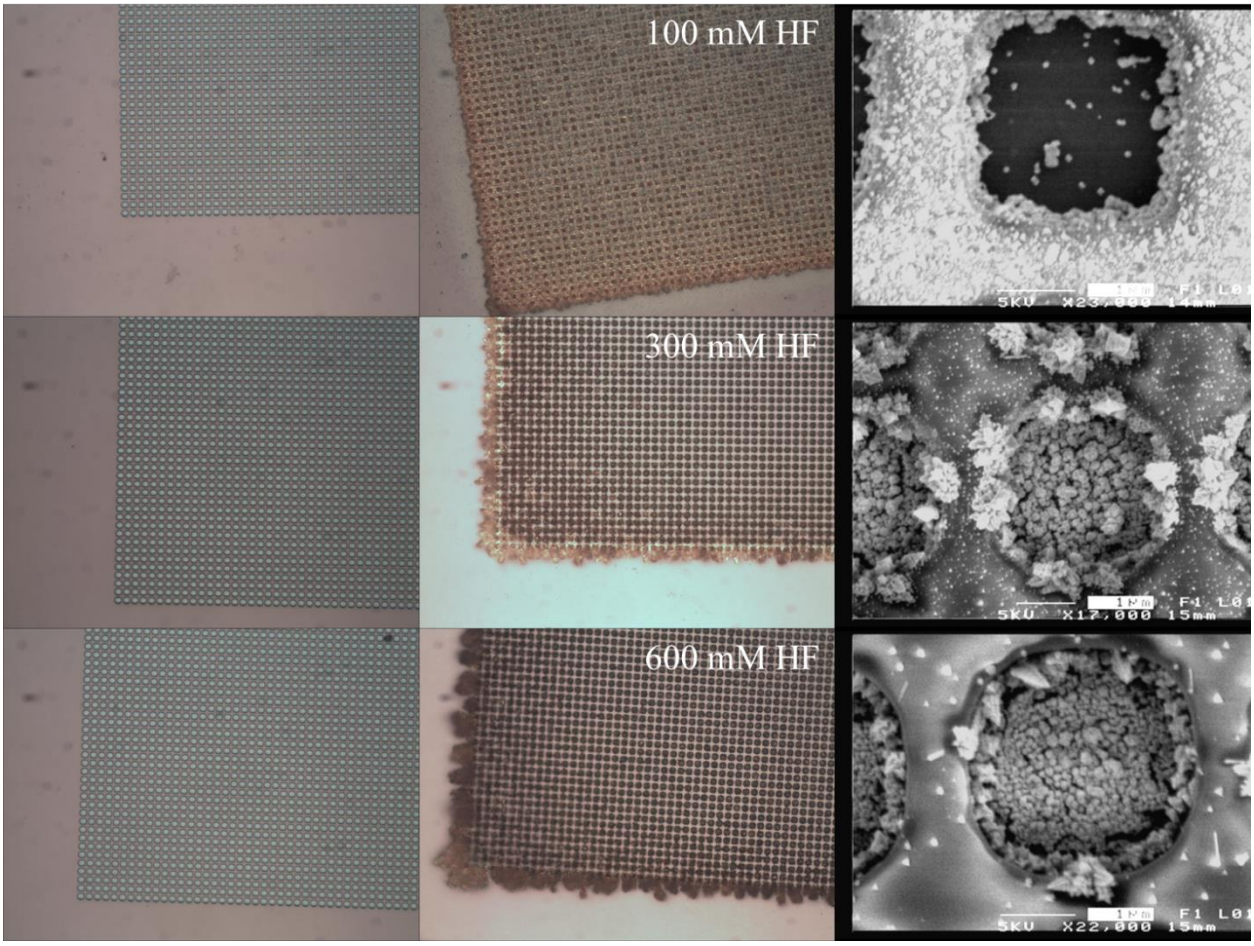

Figure 4.2. Gold galvanic displacement reactions at different HF concentrations.

(Left column) Optical images of 2 μm diameter silicon electrodes after patterning and etching. (Middle column) The silicon has been displaced by gold in a displacement reaction that ran for 30 minutes in a solution of the concentration of HF labeled and 1 mM $HAuCl_4$. (Right column) SEM images of the gold electrodes after displacement reactions.

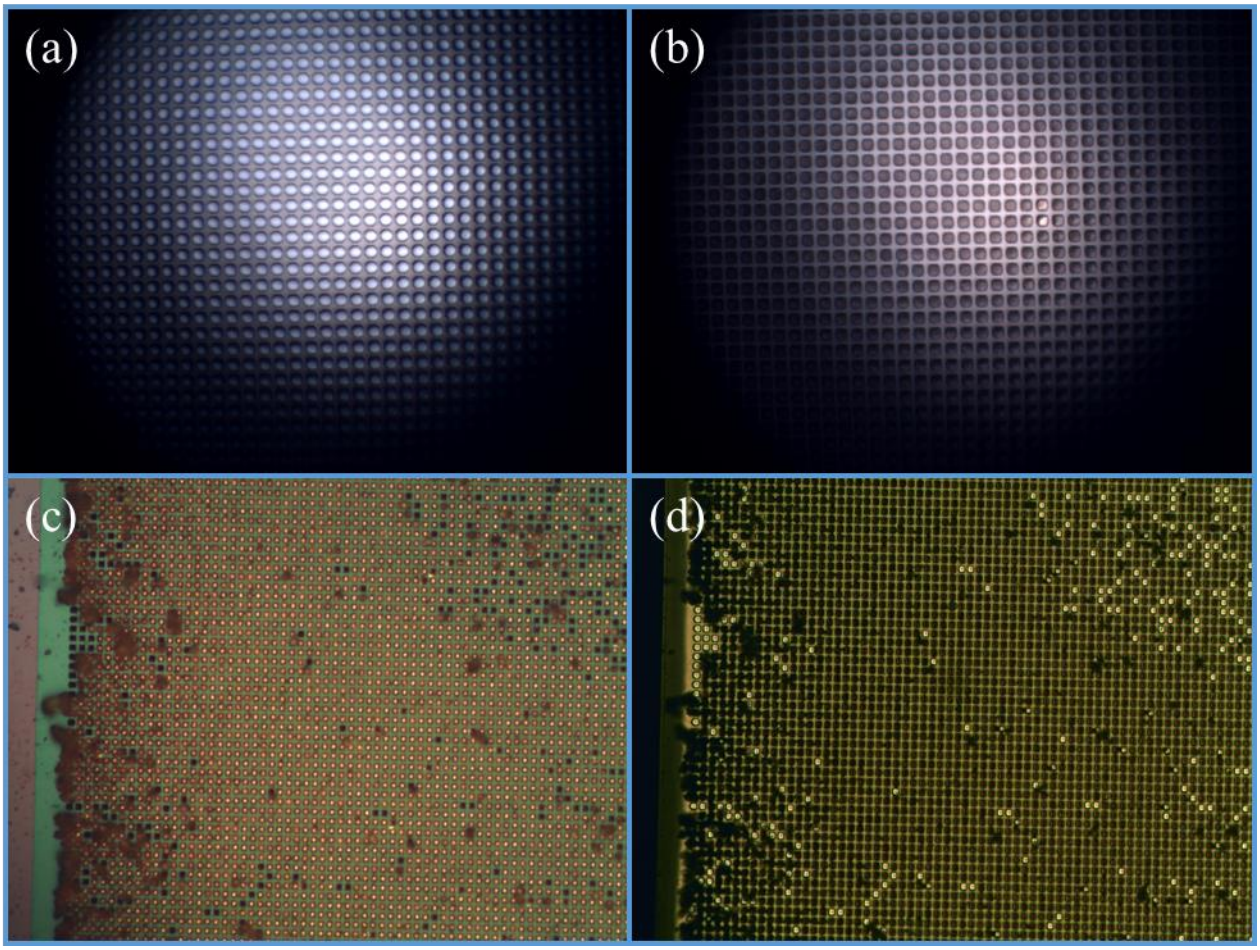

Figure 4.3. Photolithography array patterning.

(a) Image of photomask patterned array. (b) Image of gold-filled array after gold galvanic displacement. (c) Reflectance image of gold-filled array after KOH etching. (d) Transmission image of gold-filled array after KOH etching.

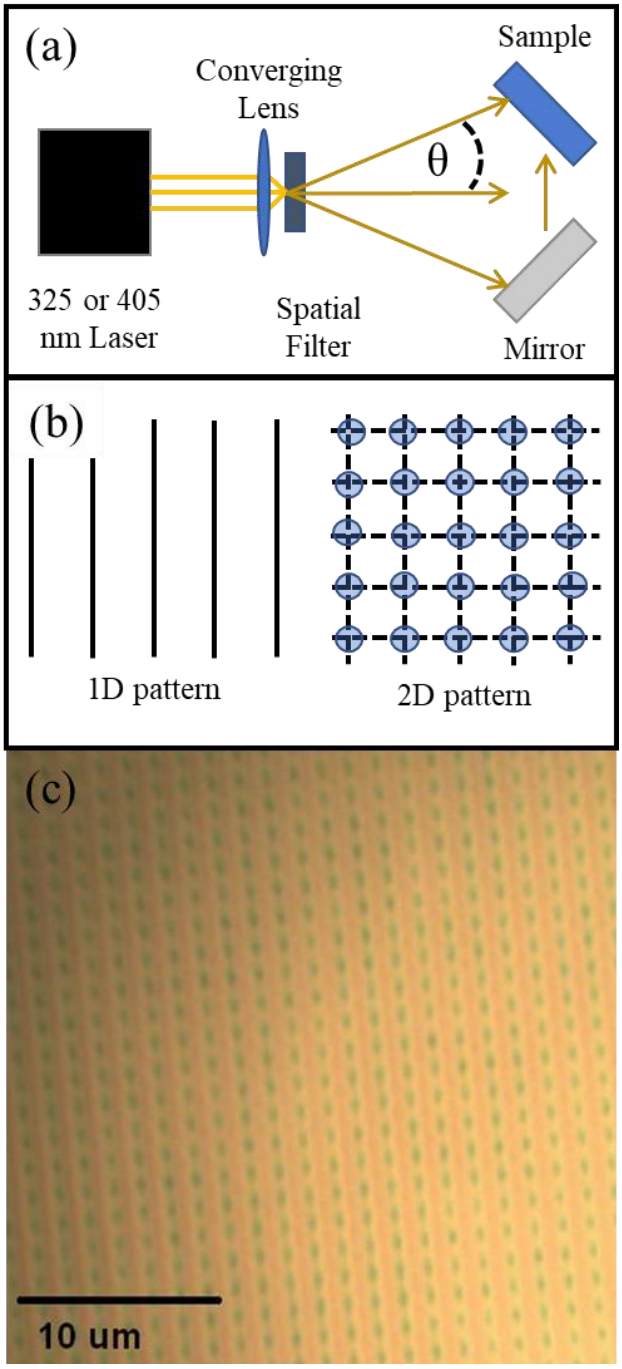

Figure 4.4. Laser interference lithography array patterning.

(a) Lloyd's mirror exposure configuration. Light from a 325 nm HeCd laser was focused by an objective through a spatial filter before expanding onto a 90° machinist's block holding a mirror and photoresist-covered silicon chip. The period of the resulting interference pattern is modulated

by θ, the angle of laser light incidence. (b) Exposure methodology. Rotating the substrate 90° on the machinist's block mid-exposure resulted in a square array pattern where maximum dosage occurred where the two interference patterns overlapped. (c) An optical reflectance microscope image of a laser interference lithography pattern with a period of approximately 1200 nm.

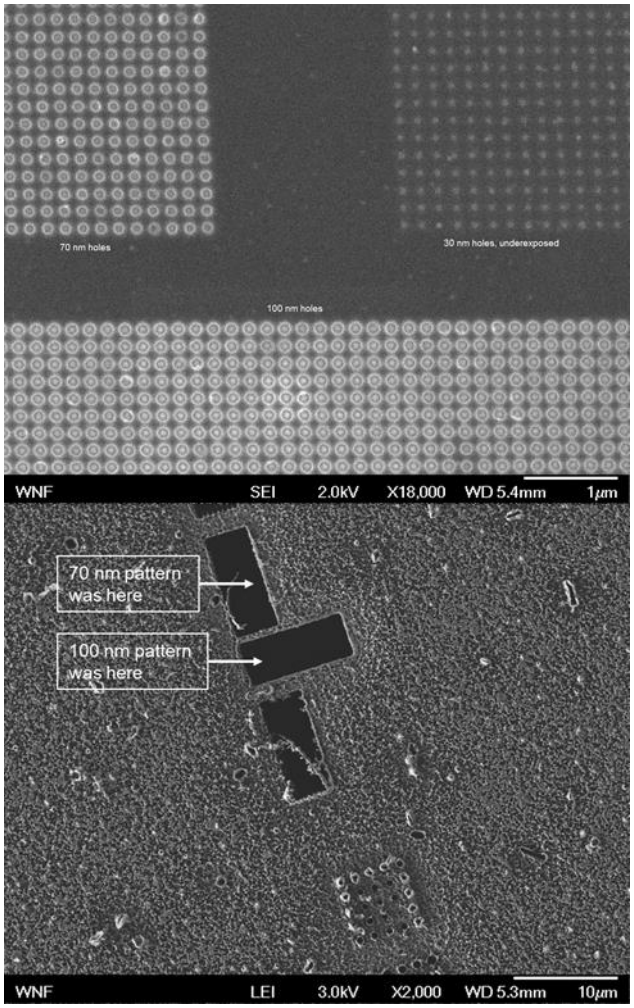

Figure 4.5. Electron beam lithography array patterning.

Image of electron beam lithography patterned array.

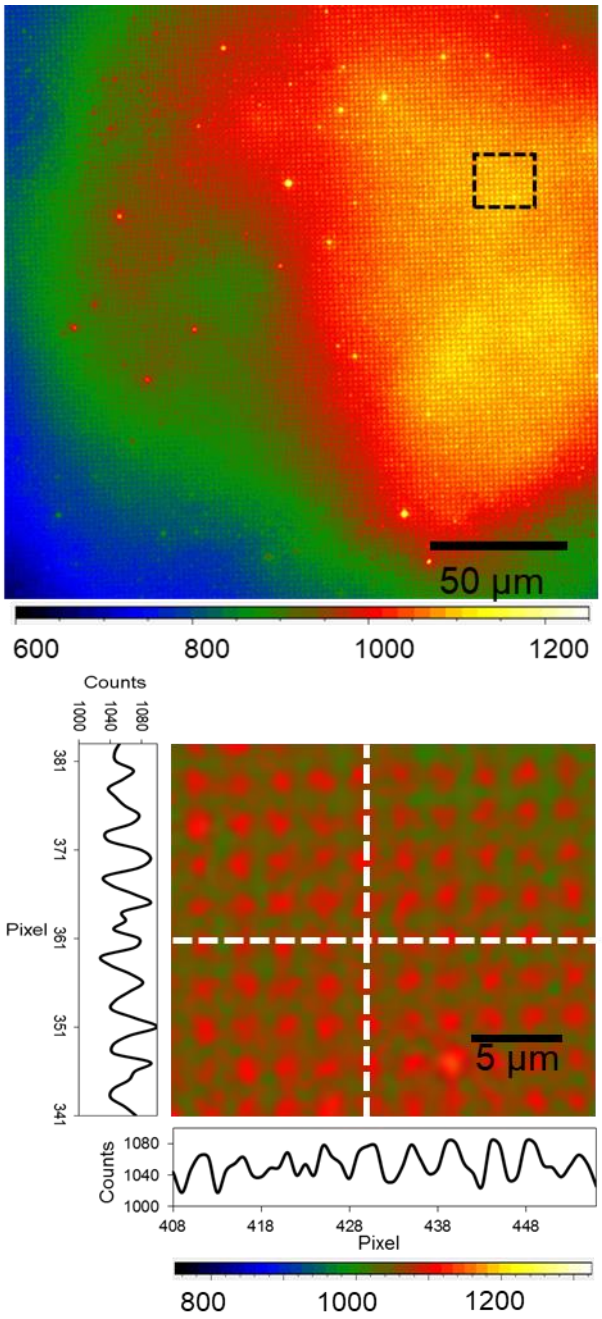

Figure 4.6. Fluorescence imaging.

Image of an array of 1 µm diameter electrodes during fluorescence imaging. The bottom image shows the spatial resolution obtained with such an array.

4.6 References

(1) Liu, H.-Y.; Fan, F.-R. F.; Lin, C. W.; Bard, A. J. *J. Am. Chem. Soc.* **1986**, *108*, 3838-3839.

(2) Bard, A. J.; Fan, F.-R. F.; Kwak, J.; Lev, O. *Anal. Chem.* **1989**, *61*, 132-138.

(3) Kwak, J.; Bard, A. J. *Anal. Chem.* **1989**, *61*, 1221-1227.

(4) Chen, C.-C.; Zhou, Y.; Baker, L. *Annu. Rev. Anal. Chem.* **2012**, *5*, 207-228.

(5) Butt, H.-J.; Cappella, B.; Kappl, M. *Surf. Sci. Rep.* **2005**, *59*, 1-152.

(6) Zhang, B.; Adams, K. L.; Luber, S. J.; Eves, D. J.; Heien, M. L.; Ewing, A. G. *Anal. Chem.* **2008**, *80*, 1394–1400.

(7) Abe, H.; Ino, K.; Li, C. Z.; Kanno, Y.; Inoue, K. Y.; Suda, A.; Kunikata, R.; Matsudaira, M.; Takahashi, Y.; Shiku, H.; Matsue, T. *Anal. Chem*. **2015**, *87*, 6364–6370.

(8) Guerrette, J. P.; Percival, S. J.; Zhang, B. *J. Am. Chem. Soc.* **2013**, *135*, 855-861.

(9) Guerrette, J. P.; Oja, S. M.; Zhang, B. *Anal. Chem.* **2012**, *84*, 1609-1616.

(10) Cox, J. T.; Gunderson, C. G.; Zhang, B. *Electroanalysis* **2013**, *25*, 2151-2158.

(11) William, K. R.; Gupta, K.; Wasilik, M. *J. Microelectromech. S.* **2003**, *6*, 761-778.

(12) Gutes, A.; Laboriante, I.; Carraro, C.; Maboudian, R. *J. Phys. Chem. C* **2009**, *113*, 16939-16944.

(13) Miyake, H.; Ye, S.; Osawa, M. *Electrochem. Commun.* **2002**, *4*, 973-977.

(14) Morita, M.; Ohmi, T.; Kawakami, H. M.; Ohwada, M. *J. Appl. Phys.* **1990**, *68*, 1272-1281.

(15) Magagnin, L.; Maboudian, R.; Carraro, C. *J. Phys. Chem. B* **2002**, *106*, 401-407.

(16) daRosa, C. P.; Iglesia, E.; Maboudian, R. *Electrochim. Acta* **2009**, *12*, 3270-3277.

(17) van Wolferen, H.; Abelmann, L. Laser Interference Lithography. In *Lithography: Principles, Processes, and Materials;* Hennessey, T. A., Nova Science Publishers, 2011.

(18) Oja, S. M.; Guerrette, J. P.; David, M. R.; Zhang, B. *Anal. Chem.* **2014**, *86*, 6040-6048.

Chapter 5. Laser-Pulled Nanopipettes for Studying Oil Emulsion Translocation Dynamics

5.1 Introduction

Nanopores are nanoscale pores that act as sensors[1] for various analytes from small molecules[2,3] and viruses[4,5] to single-stranded DNA[6-9] and RNA[10] to even larger nanoparticles.[11,12] Nanopore sensors normally operate on a resistive-pulse mechanism, also known as the Coulter counter method.[13] In resistive-pulse measurements, one normally holds a constant voltage across the nanopore membrane while measuring the ionic current passing through the pore over time. A transient change in the ionic current is anticipated when an analyte particle translocates through the nanopore providing critical information about the analyte particle, such as shape, electrophoretic mobility, charge, and size. A slight decrease in the current is often observed due to a particle partially blocking the flow of the ions. The detection frequency can be used to analyze particle concentration. Based on the shape and duration of the current pulse, one can also obtain information about the pore geometry.[14]

Here we use the resistive-pulse mechanism to observe the translocation dynamic of a soft nanoparticle. Soft particles such as liposomes,[15,16] microgels,[17] and oil emulsions,[18] have been studied previously using nanopores. The elasticity of soft particles permits particles which are larger than the nanopore to pass through the orifice.[15] Elastic deformation of soft particles can also occur in the concentrated electric field at the nanopore orifice.[19,20] The structure of soft nanoparticles can result in a separate volume within the particle with contents that can differ from that of the outside electrolyte solution.[21] The soft nanoparticle we use is an emulsion droplet based on chemistry described previously.[22] This emulsion droplet is toluene that is mixed and emulsified

with an ionic liquid. The ionic liquid acts as an emulsifier to provide stability through particle surface charge as well as an electrolyte to increase the conductivity of the droplet.

In this article, we first observe, characterize, and analyze the phenomenon of agglomeration at the nanopore orifice. We then use this phenomenon to trap a droplet in the orifice with a highly resistive seal to perform voltammetry. The ion transfer voltammogram is obtained and explained to demonstrate the capability of this method for repeatable electrochemical interrogation of a solitary attoliter oil droplet volume. Finally, a lipophilic dye is added to the droplet and the phenomenon is monitored with fluorescence microscopy in real time.

5.2 Experimental

5.2.1 Laser-Pulled Nanopipette Fabrication

Quartz pipette pores were fabricated using a P-2000 laser puller (Sutter Instrument). Quartz capillaries of dimensions 0.7 mm inner diameter, 1.0 mm outer diameter with filament (Sutter Instrument) were rinsed with isopropanol and dried prior to laser-pulling with a previously reported recipe.[23] Pulling parameters were: heat 450-470, filament 1, velocity 30, delay 145, pull 175 where a higher heat parameter resulted in a smaller diameter nanopipette. Nanopores were electrically tested in 5 mM tetrabutylammonium chloride (TBACl, 97%, Sigma-Aldrich) that had been filtered through a 200-nm PTFE syringe filter prior to emulsion droplet experiments. The inside of the nanopipette was filled with 5 mM TBACl solution and the submerged in a 5 mM TBACl solution. Ag/AgCl quasi-reference electrodes (QRE) were made by leaving 0.5 mm silver wire (Alfa-Aesar) in ultra-bleach (Tough Guy brand) until the wires turned a noticeable shade of purple-grey. The Ag/AgCl QREs were then placed into the back of the nanopipette and the 5 mM TBACl solution. The potential was controlled by an EG&G PAR Model 175 function generator connected to a Dagan Chem-Clamp potentiostat. The potentiostat was interfaced to a PC through

a National Instruments 6281 DAQ card and a National Instruments BNC-2120 breakup box with signal data recorded with a homemade LabVIEW program. The potential was scanned between -1 V and +1 V at 100 mV/s until a stable *i*-V response was produced. All potentials in this work were applied inside the nanopipette relative to the outside.

5.2.2 Emulsion Preparation and Characterization

The emulsion was created from toluene (Fisher Scientific) and the ionic liquid trihexyl-tetradecylphosphonium bis(trifluoromethylsulfonyl)amide (IL-PA, 95%, Sigma-Aldrich) using a procedure modified from elsewhere.[22] Briefly, 56 µL of IL-PA was added to 200 µL of toluene and mixed to create a 400 mM IL-PA in toluene solution. This solution was added to 10 mL of 200-nm-filtered 5 mM TBACl in DI H_2O. This combined solution was vortexed for 20 s then immediately ultra-sonicated at 10 W for 60 s by a QSonica XL-2000 probe sonicator. The resulting emulsion was milky white and was immediately diluted to the desired concentration in 200-nm-filtered 5 mM TBACl. The 5 mM TBACl solution outside of the nanopipette was replaced with the diluted emulsion solution in 5 mM TBACl. Following amperometry each emulsion solution was characterized with a NanoSight LM10 (Malvern) to measure the size distribution and ensure that it matched previous size data.

5.2.3 Electrochemical Measurements

For recording amperometry of emulsion droplets the Dagan Chem-Clamp was interfaced to a Digidata 1440A digitizer (Molecular Devices) which was connected to a PC through USB. Amperometry was recorded using Axoscope 10.2 software with a sampling frequency of 50-kHz using a 10-kHz low-pass filter on the Dagan Chem-Clamp.

5.2.4 Data Analysis

Prior to analysis, every 50 points of the current-time traces were averaged to increase the signal-to-raise ratio to resolve the few-pA current steps. Steps were analyzed using a script written in *R* that used a changepoint detection algorithm made available as a package.[24] After changepoint detection the results were compared with the raw data to ensure that changepoints were placed accurately. Python and its modules Matplotlib, NumPy, and tifffile were used to construct videos displaying voltage, ionic current, and mean fluorescence counts along with recorded camera frames simultaneously.

5.2.5 Simultaneous Electrical and Optical Recording

Electrical recordings were made with the same equipment outlined previously. The simultaneous optical recording was made with a Nikon Eclipe Ti microscope with a 60x objective. The excitation source was a Thorlabs M530L2 collimated LED powered by a DC2100 LED driver. The light was filtered with a Cy3 emission/excitation filter cube. The camera used was an Andor Clara capturing images from a binned 512x512 pixel area at a frequency of 6.57 Hz. The nanopipette was lowered with a screw micromanipulator into a well formed by PDMS on a glass cover slip positioned above the objective. Emulsion preparation for optical imaging followed the same procedure as previously described except that 1 mM Nile Red (Aldrich) in toluene was used instead of pure toluene as the basis of the 400 mM IL-PA in toluene mixture.

5.3 Results and Discussion

5.3.1 Laser-Pulled Nanopipette Fabrication

Nanopores were tested prior to use to measure their size and suitability for emulsion studies. In all cases nanopores gave a nearly linear, Ohmic *i*-V response. The conductivity of the

pore was determined from the slope of the *i*-V response and the nanopore size was estimated using the following equation,[25]

$$R_p = \frac{1}{\kappa a}\left(\frac{1}{\pi \tan(\theta)} + \frac{1}{4}\right)$$

where R_p is the resistance of the pore, κ is the conductivity of the solution, a is the pore radius at the orifice, and θ is the half-cone angle of the pore. For our pores the conductivity κ was approximated as being equal to the conductivity of a 5 mM potassium chloride solution, or approximately 0.07 S•m.[26] We feel this approximation is appropriate given that TBACl and KCl share the same anion and that the cations have the same magnitude of charge. The actual conductivity is likely lower because the diameter of TBA^+ is nearly three times larger than K^+,[27] reducing its mobility in solution. The half-cone angle was approximated as 8.5° and the resistance was found from the slope of a linear regression of the *i*-V curve.[25]

5.3.2 Emulsion Droplet Detection

Applying a negative potential inside the nanopipette relative to the outside resulted in large current blockades in which >85% of the ionic current is blocked. These large blockades are separated by tens of seconds. After each blockade the ionic current returns to its baseline current as determined by a previously acquired i-V curve. Each of these blockades are preceded by smaller blockade steps of a few pA each. The readers are encouraged to view the videos in the supporting information showing optical images of the process with a simultaneous readout of voltage, ionic current, and fluorescent intensity. We hypothesize this electrical response is the result of individual oil droplets interacting with the nanopore through collisions and translocations as shown in **Figure 5.1a**. We further investigated the steps and blockades with differently sized nanopores.

To understand the droplet-nanopore interactions it is necessary to understand the forces governing the droplets' movement within solution far from and near the nanopore orifice. Outside

of the nanopore, the electric field approaches zero and oil droplets move under the influence of Brownian motion. Near the nanopore, the electric field is concentrated and electrophoresis and electroosmosis act on the droplet. Electrophoresis is the force directly acting on the oil droplet due to its surface charge and zeta potential. The zeta potential of these droplets has been measured previously as being -15.8 mV in a salt-less solution.[22] This is quite weak for a emulsion,[28] and is weakened further by the addition of 5 mM TBACl in our experiments. The charged droplets move under the influence of the electric field in the nanopore, and under the polarity we apply, negative inside relative to outside, the droplets would be repelled. The electroosmotic flow, on the other hand, is due to the movement of positive ions along the inner wall of the nanopore. The movement of these ions is induced by the electric field concentrated in the nanopore and the positively charged ions move into the nanopore under our applied voltage. The ions bring solution with them, creating a flow in the direction of ionic movement. Given that these electrical signals occur only at negative potentials where the electrophoretic force is repelling the negatively charged oil droplets from the nanopore, we conclude that the dominant force involved with the translocation of the droplets is electroosmosis.

We will first discuss the large current blockades and we begin with a current-time trace of this phenomenon shown in **Figure 5.1b** where the large blockades shown at 40 s, 75 s, and 120 s reach a nearly 95% blockade of the current. We suggest these large blockades are an agglomerated oil droplet squeezing through the pore orifice. The nanopore's orifice, also called the sensing zone, is where the concentrated electric field reaches a maximum. This orifice is where the ionic current is limited, thus events occurring in this zone modulate the electric current measured at the Ag/AgCl electrodes. The aqueous volume containing ions is displaced when the agglomerated oil droplet moves through the pore, causing the conductivity of the pore to drop because of the reduced

amount of charge carriers. The size of the particle relative to the nanopore and its elastic nature results in a reversible >95% blockade of the nanopore's ionic current for which we have been unable to find precedent in literature. Previous studies, notably by the White group, have demonstrated trapping and translocation of soft particles. However, these never resulted in more than a 67% blockade of the ionic current.[15]

There remains some ionic current passing through the pore during the agglomerated oil droplet translocation. We present some arguments as to why one of these agglomerated droplets is unable to fully block the ionic current passing through the nanopore sensing zone given its elasticity and size. There is a voltage dependence on the ionic current blockades of these large translocations as shown in **Figure 5.2a**. At -200 mV there is a nearly 99% reduction in ionic current and at -400 mV there is a drop in the blockade current down to 87%. We suggest that this is due to ion transport in a remaining aqueous volume near the negatively charged hydrophilic quartz walls. Additionally, it has been hypothesized that the concentrated electric field of a nanopore can cause charged, elastic particles to deform[19] and elongate along the axis of the pore, increasing the aqueous volume along the nanopore walls. Another contribution comes from the transport of tetrabutylammonium ions (TBA^+) through the water-toluene-water interface. After a threshold voltage is passed, the movement of TBA^+ through the toluene phase is enabled in the concentrated electric field of the nanopore. Both of these contributions occur more strongly at larger applied voltages, and agree with our experimental findings.

The increased electric field is evident in the translocation time of the agglomerated oil droplets as shown in **Figure 5.2b**. The relationship between nanoparticle translocation time and applied potential in nanopores has been investigated previously.[29,30] Given these previous reports it is not surprising that our results follow the same relationship.

5.3.3 Emulsion Agglomeration Dynamics

The other part of the phenomenon as discovered in the current-time traces are the few-pA current steps leading to the larger blockade. We attribute these steps to the collision and agglomeration of individual oil droplets into a larger droplet at the sensing zone of the nanopore. Each addition of a droplet to the agglomerated droplet results in an increase in the size of the agglomerated droplet which decreases the amount of ionic current able to flow through the nanopore. We suggest these droplet additions are observed as the step-wise reduction of ionic current in a current-time trace. If the steps are assumed to be the collision and agglomeration of individual droplets into a larger droplet at the pore orifice then one can apply resistive-pulse analysis. In **Figure 5.3a** the average step height, in percent of open-pore ionic current, is plotted as a function of applied voltage. There is a key trend to observe in the data, that is the percent blockade follows as a function of pore size. In typical resistive pulse measurements of solid nanoparticles, the fraction of volume excluded by the pore remains constant regardless of voltage and as such the fraction of ionic current blocked remains constant.[31] We can predict the ionic current blockade using simulation results previously published regarding resistive pulses in conical nanopores. For 160-nm-diameter particles and a 300-nm-diameter nanopore one should expect a resistive pulse to blockade 3% of the ionic current,[32] which is not near the 1% blockades observed in our experiments. In the case of the emulsion droplets an inverse relationship between step height and applied potential is observed. This trend is similar to the one observed with the larger blockades and we offer the same hypothesis. The increased electric field deforms the particle and increases leakage current in the aqueous phase around the droplet, and when a threshold potential is crossed the TBA^+ ions can cross the water-toluene-water interface, increasing ionic current.

To fully block a 300-nm-diameter nanopore one would reason that a 300-nm-diameter particle or larger is required. A simple calculation reveals that 10 160-nm-diameter droplets is

required to agglomerate to form a 300-nm-diameter droplet, a number slightly lower than that of our experiments. Determining the absolute number of steps for each trace is challenging as there are steps below our detection threshold, spikes, negative steps, and hard-to-measure steps on the biphasic pulse following translocation of the agglomerated droplet. Additionally, the elastic nature of the particle allows the particle to be deformed easily, requiring a larger particle to significantly block the pore. This effect was noticed during fluorescence imaging mentioned later, where the addition of a droplet sometimes changed the position of the agglomerated oil droplet in the nanopore.

Analysis of the step frequency, or collision frequency, is plotted in **Figure 5.3b** and shows a proportional relationship with increasing voltage for each pore studied. This follows other reports in which an increased pressure differential across the nanopore increased the detection frequency.[29] In the case of our pores this pressure is replaced with an electroosmotic flow, the magnitude of which increases with voltage. It follows that this flow should increase the flux of droplets to the nanopore above that expected through a purely diffusional process. The diffusion coefficient of an 80-nm-radius droplet can be estimated from the Stokes-Einstein equation.[33]

$$D_d = \frac{k_b T}{6\pi\eta r_d}$$

Where k_b is the Boltzmann constant, T is the temperature, η is the viscosity of water at 298 K, and r_d is the radius of an individual droplet. From this equation, the calculated diffusion coefficient of an 80-nm-radius droplet is 3.1×10^{-8} cm^2 s^{-1}. We can then estimate the diffusional flux of droplets to the nanopore through the following equation,[33]

$$f_d = 4 D_d C_d r_e$$

in which C_d is the concentration of the droplets and r_e is the radius of the nanopore. For our particle concentration of 1.2×10^{12} particles/mL and a 150-nm-radius nanopore we calculate a collision

frequency of 0.21 Hz. This is below all measured collision frequencies in the presence of electroosmosis in our experiment.

Collecting step data was only possible within a pore-dependent range of potentials. This range was limited on the high end by the gradual transformation of steps into spikes as shown in **Figure 5.4**. The force on agglomerated droplets increases with potential and agglomerated droplets are pulled through before a large agglomeration can form as happens at lower voltages.

5.3.4 Emulsion Droplet Trapping

At pore-dependent potentials of -300 mV and lower a new phenomenon was discovered: droplet trapping. In this potential regime, the forces acting on agglomerated droplets were strong enough to attract droplets to the pore but not strong enough to pull the large agglomerated droplet through the orifice. In this case there are large >95% ionic current blockades that last until perturbed by changing the potential. **Figure 5.5** shows a typical trace for one of these droplet trapping events. This process bears similarity to phospholipid bilayer experiments where the formation of a bilayer is heralded by the sudden decrease of ionic current as a gigaohm electrical seal is formed around the bilayer.[34] The seal around the droplet is similarly strong, around 10 GΩ. In this trapped state, we hypothesize that the electroosmotic pulling force is clamped-off, reducing the individual droplet collision frequency close to its diffusion-only value of 0.21 Hz as calculated earlier. This is important for future electrochemical studies in which the size-stability of the trapped droplet over time will affect results.

5.3.5 Fluorescence Imaging

To verify our hypothesis, we imaged the collisions and translocations with a fluorescent microscope setup. A lipophilic dye, Nile Red, was chosen as it partitioned heavily into the toluene phase while having minimal background fluorescence in the aqueous phase. Applied voltage, ionic

current, and fluorescence intensity were measured and recorded simultaneously. An example of simultaneously recorded ionic current and mean fluorescence intensity at the nanopore is shown in **Figure 5.6**.

In the experiment, an initial oil droplet seed forms and is quickly grown through the collision of other individual droplets. The electroosmotic flow during this period is visibly strong as evidenced by the increased velocity of droplets within the entire field of view of the camera. This stage is seen in the few seconds at the beginning of droplet formation, or immediately after the translocation of a droplet that previously occupied the orifice.

As the droplet grows the ionic current drops and the apparent electroosmotic flow decreases as can be seen in the reduction of motion of oil droplets. At this point the droplets appear to exhibit Brownian motion except in the very near vicinity of the nanopore orifice. If a droplet diffuses too closely to the pore it is pulled into the pore and will either join the already-formed agglomeration or be accelerated past the pore back into solution where it returns to Brownian motion.

As the agglomerated droplet at the pore orifice grows it can suddenly be nudged into the trapped state through the collision of a droplet in solution. This is seen in the videos provided in the SI through the correlation of a >90% ionic current blockade with a sudden increase in fluorescence, along with the apparent collision of a droplet with the agglomeration at the nanopore orifice.

As with the purely electrical measurements, the agglomeration can remain in the trapped state for minutes at a time, or until perturbed. The introduction of a perturbation force through an increase in electric potential of a few hundred millivolts causes a slow pulling force to be applied to the agglomerated droplet in the nanopore. This droplet movement is accompanied by a gradual weakening of the electrical seal at the pore and an increase in ionic current. The droplet is then

suddenly released from its trapped state causing a rush of droplet solution to be drawn into the pore, causing a quick initial growth of a new agglomeration and beginning the process anew. The sudden movement of the droplet is occurs simultaneously with the decrease of mean fluorescence at the nanopore orifice and an increase in ionic current. This event happens on the order of milliseconds, or possibly faster, given that our ionic current measurements cannot capture the event while sampling at 50 kS/s with a 10 kHz low-pass filter. An example ionic current trace with accompanying fluorescence images during an agglomerated droplet translocation event is shown in **Figure 5.7**.

Additional insight gained from the video is a remarkable agreement between video and step collision analysis. As mentioned in the previous section, we used the current step analysis to calculate the actual droplet collision frequency at the nanopore orifice to be higher than that seen through a purely diffusional process. Fluorescent imaging makes it apparent that this is true, in that the electroosmotic flow into the pore gets attenuated as the agglomeration in the orifice grows larger over the course of an experiment. The rapid flux of droplets to the orifice immediately after a translocation demonstrates that the electroosmotic flow at this point is very strong. As the agglomeration grows the force pulling droplets into the pore weakens and only an area near the orifice attracts droplets, although this still creates a collision frequency above that expected through diffusion.

Imaging data also helps to explain how ionic current blockade varies with applied potential as reported in previous sections. It is seen that application of a voltage causes the droplet to move within the orifice of the nanopore quickly, on the order of milliseconds, in response to the resulting electroosmotic flow. The magnitude of the potential controls the magnitude of the force, and in imaging it was observed that a larger potential caused the agglomerated droplet in the nanopore to

sit ‘further up’ into the nanopore, where it did not form as strong of a seal on the sensing zone of the nanopore.

5.3.6 Trapped Droplet Voltammetry

The absence of pressure in our experiments means the primary forces acting on the trapped droplet are electroosmosis and electrophoresis. Both forces are dependent on the electric field strength which is a function of the applied potential. By scanning the potential quickly (20 V/s) one can obtain a voltammogram of the trapped droplet without perturbing the droplet through changing electric fields.

Consecutive 20 V/s cyclic voltammetry (CV) was performed on a droplet trapped with a -100 mV holding potential. In each case, the post-CV current returns to its pre-CV value which informs us that the gigaohm seal was not affected by the scan. **Figure 5.8** shows the acquired voltammogram with the associated TBA^+ movement shown above each peak for the forward and backward scans. Put simply, these peaks result from TBA^+ ion transfer through three different barriers during the scan. During the initial emulsification step TBA^+ partitions into the toluene phase passively. The pair of central peaks at 0.10 V and -0.13 V result from passively partitioned TBA^+ leaving the toluene phase T and entering the bulk aqueous phase B during the forward scan or the pipette aqueous phase P during the backward scan. The low potential for this transfer when compared with the outer peaks is due to TBA^+ being better solvated in the aqueous phase than the organic phase. The outer peaks result from the movement of TBA^+ through either aqueous to toluene barrier, depending on the polarity of the voltage applied.[35] We use this technique to demonstrate the quality of the resistive seal formed around the droplet and the capability of performing repeated electrochemical measurements of the single attoliter volume.

5.4 Conclusions

We use conical nanopores in conjunction with the resistive pulse technique to monitor the agglomeration of individual oil droplets in an aqueous solution. The oil droplets collide and agglomerate at the nanopore's sensing zone, allowing electrical recordings with μs time resolution and pA current resolution to be made of the process. We observe the translocation of this agglomerated droplet at potentials larger than -300 mV and trapping of the droplet at lesser potentials. The trapped droplet representing an attoliter volume can be individually and repeatedly electrochemically addressed. The entire phenomenon is captured optically using fluorescent microscopy with a lipophilic dye to confirm the hypothesis. We expect this method to be useful for single molecule optical and electrical studies within small attoliter volumes.

5.5 Schemes and Figures

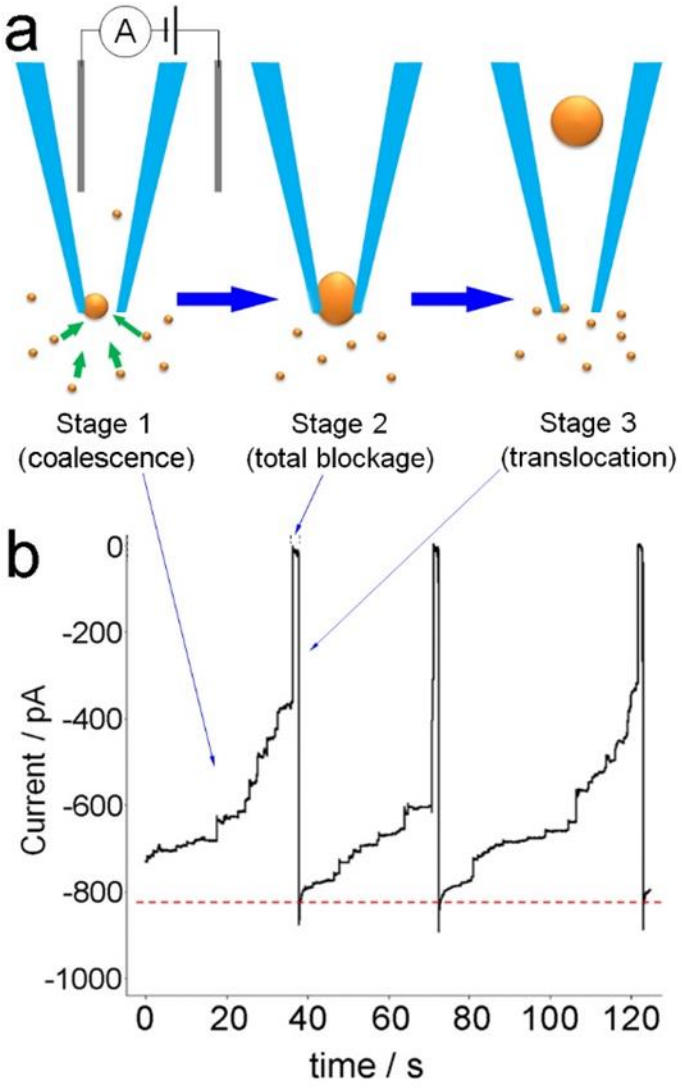

Figure 5.1. Overview of emulsion phenomenon.

(a) A cartoon showing electroosmosis-driven collision and agglomeration of individual emulsion droplets at the orifice of a pipette pore. A small voltage (<1 V) is applied across the pipette pore to drive the flow of emulsion droplets toward the pore and the ionic current is monitored as a function of time. (b) Three translocation events of large agglomerated droplets through a pipette pore at -300 mV. Each event starts from multiple smaller stepwise current decreases followed by a quick and large current decay and a current increase back to the original baseline current. The

small current steps (few-pA) indicate collision and agglomeration of small droplets onto a larger droplet trapped at the pore orifice. The large current decay is due to growth of the trapped droplet exceeding a certain size limit causing a full blockage of the pipette pore. The large current increase indicates translocation of the trapped large droplet through the pore. The red dashed line indicates the ionic current baseline as determined from a CV prior to droplet studies.

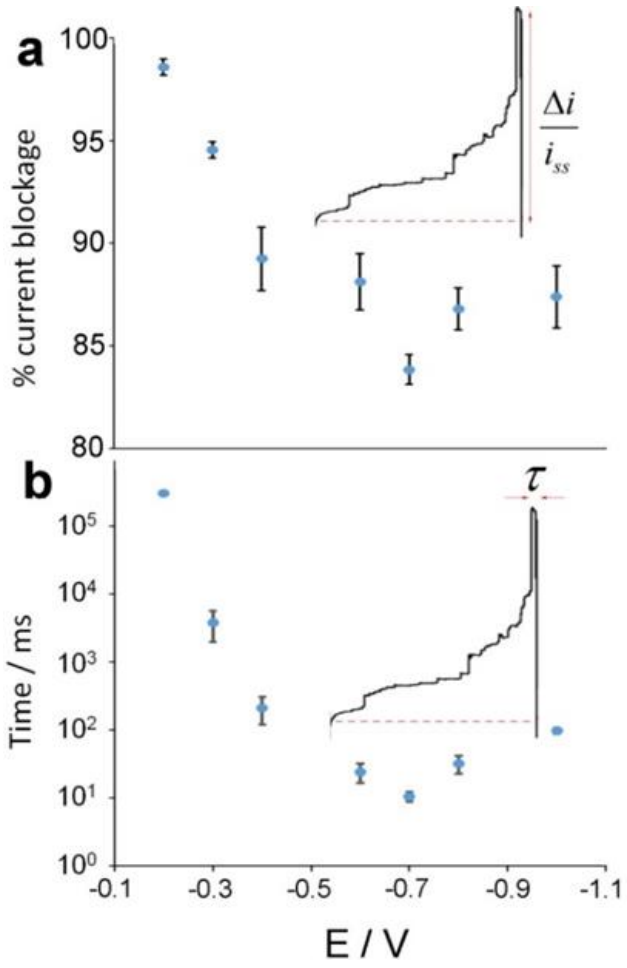

Figure 5.2. Agglomerated droplet translocation dynamics.

(a) A plot of the % current blockage caused by an agglomerated droplet as a function of the applied potential. (b) A plot of the residence time of an agglomerated droplet as a function of the applied potential. Error bars are standard error.

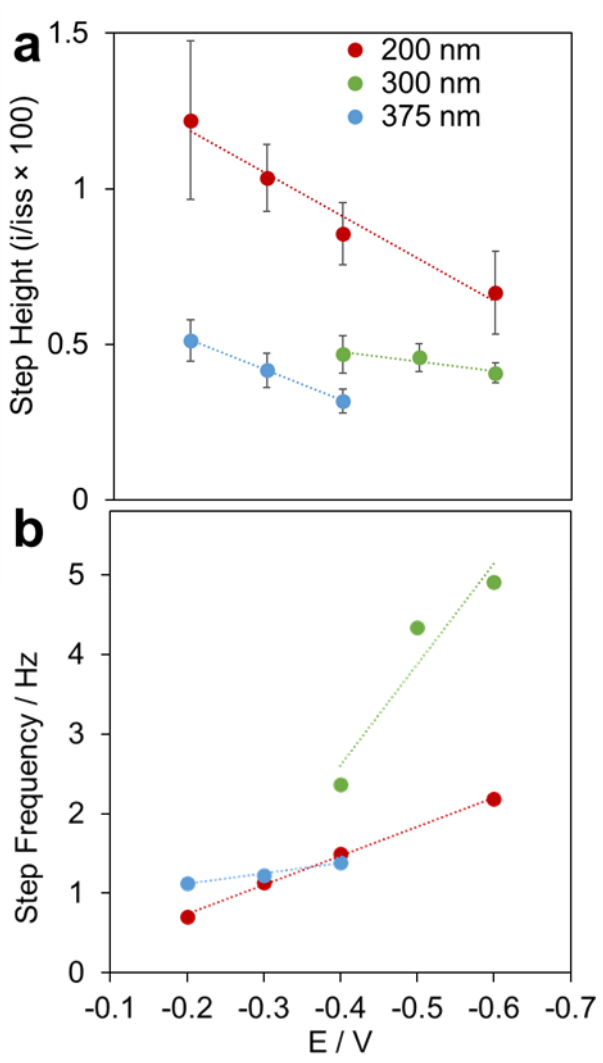

Figure 5.3. Individual oil droplet collision dynamics.

The average % current reduction due to the addition of a single oil droplet plotted as a function of the applied potential for three different nanopores with diameters listed in the legend. The steps follow a trend of being higher for smaller pores as seen in the -0.4 V points. The steps become smaller with increased potential which is attributed to a larger ionic leakage current around and through the agglomerated droplet. Error bars are standard error. (b) The frequency of current steps as a function of applied potential. Unlike step height there is no obvious trend among pore sizes. However, steps become more frequent with applied potential among all pores studied. This can be

understood as an increase in the distance and magnitude of the electroosmotic pulling force as the potential becomes more negative.

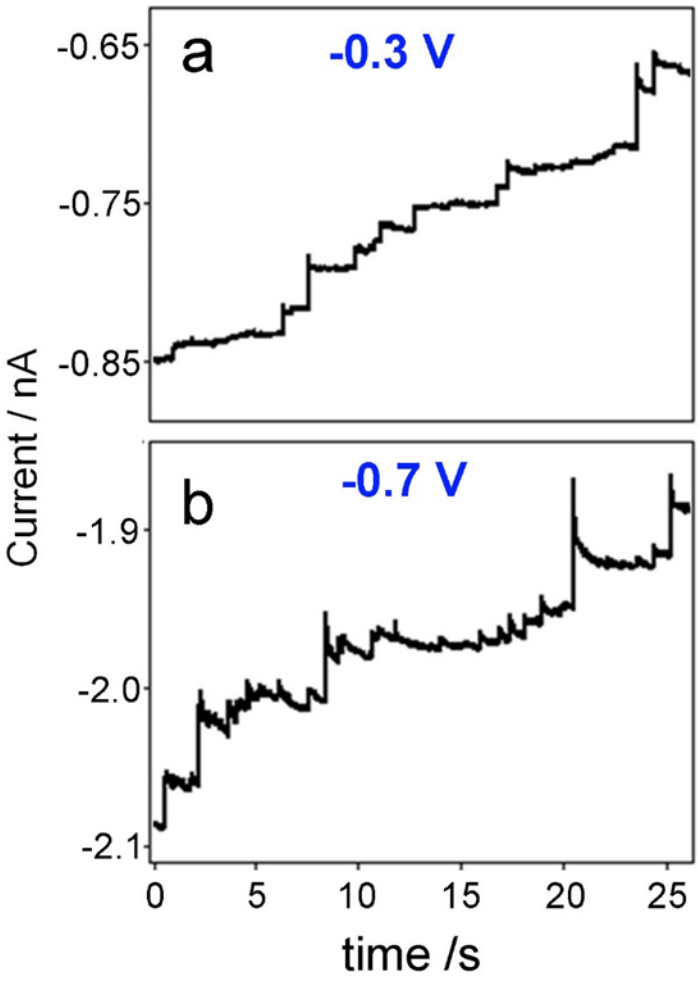

Figure 5.4. Transformation of oil droplet collision electrical signature from steps to peaks. A comparison of step-like current changes observed at -0.3 V (a) and peak-shape current changes at -0.7 V (b). Single emulsion agglomerations change from step-shape response to peak-shape responses as the applied voltage was increased.

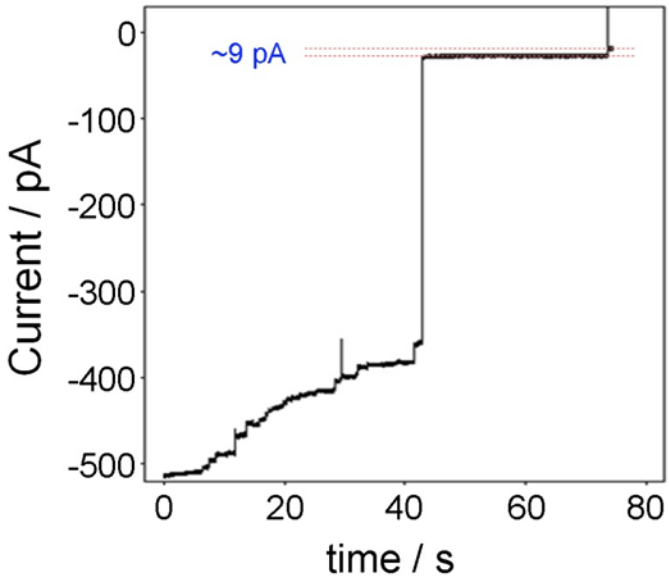

Figure 5.5. Droplet trapping.

A nanopore at -0.2 V featuring the step-wise decrease of ionic current before experiencing an indefinite 98.6% ionic current blockade. Typically, the droplets are stable enough in this trapped configuration to run CVs at high scan rates (~20 V/s). At the 75 s mark, the potential is switched from -0.2 V to 0 V giving a large charging spike. This was done to demonstrate the magnitude of the blocked ionic current. In this case there was a 9 pA difference between the trapped state at -0.2 V and the off state at 0 V. With a 600 pA baseline at -0.2 V, as determined by the prior *i*-V curve, this amounts to a 98.6% ionic current blockade, or a 20 gigaohm seal. The trapped droplet can be dislodged by increasing the magnitude of the negative potential or by switching to a positive potential to eject the droplet.

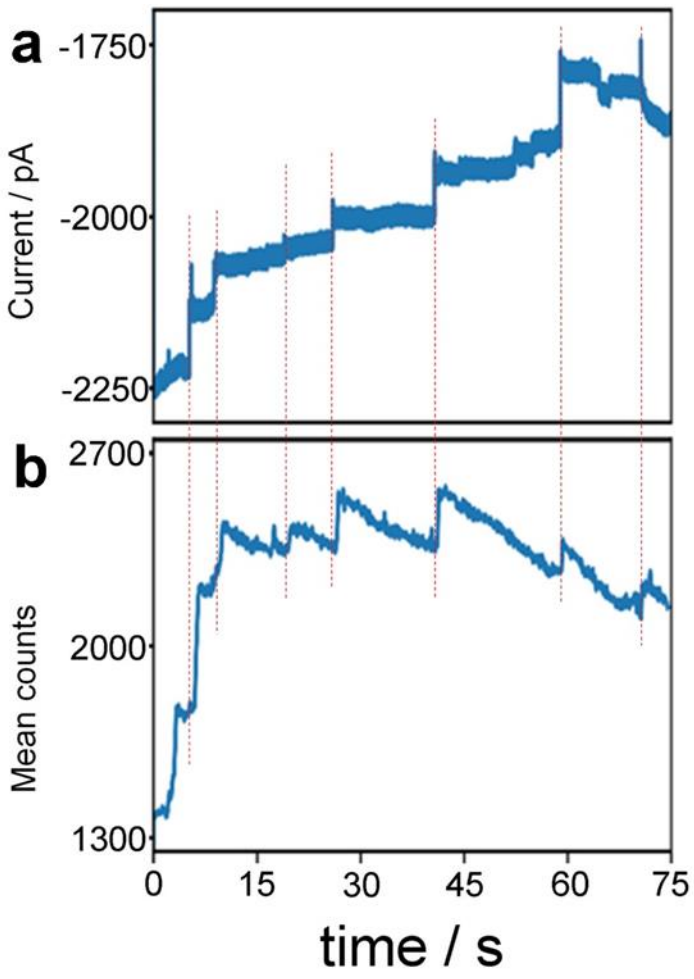

Figure 5.6. Simultaneous electrical and optical recording.

(a) Ionic current versus time for a nanopore during oil droplet collisions. (b) The corresponding fluorescence trace recorded simultaneously. Counts were measured as the mean fluorescence of a square region of pixels at the nanopore orifice.

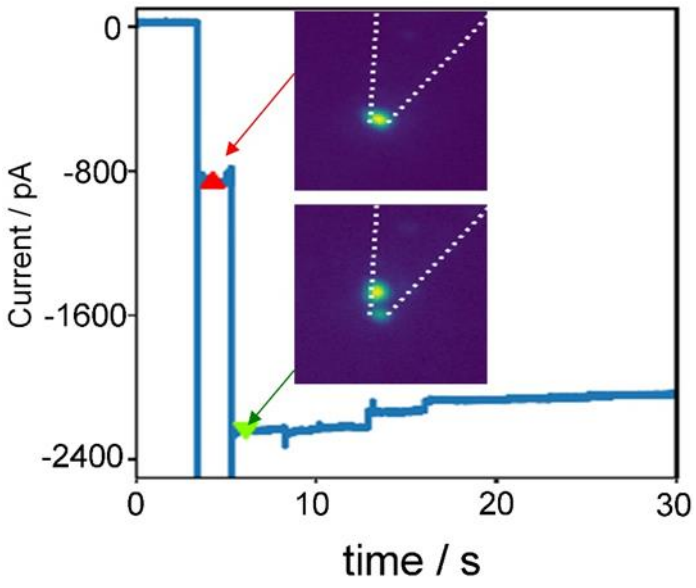

Figure 5.7. Fluorescence imaging of agglomerated droplet translocation.

Fluorescence images corresponding to points on the ionic current-time trace before (red triangle) and after (green triangle) the translocation of an agglomerated oil droplet through the nanopore. The white dashed lines in the images denote the edges of the nanopipette. The bright dot in the before image is the agglomerated oil droplet with fluorescently excited Nile Red. In the after image, the agglomerated droplet has moved further up into the nanopipette but is still adsorbed to the wall. At this stage, because of residue from the previous agglomeration or the immediate collision of new individual droplets, a new agglomerated droplet is forming in the nanopore orifice.

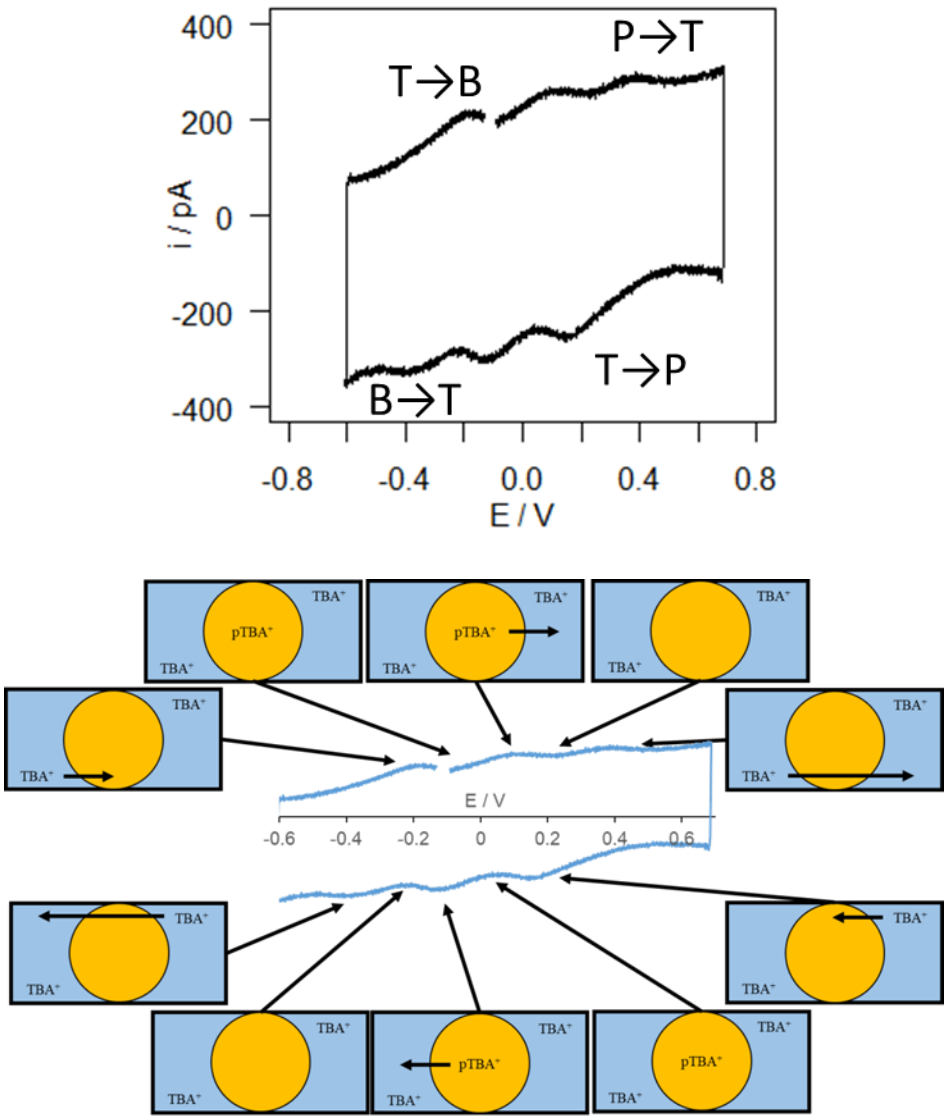

Figure 5.8. Trapped droplet voltammetry.

Illustration of phases present during CVs of trapped emulsion droplets with the aqueous nanopipette phase P, the toluene droplet phase T, and the outer beaker solution B. A CV of a trapped droplet at 20 V/s with proposed movement of TBA^+ ions. Potential listed is the voltage applied to the inside of the nanopipette relative to the outside.

5.6 References

(1) Shi, W.; Friedman, A. K.; Baker, L. A. *Anal. Chem.* **2017**, *89*, 157−188.

(2) Li, G.; Zhang, Z.; Lin, X. *Chin. J. Anal. Chem*. **2010**, *38*, 1698−1702.

(3) Heins, E. A.; Siwy, Z. S.; Baker, L. A.; Martin, C. R. *Nano Lett*. **2005**, *5*, 1824−1829.

(4) Harms, Z. D.; Mogensen, K. B.; Nunes, P. S.; Zhou, K.; Hildenbrand, B. W.; Mitra, I.; Tan, Z.; Zlotnick, A.; Kutter, J. P.; Jacobson, S. C. *Anal. Chem*. **2011**, *83*, 9573−9578.

(5) Zhou, K.; Li, L.; Tan, Z.; Zlotnick, A.; Jacobson, S. C. *J. Am. Chem. Soc*. **2011**, *133*, 1618−1621.

(6) Manrao, E. A.; Derrington, I. M.; Laszlo, A. H.; Langford, K. W.; Hopper, M. K.; Gillgren, N.; Pavlenok, M.; Niederweis, M.; Gundlach, J. H. *Nat. Biotechnol*. **2012**, *30*, 349−354.

(7) Li, W.; Gong, L.; Bayley, H. *Agnew. Chem. Int. Ed*. **2013**, *52*, 4350−4355.

(8) Perera, R. T.; Fleming, A. M.; Johnson, R. P.; Burrows, C. J.; White, H. S. *Nanotechnology* **2015**, *26*, 074002.

(9) An, N.; Fleming, A. M.; White, H. S.; Burrows, C. J. *ACS Nano* **2015**, *9*, 4296−4307.

(10) Ayub, M.; Bayley, H. *Nano Lett*. **2012**, *12*, 5637−5643.

(11) Berge, L. I.; Feder, J.; Jøssang, T. *Rev. Sci. Instrum*. **1989**, *60*, 2756−2763.

(12) Ito, T.; Sun, L.; Crooks R. M. *Anal. Chem.* **2003**, *75*, 2399−2406.

(13) Coulter, W. H. *Means for Counting Particles Suspended in a Fluid* **1953**, US Patent No. 2656508.

(14) Pevarnik, M.; Healy, K.; Toimil-Molares, M. E.; Morrison, A.; Létant, S. E.; Siwy, Z. S. *ACS Nano* **2012**, *6*, 7295−7302.

(15) Holden, D. A.; Watkins, J. J.; White, H. S. *Langmuir* **2012**, *28*, 7572-7577.

(16) Chen, L.; He, H.; Jin, Y. *Anal. Chem.* **2015**, *87*, 522-529.

(17) Holden, D. A.; Hendrickson, G. R.; Lan, W-J.; Lyon, L. A.; White, H. S. *Soft Matter* **2011**, *7*, 8035-8040.

(18) Somerville, J. A.; Willmott, G. R.; Eldridge, J.; Griffiths, M.; McGrath, K. M. *J. Colloid Interface Sci.* **2013**, *394*, 243-251.

(19) Darvish, A.; Goyal, G.; Aneja, R.; Sundaram, R. V. K.; Lee, K.; Ahn, C. W.; Kim, K-B.; Vlahovska, P. M.; Kim, M. J. *Nanoscale* **2016**, *8*, 14420-14431.

(20) Goyal, G.; Darvish, A.; Kim, M. J. *Analyst* **2015**, *140*, 4865-4873.

(21) Holden, D. A.; Hendrickson, G.; Lyon, L. A.; White, H. S. *J. Phys. Chem. C* **2011**, *115*, 2999-3004.

(22) Kim, B.-K.; Boika, A.; Kim, J.; Dick, J. E.; Bard, A. J. *J. Am. Chem. Soc.* **2014**, *136*, 4849−4852.

(23) Edwards, M. A.; German, S. R.; Dick, J. E.; Bard, A. J.; White, H. S. *ACS Nano* **2015**, *9*, 12274-12282.

(24) Killick, R.; Eckley, I. A. *J. Stat. Soft.* **2014**, *58*, 1-19.

(25) Zhang, B.; Galusha, J.; Shiozawa, P. G.; Wang, G.; Bergren, A. J.; Jones, R. M.; White, R. J.; Ervin, E. N.; Cauley, C. C.; White, H. S. *Anal. Chem.* **2007**, *79*, 4778-4787.

(26) Wu, Y. C.; Koch, W. F.; Pratt, K. W. *J. Res. Natl. Inst. Stand. Technol.* **1991**, *96*, 191-201.

(27) Masterton, W. L.; Bolocofsky, D.; Lee, T. P. *J. Phys. Chem.* **1971**, *18*, 2809-2815.

(28) Everett, D. H. *Basic Principles of Colloid Science*; The Royal Society of Chemistry: London, 1988.

(29) German, S. R.; Luo, L.; White, H. S.; Mega, T. L. *J. Phys. Chem. C* **2013**, *117*, 703-711.

(30) Davenport, M.; Healy, K.; Pevarnik, M.; Teslich, N.; Cabrini, S.; Morrison, A. P.; Siwy, Z. S.; Létant, S. E. *ACS Nano* **2012**, *9*, 8366-8380.

(31) Luo, L.; German, S. R.; Lan, W.-J.; Holden, D. A.; Mega, T. L.; White, H. S. *Annu. Rev. Anal. Chem.* **2014**, *7*, 513-535.

(32) Lan, W.-J.; Holden, D. A.; Zhang, B.; White, H. S. *Anal. Chem.* **2011**, *83*, 3840-3847.

(33) Kim, B.-K.; Boika, A.; Kim, J.; Dick, J. E.; Bard, A. J. *J. Am. Chem. Soc.* **2014**, *136*, 4849-4852.

(34) Jonas, E. A.; Knox, R. J.; Kaczmarek, L. K. *Neuron* **1997**, *19*, 7-13.

(35) Velický, M.; Tam, K. Y.; Dryfe, R. A. W. *Anal. Chem.* **2013**, *86*, 435-442.

Chapter 6. Sealed Laser-Pulled Nanopipettes as a Unique Platform for Microfabricated Quartz Nanopores

6.1 Introduction

A nanopore is a nanometer-scale aperture formed inside either an ultrathin solid-state membrane, referred to as an artificial nanopore, or a biological protein molecule such as an ion-channel protein. Nanopore-based sensors have attracted enormous interests in analytical chemistry due to their exceedingly high sensitivity.[1] For example, depending on the sizes of the nanopore and the analyte species, one can use a nanopore sensor to detect various species ranging from single-stranded DNA,[2-5] RNA,[6] small molecules,[7,8] proteins,[9] viruses,[10,11] and larger nanoparticles.[12,13]

Nanopore sensors normally operate on a resistive-pulse mechanism, also known as the Coulter counter method.[14] In resistive-pulse measurements, one normally holds a constant voltage across the nanopore membrane while measuring the ionic current passing through the pore over time. A transient change in the ionic current is anticipated when an analyte particle translocates through the nanopore providing critical information about the analyte particle, such as shape, electrophoretic mobility, charge, and size. A slight decrease in the current is often observed due to a particle partially blocking the flow of the ions. The detection frequency can be used to analyze particle concentration. Based on the shape and duration of the current pulse, one can also obtain information about the pore geometry.[15]

Protein pores can give reproducible pore size and somewhat tunable chemistry of the inner pore walls. However, the analytical use of these pores is often limited by the short lifetime of the lipid membrane the pores are inserted in and their narrow size range. Artificial nanopores, on the other hand, can be made in a variety of materials including glass,[16,17] silicon nitride,[18]

polycarbonate and polyethylene terephthalate (PET),[19] metals,[20] carbon nanotubes,[21] and single or few layer graphene.[22] Some of the popular nanopore fabrication methods include glass/quartz pipette pulling,[23] milling of a thin membrane using a focused beam of electrons[24] or ions,[25] electric breakdown,[26] and track etching of a polymer membrane.[27] Depending on the fabrication technique, one can make cylindrical or conical nanopores from as small as a few angstroms[28] to hundreds of nm enabling detection of analyte species of various sizes. The methods for nanopore fabrication in some of the above materials have been well reviewed.[1,29,30]

Pipette pulling is an easy and fast method to prepare size-tunable conical glass/quartz nanopores with benchtop equipment.[31,32] Pipette nanopores are low cost, disposable, and can be quickly filled with an electrolyte solution for leak-free electric measurements. Furthermore, they can be used as useful scanning probes for high-resolution imaging in liquids.[33] However, pipette pores are normally made with a long taper which not only lowers the sensitivity due to the added solution resistance, but also increases the possibility of pore clogging due to adsorption in a highly restricted volume near to tip. Focused ion-beam (FIB) or electron-beam milled silicon nitride membrane pores can have tunable size and shape. These pores can potentially have exceedingly high sensitivity due to ultrathin pore thickness and a highly-focused sensing zone. However, a key challenge is the high electric noise due to the large membrane size and the use of conductive silicon support.[34,35]

Here we describe a new nanopore fabrication method which combines the advantages of the handheld pipette pores, the superior electric property of quartz, and the versatility of FIB milling in one device. **Scheme 6.1** shows a comparison of particle translocation through a laser-pulled pipette pore and FIB-milled side pores. The pipette pore is located at the far end of the pipette tip and is characterized by a longer highly restricted zone. In the case of the side pores, two

nanopores are shown in the side walls of a sealed quartz pipette. A small voltage (<1 V) is applied between the inside and outside of the quartz nanopipette enabling electroosmosis-driven nanoparticle translocation. Besides its easy use, a unique aspect of a side pipette nanopore is the ability to change the pore thickness by selectively milling at different distances away from the sealed pipette tip. Nanopore thickness can be varied over a large range from below 50 nm to several microns on the same device. This allows one to focus the sensing zone to an ultrathin pore volume while largely avoiding the ionic resistance in the long pipette taper. These pores have tunable diameters, depths, and to an extent, cone angles, based on easily tunable milling parameters. We show that the pores have smooth, reverse-conical geometries and exhibit very low current rectification under the conditions used. We characterize the pores using scanning electron microscopy (SEM), cyclic voltammetry (CVs), and amperometry of nanoparticle translocations. We observe the translocations of a single population of polystyrene nanoparticles and then successfully discriminate between two differently sized populations of polystyrene beads. Finally we demonstrate the versatility of the system by comparing the dynamic forces acting on particle translocation through two parallel pores of different length in the same membrane. Our results indicate that this system could be used as a model to explore particle transport in single nanopores as well as multi-pore membranes.

6.2 Experimental Section

6.2.1 Chemicals and Materials

Potassium chloride (KCl) was from Fisher. Potassium phosphate monobasic and dibasic was from J. T. Baker. Triton X-100 was from Aldrich. Polystyrene nanoparticles with diameters of 57 nm and 112 nm were from Polysciences. Ag/AgCl quasi-reference electrodes (QRE) were prepared by immersing 0.5 mm diameter silver wire from Alfa-Aesar into Tough Guy brand ultra-

bleach until the wire turned a noticeable shade of purple-grey. Quartz capillaries with a filament were from Sutter (I. D. 0.7 mm, O. D. 1.0 mm).

6.2.2 Focused-Ion Beam Nanopore Fabrication

Quartz capillaries were pulled into nanopipettes with a Sutter P-2000 laser-based micropipette puller using the standard thin-walled quartz recipe (Heat 700, Filament 4, Velocity 60, Delay 150, Pull 175). The nanopipettes were then sealed at the tip by carefully heating the tip on a Narishige MF-83 microforge. Sealed pipettes were electrically tested in 100 mM KCl to ensure a fully sealed tip. The sealed pipettes were sputter coated with an amorphous carbon film (SPI Supplies) to provide a conductive surface for SEM imaging and FIB milling. Nanopores were milled in the coated pipette wall using a dual beam FEI XL830 FIB. Beam current and exposure time were varied according to the depth of the nanopore being drilled. After FIB milling, the carbon film was removed from the pipettes with O_2 plasma in a Diener Femto plasma cleaner for 10 minutes.

6.2.3 Electrochemical Measurements

The conductance of FIB-milled nanopores was initially tested in 100 mM KCl by scanning between -1 and +1 V (all potentials hereafter were applied from the inside to the outside of the pipette). As an example, **Figure S6.1** shows a typical current-voltage response of a 263 nm diameter quartz nanopore. The potential was controlled by an EG&G PAR Model 175 function generator and a Dagan Chem-Clamp potentiostat. The Dagan was interfaced to a PC through a National Instruments 6251 DAQ card and a National Instruments BNC-2120 breakup box. Following conductance measurements, the solution in the pipettes was replaced with a solution of 100 mM KCl, 10 mM phosphate, and 0.1% Triton X-100 that was buffered to pH 7.4. An Axopatch 200B (Molecular Devices) was used for all nanoparticle translocation recordings. The signal was

digitized using a Digidata 1440A (Molecular Devices) that was interfaced with the computer using USB. Two Ag/AgCl QRE were used as the driving electrodes. All solutions used were filtered through a 200 nm PTFE syringe filter prior to use.

The tip of the pipette was submerged in the 100 mM KCl, 10 mM phosphate, 0.1% Triton X-100 solution as a control to observe baseline current in the absence of nanoparticles. Following this the outer solution was exchanged with the same solution with 112 nm or 57 nm polystyrene particles added at a concentration of 5×10^{10} particles/mL. Translocation experiments were performed by initially applying a series of positive potentials versus the outer electrode as a control to rule out particle translocations at this polarity. The voltage was then switched to negative and measured at -100 mV, -200 mV, -300 mV, and -400 mV for at least two minutes. Pore clogging was noted as an increase in root mean square (RMS) noise and was accompanied with a decrease in conductivity. We attempted to revive pores by applying a +1.3 V pulse through the application of the Axopatch's zap function. In the event of an unclogging we observed a decrease in RMS noise and an increase in conductance to the original level along with the return of translocation events as shown in **Figure S6.2**. Typically the current was filtered at 10 kHz by a low-pass filter and digitally sampled at 100 kHz. For longer pores at low voltages where the translocation events were sufficiently long the current was filtered at 5 kHz to increase the signal-to-noise ratio.

6.2.4 Finite Element Simulations

Nanopore conductance simulations with and without the presence of an insulating nanoparticle in the sensing zone was performed using COMSOL Multiphysics 5.2a.

6.3 Results and Discussion

6.3.1 Focused Ion Beam Nanopore Fabrication

In this study we used thin-walled quartz capillaries with an I. D. of 0.7 mm and an O. D. of 1.0 mm. The use of thin-walled quartz gave the greatest range of pore lengths to choose from during the ion milling process. Quartz is an ideal choice for low noise nanoparticle studies because of its superior electrical property[36] and a lower surface charge density than borosilicate.[37] The lower charge density reduces the electroosmotic force therefore increasing nanoparticle translocation time, assuming electroosmosis is the dominant force acting on the particle. It also reduces electrostatic repulsion between the negatively charged quartz nanopore walls and the negatively charged polystyrene particles, although this interaction was already significantly diminished by the high salt concentration in these experiments.

The thickness of the quartz wall of the pulled pipette increases away from the tip. We use the FIB to mill a pore in the taper of the pulled capillary at a specific distance from the tip. We have previously demonstrated that the ratio between the I. D. and the O. D. of the quartz capillary is kept during the laser pulling process.[38,39] **Figure S6.3** shows that the measured ratio between the I. D. and the O. D. of the quartz pipette follows the initial ratio prior to laser pulling. By examining the diameter of the sealed pipette at the milled location one can calculate the pore length (or, pipette wall thickness) based on the dimension of the original glass capillary. To demonstrate this unique capacity, we have created several quartz nanopores in the same pipette as shown in **Figure 6.1**. As one can see, four nanopores were milled with nominal lengths from 500 nm to as long as 4 μm. SEM images show that these nanopores are circular in shape ranging from ~250 to 350 nm in diameter. For all pores used in this study, the inner pore diameter was controlled in the range of 150 to 250 nm and the outer pore diameter was between 250 to 350 nm.

One minor challenge in FIB milling is the possible creation of asymmetric nanopores due to slow drift and vibrations. As such, a relatively large beam current is beneficial to mill quickly (<30 s) and eliminate the impact of sample drift and vibration. This is especially important when milling nanopores with thicker pore walls. The outer pore diameter of an FIB-milled nanopore has been found to be always greater than its inner pore diameter and a conical nanopore geometry is assumed with half-cone angles of 2° to 10°. The application of xenon difluoride (XeF_2) during ion milling has been proven to reduce this angle although a perfect cylinder is still not achievable. In this study the application of XeF_2 creates a nearly-cylindrical pore with measured cone angles below 7^o.[40] Cone angles were calculated based on the inner and outer pore diameters and the pore length. The inner and outer diameters of the pore were measured by independently focusing on the inner and outer orifice of the milled pore with SEM after FIB milling. These geometric measurements are illustrated in **Figure S6.4**. Even with the most conservative SEM measurements half-cone angles were always less than 7^o with this angle decreasing sharply with pore length to one or two degrees in pores over a micrometer long.

In the case of "good" pores we observe smooth walls inside the pore as shown in **Figure S6.5**. Nanoparticle translocations were not observed in pores with rough sidewalls even though the apparent pore diameter as determined with SEM and resistance measurements was twice as large as the particle diameter. Our hypothesis is that milled material redeposits inside the pore, occluding particle translocation. Only through the introduction of particles can one determine if a pore is blocked or not. In some cases, we observe discrete current changes in the absence of particles during initial conductance measurements, lending support to our hypothesis that there is material occluding the pore from the milling step. The application of XeF_2 during milling greatly increased our success rate from below 50% to nearly 100%. This was especially helpful in milling

longer pores for which the XeF_2 not only reduced redeposition but also increased the milling rate reducing the drifting effect of the SEM/FIB stage.

6.3.2 Electric Noise

A critical aspect of nanopore recording is the signal to noise ratio (S/N). Chip-based solid-state nanopores fabricated in silicon-supported thin-films of silicon nitride (SiN_x) or silicon oxide (SiO_x) typically exhibit significantly higher noise than quartz nanopores.[34] There have been several efforts to reduce the noise of these silicon based nanopores including the use of an additional insulating layer between the silicon substrate and the nanopore membrane. Due the small chip size, the mounting of these solid-state pores for nanopore recording can also be quite challenging, with these pores being prone to leaks around the mounting setup. One focus of this research was to create a new nanopore platform which not only expanded the abilities of existing nanopores but retained the low noise and ease-of-use of conical nanopores in quartz.

We measured the noise of laser-pulled pipette nanopores (referred hereafter as end pores) and FIB-milled side nanopores with an ionic current of 0 nA and -8 nA, a current representative of our -100 mV recordings. End pores had RMS noise of 3.65 pA and 5.28 pA at 0 nA and -8 nA, respectively. At 0 nA and -8 nA, the 1.3 µm side pore had an RMS noise of 4.64 pA and 4.70 pA and the 2 µm long pore had 6.03 pA and 6.65 pA respectively. The increase in low-frequency noise is expected with longer pore length and comes from the larger availability of charge states within the nanopore.[41,42] For comparison, the RMS noise of silicon-based nanopores has been reported as being as high as 38 pA at 0 nA, and noise over 100 pA with an ionic current being passed through the pore.[34] All told we observed a negligible difference in noise between laser-pulled end pores and FIB-milled side pores and measurements of tens of picoamperes was easily performed with

all pores. This is particularly evident in our double pore experiment, in which current blockades of ~20 pA are measured on top of an ~8000 pA baseline.

6.3.3 Nanopore Conductance

The nanopore conductance was measured in 100 mM KCl. As shown in the representative *i*-V response in **Figure S6.1**, all side pores had linear *i*-V responses between -1 V and +1 V. The diameter was determined from the *i*-V curve using the equation for the ionic resistance of a cylindrical nanopore:[43]

$$R = \frac{4L + \pi D}{\pi \kappa D^2} \quad (1)$$

Where L is the length of the pore as determined from SEM, D is the pore's diameter, and κ is the conductivity of the electrolyte solution. Discrepancies between the measured SEM diameter and the electrically measured diameter arose for the shortest of our pores. We ascribe this to an increased resistance due to the taper of the pipette as it constricts toward its point, as discussed later.

6.3.4 Electroosmosis-Driven Nanoparticle Transport

The translocation of polystyrene nanoparticles through the nanopore manifests as resistive-pulses in a current-time trace. **Figure S6.2** displays a typical current-time response showing nanoparticle detection through a 263 nm FIB-milled side nanopore with a length of 1259 nm. At a pH of 7.4 and a salt concentration of 100 mM the 57 nm and 112 nm polystyrene nanoparticles have a slight negative zeta potential of -6 mV and -5 mV respectively as measured with dynamic light scattering.

In previous studies on the translocation of nanoparticles through nanopores there have been three controllable forces in play: pressure, electroosmosis, and electrophoresis.[44] In this study we

do not apply a differential pressure and instead rely on electroosmosis and electrophoresis. These forces depend on the electric field within the pore. Electroosmosis pulls the cations within the double layer of the pore sidewalls into the pore when a negative potential is applied within the pore relative to the outside. Electrophoresis pulls the negatively charged nanoparticles into the pore when a positive potential is applied relative to the outside. Electroosmosis and electrophoresis will always work against each other because both the side walls of the pore and the surface of the particles are negatively charged. The dominant force can be determined by observing the polarity of the potential under which particles translocate. Only in the case of a negative potential applied inside the pore relative to outside did we observe translocations. We thus concluded that the electroosmotic force was the dominant force when considering the translocation of nanoparticles.

Figure 6.2a displays the change in the translocation time with pore length. The half-width of translocation events changes exponentially with pore length. All pores had an inner diameter of 150-250 nm and an outer diameter of 250-350 nm with pore lengths ranging from 495 to 3688 nm. Half-widths were all measured at -100 mV. The dashed line is an exponential fit to the data. The exponential increase in translocation time with pore length is an interesting result and can be qualitatively understood from two factors. The first factor is the increased sensing zone length. This increase in length creates a larger distance which the particle must travel. If this were the only factor one would expect the translocation time to increase linearly with pore length. The second factor is the decreased electroosmotic force as pore length gets greater. The electroosmotic force weakens because the same potential is now falling across a larger distance, lowering the magnitude of the electric field within the pore assuming the same potential is applied.

Figure 6.2b gives a direct comparison of the translocation current blockades of the 495 nm and 1259 nm long nanopores. The pore diameters are 210 nm for the 495 nm long pore and 265

nm for the 1259 nm pore. Here, we observe an unexpected higher current blockade in the 1259 nm long nanopore. This was originally puzzling because it has been suggested that the magnitude of the current blockade is related to the volume ratio of nanoparticle itself and the nanopore. For a cylindrical nanopore,[21]

$$\frac{\Delta i_c}{i_c} = S(d_s, d_c)\frac{d_s^3}{l_c' d_c^2} \qquad (2)$$

where i_c is the baseline current, Δi_c is the amplitude of the current pulse, d_s is the diameter of the particle, d_c is the diameter of the nanopore, and l_c' is the "end effect" corrected length given by: $l_c' = l_c + 0.785 d_c$. The correction factor $S(d_s, d_c)$ is dependent on the ratio of d_s to d_c,

$$S(d_s, d_c) = \frac{1}{1 - 0.8\left(\frac{d_s}{d_c}\right)^3} \qquad (3)$$

However it has been suggested that this is not the sole contributor to the current blockade and observations of this nature have also been reported by others using nanopores manufactured with FIB.[43] We hypothesize that in our system the overall current ratio $\Delta i_c/i_c$ is controlled by both the volume of the nanopore and the additional volume of the pipette's taper as the position of the nanopore is moved toward the tip. The 495 nm long pore is only ~20 μm from the tip while the 1259 nm long pore is ~50 μm from the tip. The constriction of the pipette between these pores adds additional resistance to the 495 nm long pore which is evident in its lower ionic conductance and the lower current blockades of translocating nanoparticles of the same diameter. Later we perform experiments and simulations to affirm this hypothesis in a double-pore setup.

To demonstrate the ability of our pores to analyze nanoparticles of different sizes, which is an important characteristic of any Coulter counter, we detected two different populations of

polystyrene beads. **Figure 6.3a** shows a current trace of nanoparticle detection in a buffer solution containing both 57 nm and 112 nm polystyrene nanoparticles using a 495 nm long nanopore at -400 mV. The diameter of the nanopore is 210 nm as determined by SEM. **Figure 6.3b** is a histogram of detected current blockades containing the two populations of nanoparticles. The larger 112 nm particles gave a larger current blockade of ~500 pA while the smaller 57 nm particles gave a ~70 nA blockade using the same pore. The predicted current ratio of the two nanoparticle populations based on equation 2 is 0.13 ($57^3/112^3$) which is in good agreement with the measured current ratio (70/500 = 0.14). **Figure S6.6** shows traces of nanoparticle translocations of each individual population as well as the voltage dependence on the percent current blockade. This result indicates that such FIB-milled glass nanopores are an excellent platform for sizing nanoparticles using the Coulter counter mechanism.

6.3.5 Double Pore Translocations

It has previously been demonstrated that multiple protein nanopores can be used in the same membrane to detect single molecules.[45] The ability to create multiple nanopores can significantly increase detection frequency. However, a key concern of using multiple nanopores is the possible decrease in sensitivity due to an increased baseline current and thus a small current blockade. To further demonstrate the ability of FIB milling to create multiple nanopores in the same pipette substrate and study how they may affect nanoparticle translocation and detection sensitivity, we milled two pores in a single nanopipette substrate. These pores had different lengths with the shorter pore being 376 nm long with an inner diameter of 186 nm and outer diameter of 269 nm and the longer pore being 1007 nm long with an inner diameter of 180 nm and outer diameter of 277 nm. We observed the translocations of 112 nm particles through each of these

pores simultaneously as shown in **Figure 6.4a**, with one population having roughly three times the amplitude of the other.

Further analysis revealed that the larger amplitude blockades had longer half-widths and therefore belonged to the population of particles translocating the 1007 nm long pore as shown in **Figures 6.4b and 6.4c**. The relationship of half-width and current blockade follows that of the single pore experiments where we see the 1259 nm long pore having larger current blockades of 2.96% versus the 1.59% blockades of the 495 nm pore.

The trend of increasing current blockade from the shorter nanopores to the ~1000 nm long nanopores is shown in **Figure 6.5**. All percent current blockades were observed in nanoparticle translocation experiments at -100 mV. The double pores follow the same trend of the single pores due to the added electrical resistance leading up to the shorter pores. Resistive-pulse amplitude depends upon volume excluded by the pore, and in this case the overall pore volume is that of the two pores combined. The blockades decrease dramatically from their single pore values to 0.82% and 0.27% in the double pore experiment for the longer and shorter pore, respectively. While the double pore geometries are not the same as their single pore comparisons; the trend they exhibit is similar.

The electric field, which electrophoresis and electroosmosis depend upon, should not change as the potential difference across each pore remains the same. We do observe an increase in the average half-width of particle translocations, from 0.309 ms in the 495 nm long single pore to 0.478 ms in the 376 nm long pore and from 0.744 ms in the 1259 nm long single pore to 0.969 ms in the 1007 nm long pore. It is unclear if these differences are significant given that the pores are not identical. We hypothesize that these could be caused by the intermixing of the electroosmotic flows coming through both pores and down the length of the pipette taper.

However, there is not as large of a difference between single and double pore experiments with respect to translocation time as there is with the current blockade.

6.3.6 Finite Element Analysis

To further understand particle translocation in a double-pore pipette, we performed a finite-element simulation of the translocation experiment using COMSOL Multiphysics 5.2a. The geometries of the two pores in the double pore experiment were simulated using SEM measurements to construct the pores. An electric potential of -100 mV is applied across the nanopore from the inside of the pipette to 0 mV outside the pipette. An electric potential map and electric field is generated, the magnitude of which is used to determine the flux of ions through each pore as shown in **Figure 6.6**. A description of the geometry used for the simulation is found in **Figure S6.7**. We use a method for simulating the ionic current blockade that is outlined elsewhere using the Nernst-Planck equation for an ionic species *i* while ignoring convection:[46]

$$J_i = -D_i\left(\Delta C_i - \frac{z_i F}{RT} C_i \nabla \phi\right) \qquad (4)$$

with J_i being the flux, D_i the diffusion coefficient, C_i the concentration, and z_i the charge of ionic species. F, R, and T, are the Faraday's constant, universal gas constant, and temperature. The quantity $\nabla\phi$ is the electric field as determined from our simulation. The ionic flux is calculated at each pore orifice and summed.

The double layer on the nanoparticle and the sidewalls of the pore was ignored for this simulation because of the large difference between the Debye length and pore diameter at the salt concentration used. Our simulation was only of the change in conductivity of the pore with and without an insulating particle displacing electrolyte solution and not of forces acting on the particle. In our simulation, we assume the conductance of the electrolyte solution within the pore

to be the same at every location and the same as the bulk solution conductivity. This is not entirely accurate as there is a double layer along the sidewalls of the nanopore which perturbs the concentration of ions and alters the conductivity. However, under the salt conditions used (100 mM), this double layer has a Debye length of ~1 nm which is small when compared with a 100 nm radius pore. [47] When solution within the pore is displaced by a particle it will likely have the bulk solution conductivity that is unperturbed by the ion concentration gradients within a few nm of the sidewalls. This assumption was not made only because of convenience, but because of experimental evidence showing that the double layer, and therefore electroosmosis, was not noticeably affecting the conductivity of the pore. In cases where the size of the double layer approaches the size of the pore a phenomenon known as ionic current rectification[48] is seen where the concentration of cations within the double layer near the pore orifice alters the conductivity of the nanopore and gives the nanopore a rectified i-V response. All side pores tested showed a linear Ohmic response in 100 mM KCl at negative and positive potentials. We acknowledge that we introduce error into our simulation by ignoring these double layer effects, however we estimate it to be negligible based on experimental i-V curves and theoretical predictions of the Debye length (~1 nm) when compared with our nanopore radii (~100 nm). This assumption is not without precedent and similar treatment is found in other nanopore-nanoparticle translocation simulations.[49]

The simulations show a decreasing potential along the length of the taper of the pulled pipette. This is from an additional resistance between the 376 nm long pore and the 1007 nm long pore which is farther up the taper. This additional resistance results in a smaller current blockade from translocating nanoparticles in the shorter pore. These simulations support both our single and double pore experiments with respect to observed current blockades.

To simulate a maximum blockade a 112 nm diameter sphere was placed within the same plane as the inner pore, which has the smaller diameter and is shown in **Figure S6.8**. This was done separately for each pore in the double pore experiment and the current reduction in each case was compared with the current when there was no particle present. The shorter 376 nm long pore had about half of the conductance of the larger 1007 nm pore and because of this had a smaller blockade when a particle was present in its sensing zone.

Further simulations of a single side pore were performed to examine the differences between end pores and side pores. The electric field along the center of the pore was examined with simulations results plotted for a nanopore of radius 75 nm with a half-cone angle of 8.5° in **Figure 6.7**. The electric field maximum occurs at the nanopore's most constricted orifice and follows a trend of being higher for shorter pores. More importantly, the average electric field magnitude within the confines of each pore drops more dramatically for longer pores and end pores. This agrees with our experimental results showing an exponential relationship between translocation time and pore length. Not only does the pore have a longer distance to traverse, but the average electric field driving the electroosmosis that is acting on the particle is weaker.

The relationship between half-cone angle, pore radius, and pore length and their effect on the average electric field magnitude along the axis of the pore were further studied. The average electric field magnitude as it relates to pore radius and half-cone angle is shown for an end pore of length 500 nm and 4000 nm in **Figure 6.8a-b**. The methodology for calculating the average electric field magnitude for end pores is shown in **Figure S6.9a-b**. Notably, the electric field within an end pore is proportional to half-cone angle and inversely proportional to pore radius. The electric field within a side pore is also concentrated more highly in pores with smaller radii as shown in **Figure 6.8c-d**. However, in contrast to an end pore, the electric field in a side pore decreases with an

increasing cone angle. Also, the change in electric field with cone angle is more muted in side pores when compared to end pores. This is illustrated in **Figure 6.8e-f** where the scales for the side pore charts have been changed to those of the end pores, showing minimal change.

Figure 6.9a quantifies the relationship between electric field and pore radius for a range of experimentally relevant radii for both side pores and end pores of 500 nm length and a half-cone angle of 8.5°. The average electric field magnitude in the side pores decreases by 23% at a pore radius of 150 nm from its value at 50 nm. The end pore electric field reduces to 46% of its average magnitude at a radius of 150 nm compared to its value at 50 nm. For experiments we had used side pores of different lengths and slightly different pore radii and this validates our experimental method by showing how robust the side pore is to changes in its pore radius. Further, in **Figure 6.9b**, we observe that both the end pore and side pore have a similar trend in average electric field magnitude over a range of pore lengths from 500 nm to 4000 nm for a pore of radius 75 nm and half-cone angle 8.5°. In **Figure 6.9c** we show the change in electric field with half-cone angle for a pore of radius 75 nm and length 500 nm. In this case, the average electric field magnitude of a side pore decreases by less than 10% over a range of 2-10° whereas that of an end pore increases by 110%. This sensitivity to changes in cone angle is a major disadvantage of end pores compared to side pores. The reduced sensitivity to changes in geometry in general is a boon when working with side pores, not only because all geometric aspects are known, but because pore radius and pore cone angle do not need to be so tightly controlled and monitored.

6.4 Conclusions

We have demonstrated the use of sealed quartz nanopipettes as a new platform for microfabricated nanopores. An FIB milling process is used on the side walls of a sealed quartz pipette enabling fast and reproducible fabrication of low noise, conical shape quartz nanopores

down to ~70 nm in diameter with tunable pore size and length. Pores of smaller dimensions can be prepared using more advanced FIB systems with a higher spatial resolution. Nanopore geometry, including inner and outer pore diameter, pore length, and cone-angle, can be fully characterized using SEM. Fabricating and using nanopores on the side walls of a pulled pipette avoids the highly restricted volume in the tip region and its associated mass-transfer and ionic resistance. Nanoparticle translocation has been demonstrated using pipettes containing both single pores and double pores. The use of two pores of differing lengths within a single pipette further underscores the differing particle dynamics of pores of different lengths. Further simulations illustrate that the end pore has a remarkably sensitive relationship between electric field and pore geometry that is avoided by using a side pore, where the electric field is primarily dependent on the pore length. This unique system will prove useful for further studies on particle translocation dynamics and development of nanopore-based sensors.

6.5 Schemes and Figures

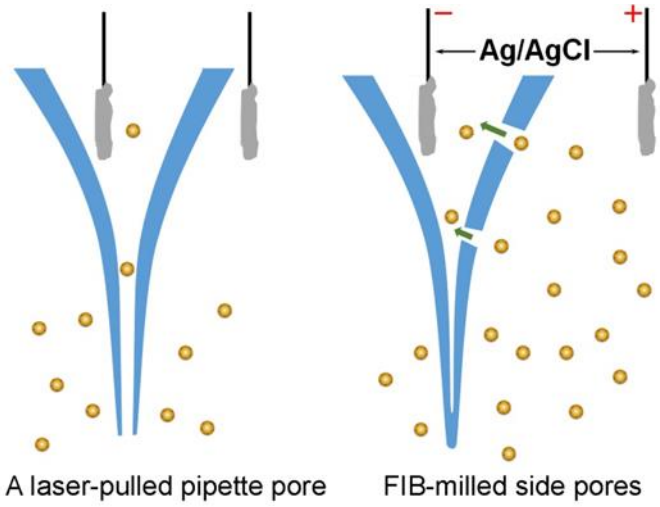

Scheme 6.1. Nanoparticle translocation through a laser-pulled pipette pore and FIB-milled side pores.

On the left is shown a typical laser-pulled nanopipette, referred to in the text as an end pore. On the right is a laser-pulled nanopipette that has had its end heat sealed before having new nanopores milled into the taper using FIB.

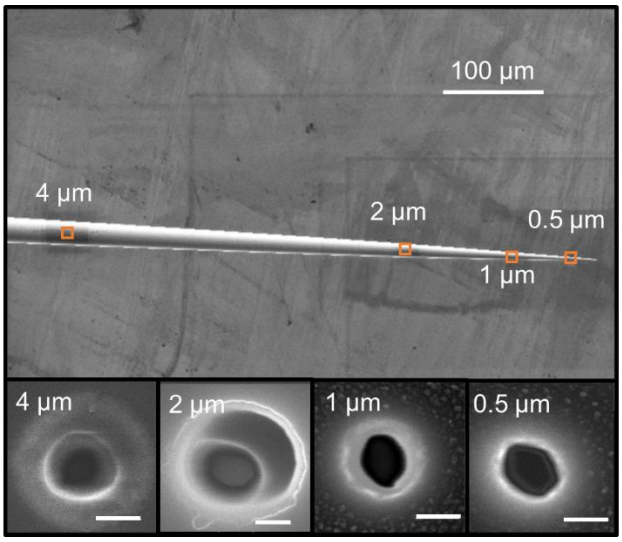

Figure 6.1. SEM image of locations on the sealed quartz capillary taper for FIB milling. FIB milling at these locations creates pores that are nominally 500 nm, 1 µm, 2 µm, and 4 µm long. The scale bars for the inset nanopores are 200 nm.

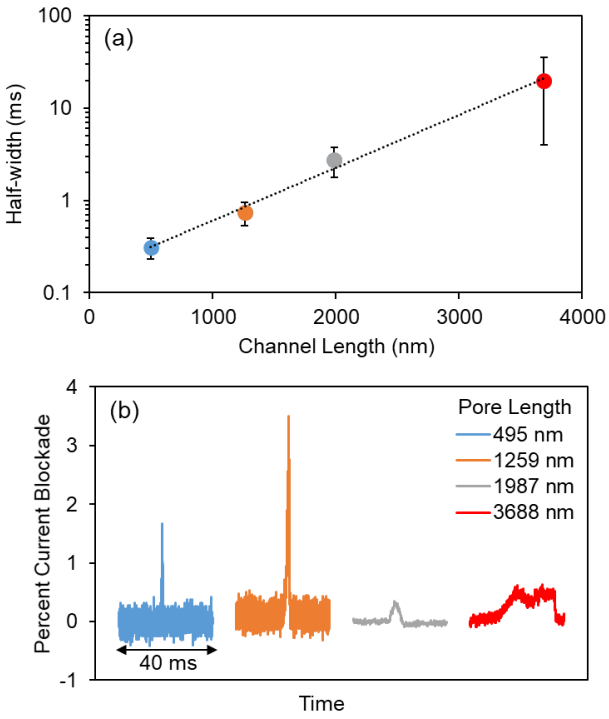

Figure 6.2. Half-width and ionic current blockades of pores varied by pore length.

(a) The half-width of translocation events changes exponentially with pore length. Half-widths were all measured at -100 mV. The dashed line is an exponential fit to the data. Error bars are one standard deviation. (b) Representative resistive current pulses for the 495 nm, 1259 nm, 1987 nm, and 3688 nm long nanopores. All pores had an inner diameter between 150 to 250 nm and an outer diameter between 250 to 350 nm.

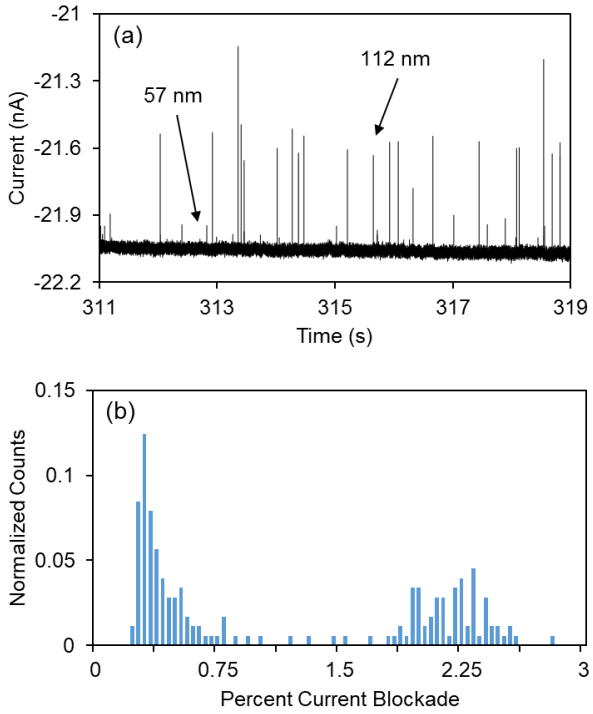

Figure 6.3. Nanopore detection of mixed size nanoparticle solution.

(a) An 8-second current-time trace collected at -400 mV showing particle size discrimination between 57 nm and 112 nm polystyrene nanoparticles using a 495 nm long nanopore. (b) Histogram of current blockades showing the two populations of nanoparticles.

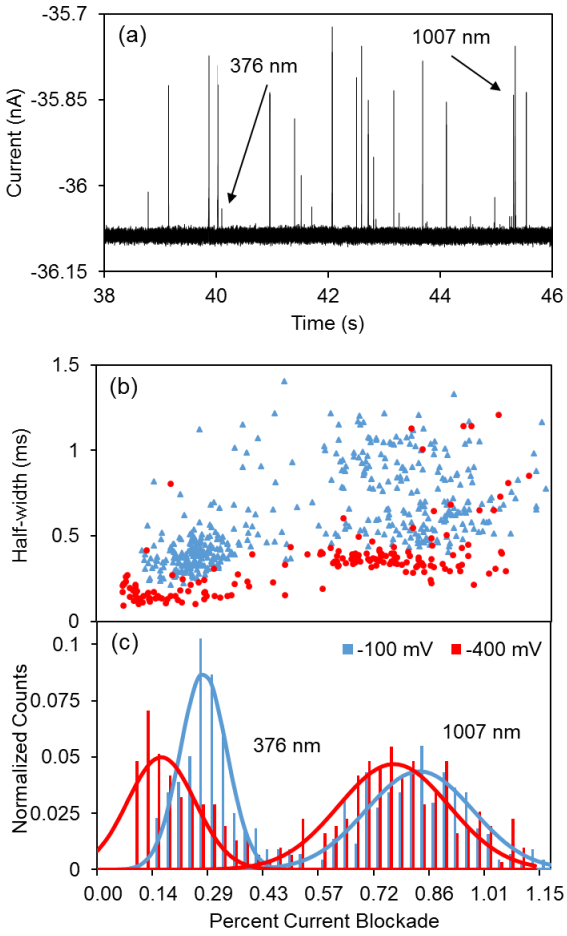

Figure 6.4. Double-nanopore detection of homogenous nanoparticle solution.

(a) An 8-second current-time trace collected at -400 mV using a sealed pipette containing two pores of different lengths showing detection of 112 nm polystyrene particles. The 376-nm-long pore has an inner diameter of 186 nm and the 1007-nm-long pore has an inner diameter of 180 nm. (b) A scatter plot of individual detection events showing their half-widths and current blockades from results in (a). (c) Histogram of current blockades for the 376 nm and 1007 nm long nanopores. Overlayed are Gaussians fit to each of the peaks.

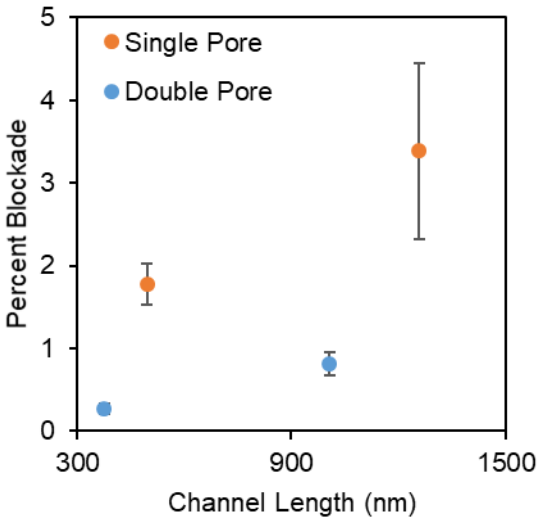

Figure 6.5. Percent current blockades observed in nanoparticle translocation experiments at -100 mV.

The double pores follow the same trend of the single pores due to the added electrical resistance leading up to the shorter pores. All pores had an inner diameter of 150 to 250 nm and an outer diameter of 250 to 350 nm.

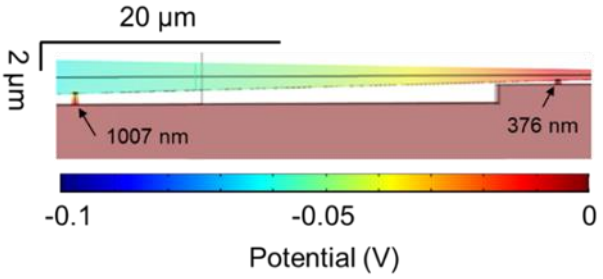

Pore	Observed Blockade (%)	Simulated Blockade (%)
376 nm long	0.27	0.39
1007 nm long	0.82	0.88

Figure 6.6. Nanopore finite element analysis results.

(Top) Simulated potential surface profile for the double pores of lengths 376 nm and 1007 nm. The cumulative in-series resistance of the pipette taper and the shorter 376 nm pore is greater than that of the 1007 nm pore. (Bottom) Table comparing observed current blockades with those simulated.

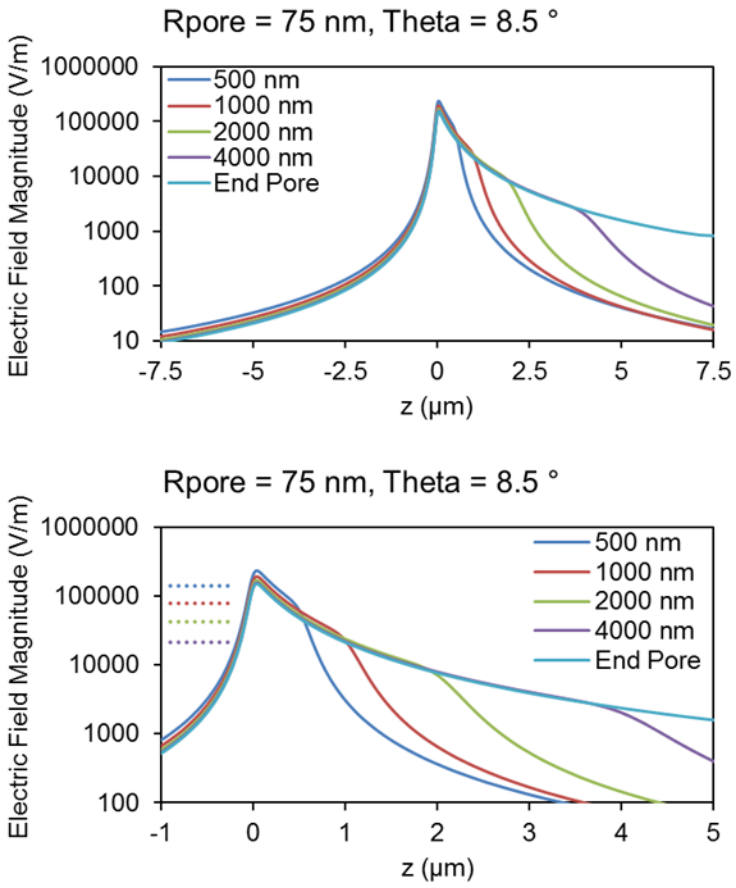

Figure 6.7. Electric field distribution of side pore vs end pore.

(Top) The electric field magnitude of the various side pore lengths and an end pore along the axis of symmetry down the center of the pore. There is a rapid drop in the field outside of the confines of the pore. (Bottom) A zoomed in section of the top graph showing the rapid drop in the field outside of the pore. The colored dotted lines to the left of the peak are the values of the average electric field magnitude within the confines of each pore. This demonstrates how the longer pores have a lower average field.

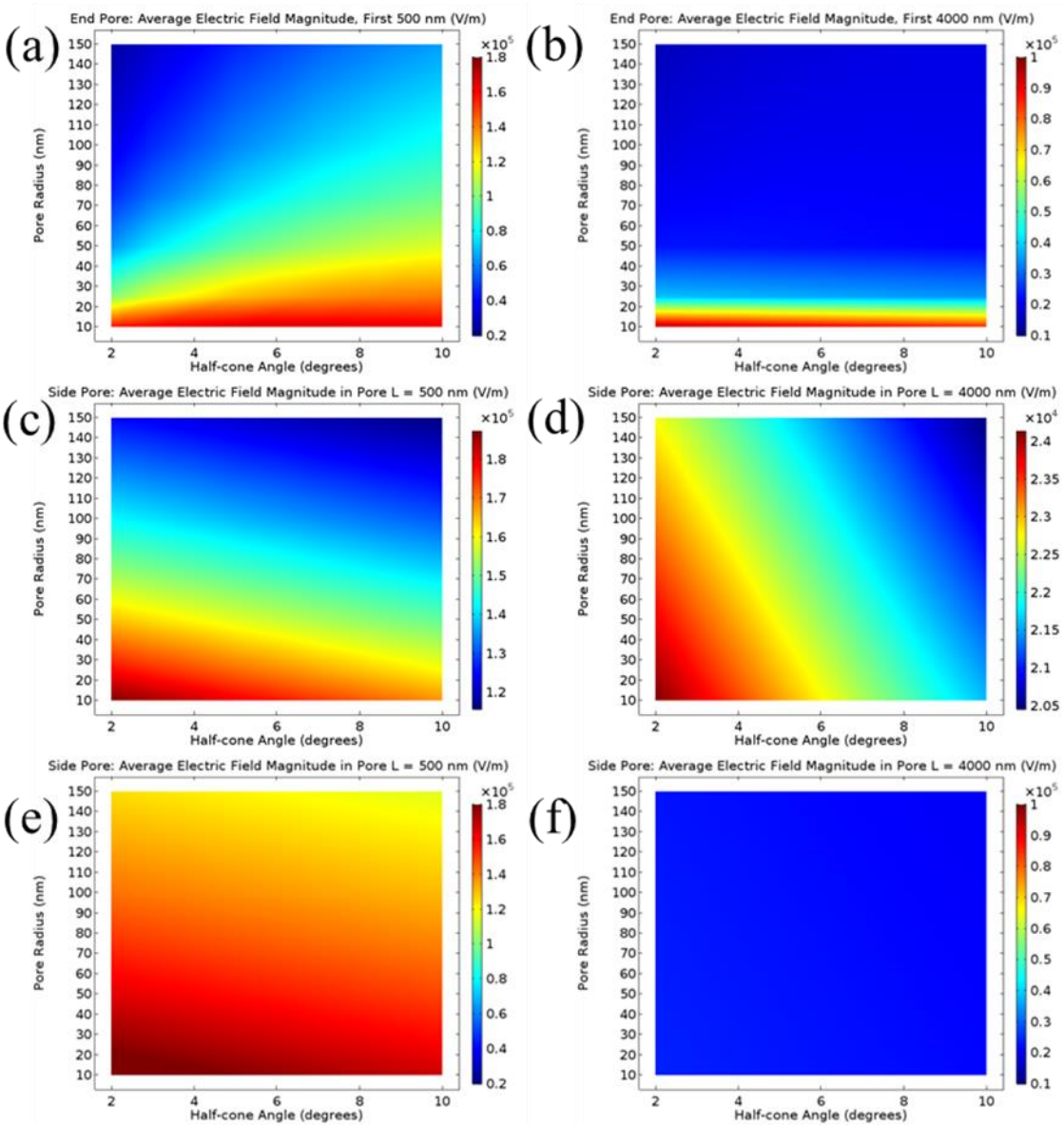

Figure 6.8. 2D tables of average electric field magnitude within side pores vs end pores depending on geometry.

(a) and (b) show the electric field dependence on pore radius and half-cone angle for the typical quartz nanopore "end pore". (c) and (d) show the electric field dependence on pore radius and half-cone angle for our "side pore". (e) and (f) show the electric field dependence on pore radius and half-cone angle for our "side pore" using the same electric field range as with the end pores to show the stronger geometric dependence of the electric field of the end pores.

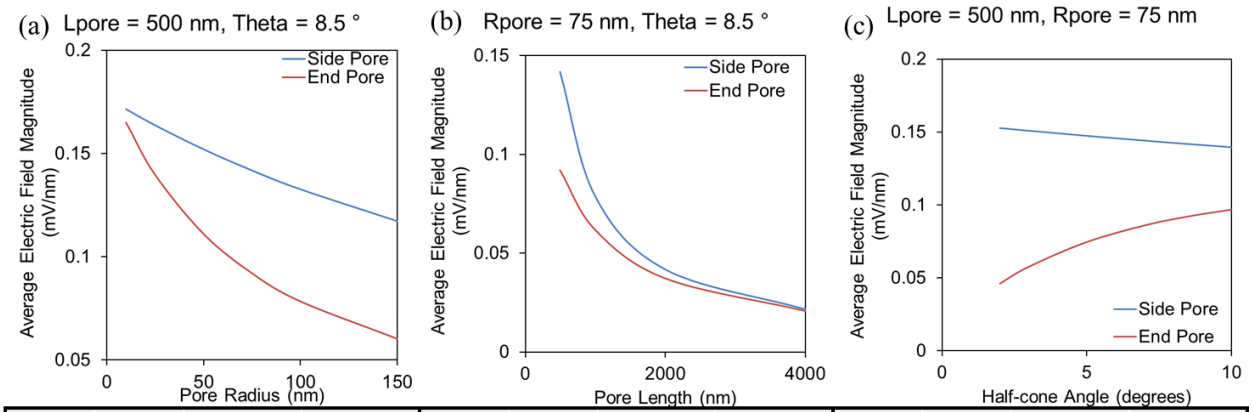

Pore Radius 1 (nm)	Pore Radius 2 (nm)	Percent Decrease Side Pore	Percent Decrease End Pore
25	50	7	20
50	100	13	29
75	150	17	34
50	150	23	46

Pore Length 1 (nm)	Pore Length 2 (nm)	Percent Decrease Side Pore	Percent Decrease End Pore
500	1000	44	33
1000	2000	47	40
2000	4000	49	44
500	4000	85	77

Half-cone Angle 1 (°)	Half-cone Angle 2 (°)	Percent Decrease Side Pore	Percent Increase End Pore
2	5	4	62
3	7	5	49
5	10	5	30
2	10	9	110

Figure 6.9. 1D graphs of average electric field magnitude within side pores vs end pores depending on geometry.

Tables beneath each graph calculate the percent change in the average electric field magnitude when going from parameter 1 to parameter 2 for side pores and end pores. (a) The electric field dependence on pore radius. The end pore is more sensitive to changes in pore radius than the side pore. (b) The electric field dependence on pore length. Side pores and end pores are about equally sensitive to changes in length. Note that for the end pore this is just changing the distance used to average the electric field. (c) The electric field dependence on pore half-cone angle. The end pore is much more sensitive and experiences an increase rather than a decrease when half-cone angle is increased.

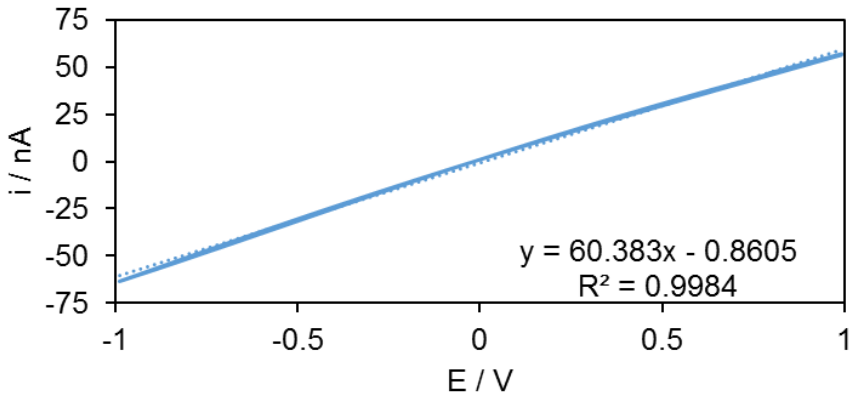

Figure S6.1. Example of a side pore i-V curve.

A current-voltage response collected at 100 mV/s from a 263 nm diameter FIB-milled quartz nanopore in 100 mM KCl. The pore length is 1259 nm determined from SEM. The dotted line is a linear fit of the current-voltage data.

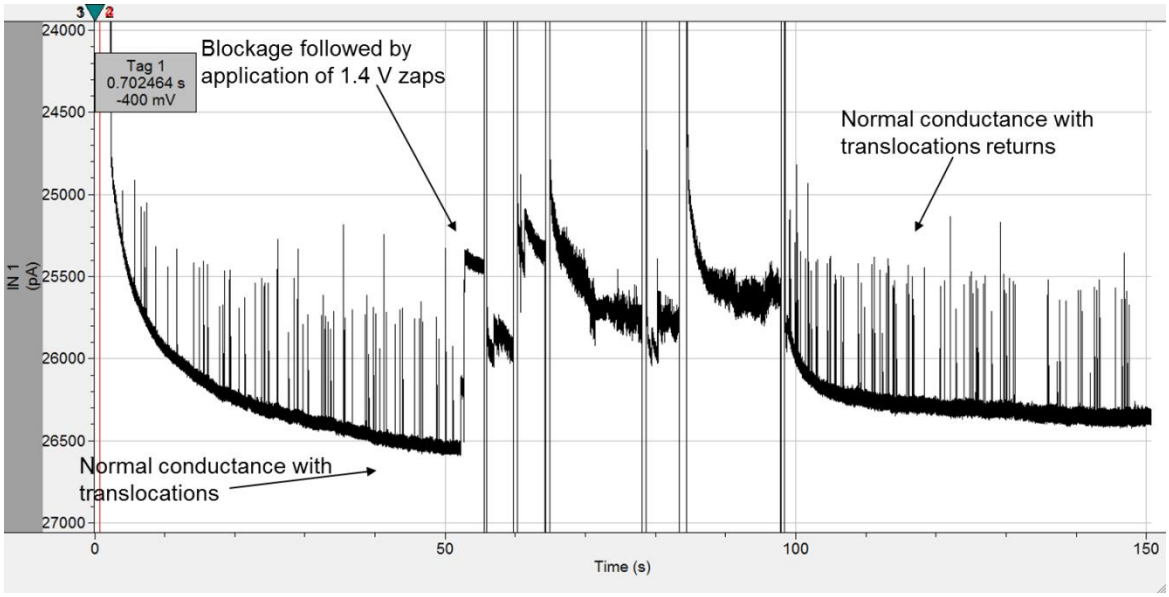

Figure S6.2. Example of clearing a pore clog with 1.4 V zaps.

Pore blockages were more common with longer pores. The solution contained 100 mM KCl and 10 mM K_2HPO_4/KH_2PO_4 at pH 7.4 and 0.1% Triton X-100. The 112 nm polystyrene particles were concentrated at 5×10^{10} particles/mL. The voltage applied was -400 mV from the inside of the pipette.

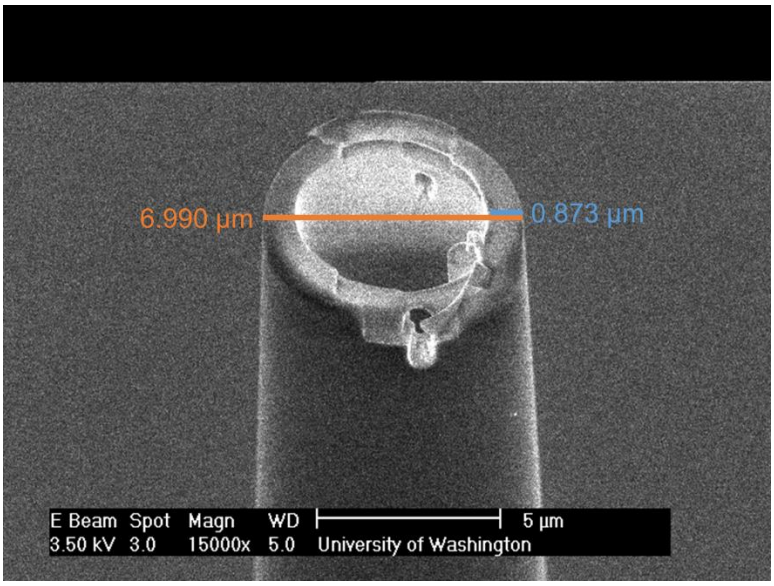

Figure S6.3. Nanopipette wall thickness verification.

A pulled quartz capillary with a failed pore in it which we cut open to measure the ratio of inner and outer diameter. The original capillary had a 0.7 mm I. D. and a 1.0 mm O. D. meaning the sidewall should be 15% of the capillary's width. After pulling we find that this ratio is still very close, about 12.5%.

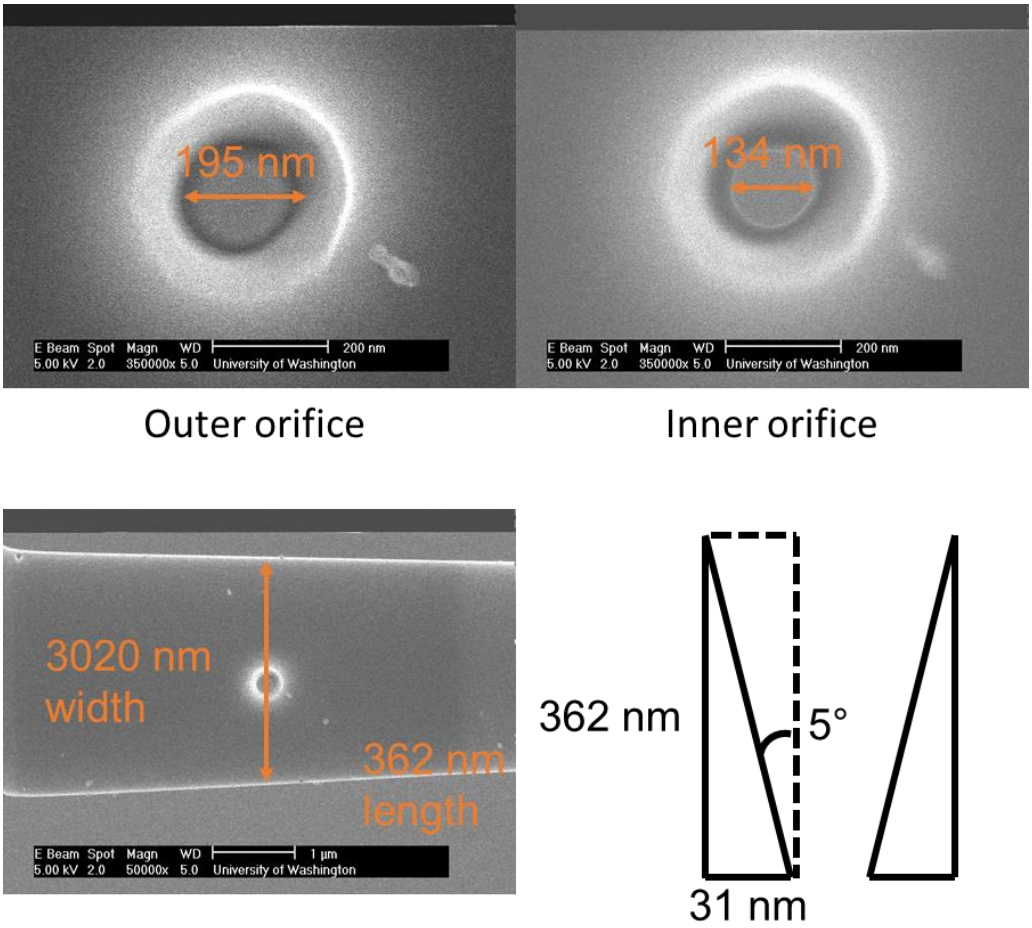

Figure S6.4. Method for determining pore diameter and length.

(Top left) Focusing on the outer orifice and measuring the outer diameter. (Top right) Focusing on the inner orifice and measuring the inner diameter. We were not able to do this for pores larger than ~2 µm. (Bottom left) Measuring the capillary width at the location of the drilled pore and calculating the wall thickness from it (~12%). (Bottom right) Geometry employed to calculate the half-cone angle.

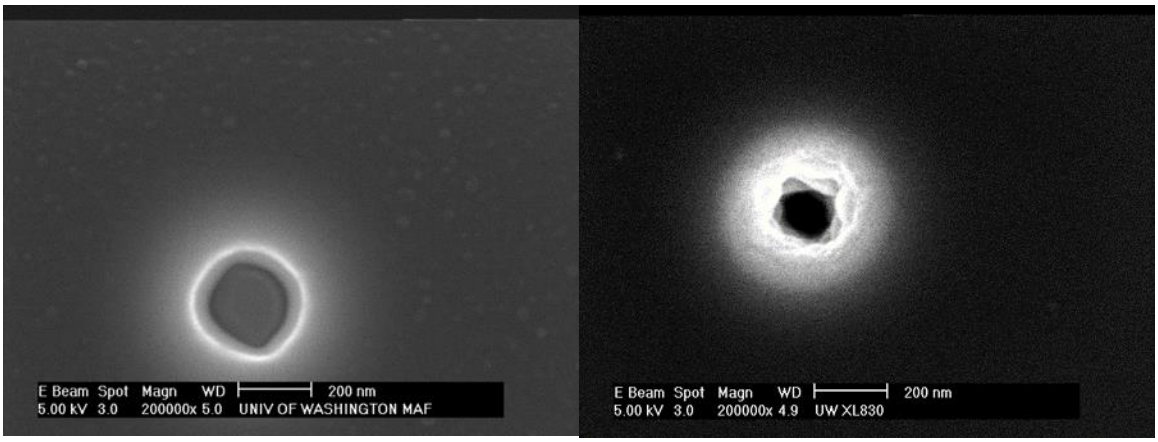

Figure S6.5. Side pore sidewall roughness.

Example of a good pore with smooth sidewalls (left) versus a bad pore with rough sidewalls (right).

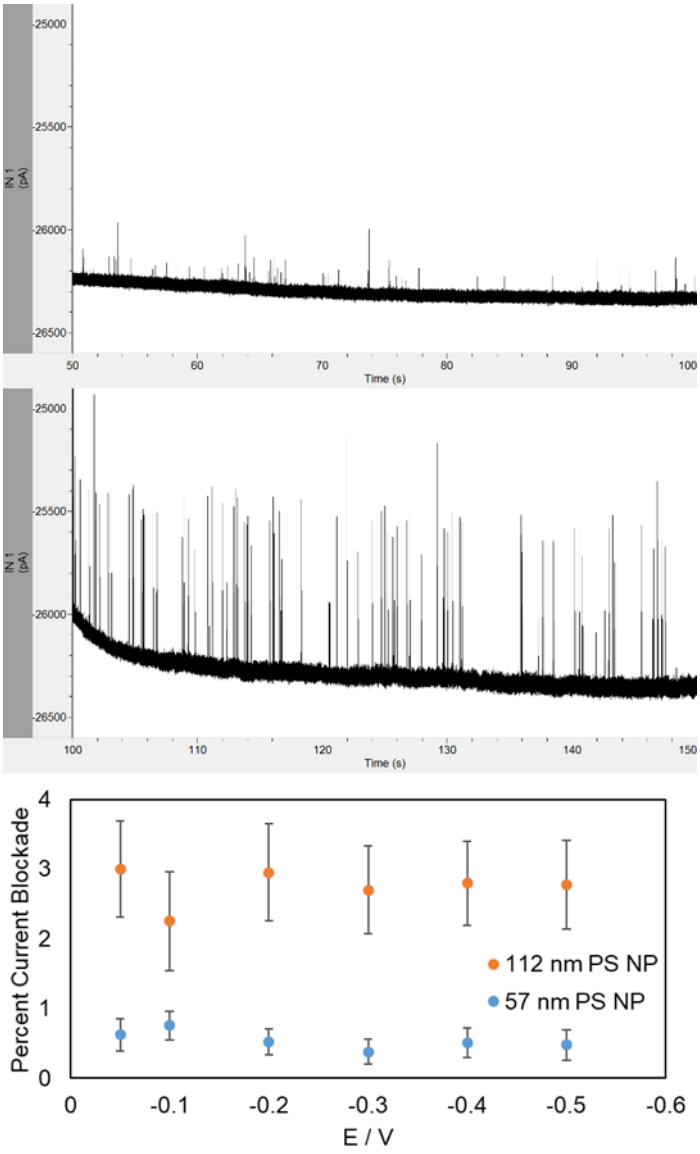

Figure S6.6. Example traces of 57 nm and 112 nm polystyrene nanoparticles and voltage dependence of percent current blockade.

(Top) 57 nm polystyrene nanoparticle translocations through a 1259 nm long pore. (Middle) 112 nm polystyrene nanoparticle translocations through the same pore. Both figures have the same current range to illustrate the difference in current blockade. (Bottom) Voltage dependence of the percent current blockade of 57 nm and 112 nm polystyrene nanoparticles through the 1259 nm long pore.

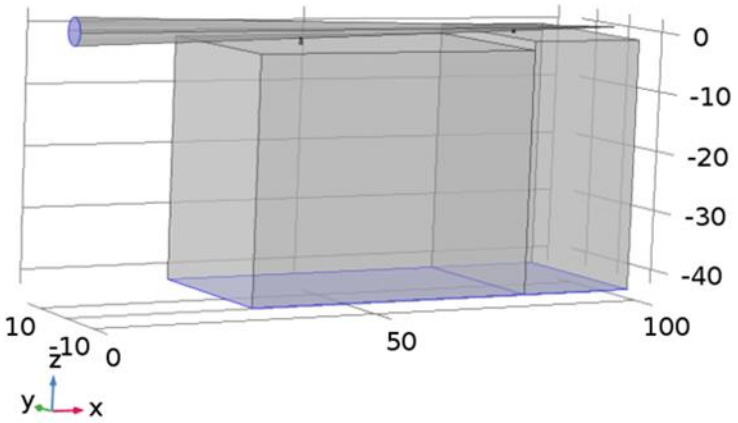

Figure S6.7. COMSOL simulation geometry and parameters.

Units are in micrometers. Only the solution volume on one side of the pipette was simulated to reduce computational cost. The highlighted circle on the border of the pipette is set to -0.1 V. The bottom highlighted surfaces were set to 0 V. All other surfaces were considered to be insulating with no charge. For concentration boundary conditions all surfaces except those constituting the walls of the pipette and the walls of nanopores were set to bulk concentration, 100 mM. The viscosity was 8.9×10^{-4} Pa·s which is that of water at 25 °C. A relative permittivity of 76 was used for the 100 mM KCl solution.[50] The diffusion coefficients of chloride and potassium ions were 2.023×10^{-9} m^2/s and 1.957×10^{-9} m^2/s, respectively.[46]

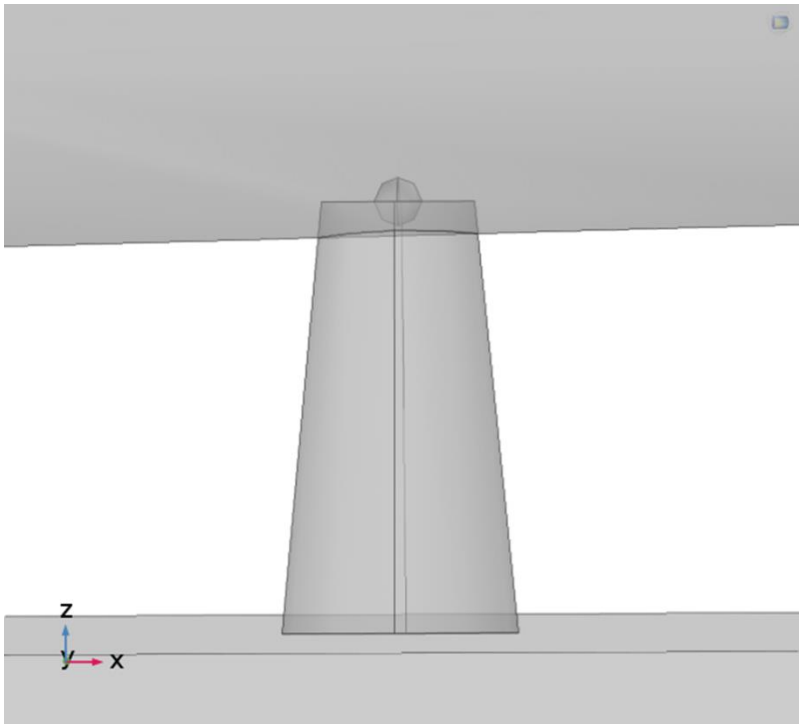

Figure S6.8. Nanoparticle ionic current blockade simulation method.

Current blockades were measured by placing a non-conducting 112 nm diameter sphere in plane with the inner orifice of either pore. The flux was calculated at this plane for both pores and summed. This was done with the 112 nm diameter sphere in either pore and in neither pore.

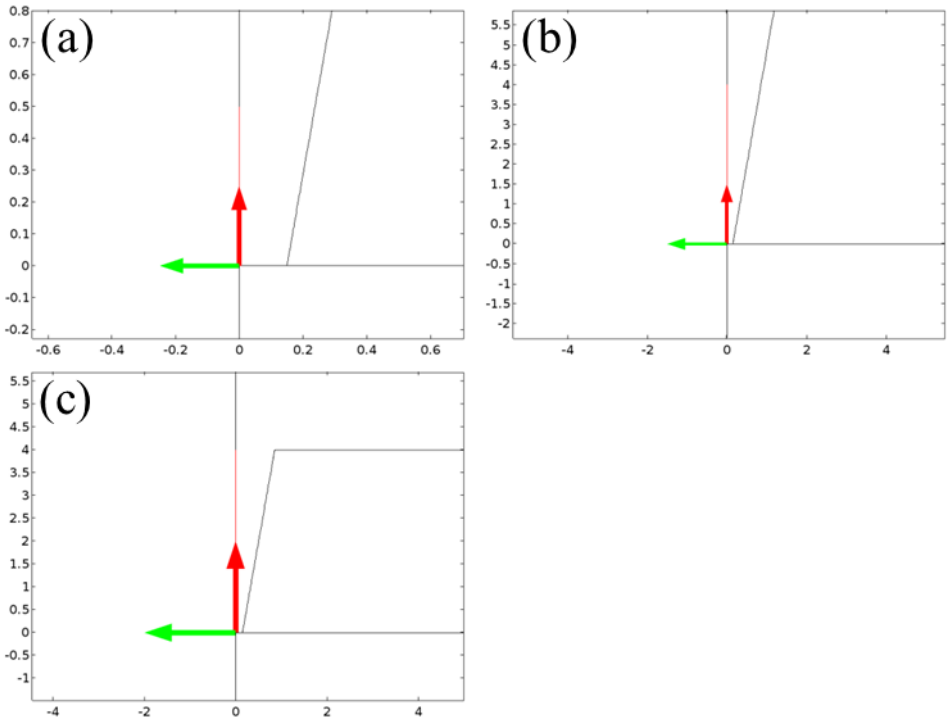

Figure S6.9. Cut line used for averaging electric field magnitude in COMSOL simulations. The red line including and extending past the red arrow illustrates the section of the pore used for averaging the electric field magnitude during simulations. Electric fields were simulated in a 2D model with axial symmetry. The cut lines shown go through the center of the pore which in this case is the axis of symmetry. (a) The 500 nm long cut line used for averaging the electric field magnitude within the first 500 nm of the end pore orifice. (b) The 4000 nm long cut line used for averaging the electric field magnitude within the first 4000 nm of the end pore orifice. (c) The cut line used for the side pores which was the length of the pore in question.

6.6 References

(1) Shi, W.; Friedman, A. K.; Baker, L. A. *Anal. Chem.* **2017**, *89*, 157−188.

(2) Manrao, E. A.; Derrington, I. M.; Laszlo, A. H.; Langford, K. W.; Hopper, M. K.; Gillgren, N.; Pavlenok, M.; Niederweis, M.; Gundlach, J. H. *Nat. Biotechnol*. **2012**, *30*, 349−354.

(3) Li, W.; Gong, L.; Bayley, H. *Agnew. Chem. Int. Ed*. **2013**, *52*, 4350−4355.

(4) Perera, R. T.; Fleming, A. M.; Johnson, R. P.; Burrows, C. J.; White, H. S. *Nanotechnology* **2015**, *26*, 074002.

(5) An, N.; Fleming, A. M.; White, H. S.; Burrows, C. J. *ACS Nano* **2015**, *9*, 4296−4307.

(6) Ayub, M.; Bayley, H. *Nano Lett.* **2012**, *12*, 5637−5643.

(7) Li, G.; Zhang, Z.; Lin, X. *Chin. J. Anal. Chem*. **2010**, *38*, 1698−1702.

(8) Heins, E. A.; Siwy, Z. S.; Baker, L. A.; Martin, C. R. *Nano Lett*. **2005**, *5*, 1824−1829.

(9) Movileanu, L. *Soft Matter* **2008**, *4*, 925−931.

(10) Harms, Z. D.; Mogensen, K. B.; Nunes, P. S.; Zhou, K.; Hildenbrand, B. W.; Mitra, I.; Tan, Z.; Zlotnick, A.; Kutter, J. P.; Jacobson, S. C. *Anal. Chem*. **2011**, *83*, 9573−9578.

(11) Zhou, K.; Li, L.; Tan, Z.; Zlotnick, A.; Jacobson, S. C. *J. Am. Chem. Soc*. **2011**, *133*, 1618−1621.

(12) Berge, L. I.; Feder, J.; Jøssang, T. *Rev. Sci. Instrum*. **1989**, *60*, 2756−2763.

(13) Ito, T.; Sun, L.; Crooks R. M. *Anal. Chem.* **2003**, *75*, 2399−2406.

(14) Coulter, W. H. *Means for Counting Particles Suspended in a Fluid* **1953**, US Patent No. 2656508.

(15) Pevarnik, M.; Healy, K.; Toimil-Molares, M. E.; Morrison, A.; Létant, S. E.; Siwy, Z. S. *ACS Nano* **2012**, *6*, 7295−7302.

(16) Zhang, B.; Galusha, G.; Shiozawa, P. G.; Wang, G.; Bergren, A. J.; Johns, R. M.; White, R. J.; Ervin, E. N.; Cauley, C. C.; White, H. S. *Anal. Chem.* **2007**, *79*, 4778−4787.

(17) Gao, C.; Ding, S.; Tan, Q.; Gu, L-Q. *Anal. Chem.* **2009,** *81*, 80-86.

(18) Tsutsui, M.; Hongo, S.; He, Y.; Taniguchi, M.; Gemma, N.; Kawai, T. *ACS Nano* **2012**, *6*, 3499−3505.

(19) Qiu, Y.; Dawid, A.; Siwy, Z. S. *J. Phys. Chem. C* **2017**, *121*, 6255−6263.

(20) Yang, C.; Hinkle, P.; Menestrina, J.; Vlassiouk, I. V.; Siwy, Z. S. *J. Phys. Chem. Lett.* **2016**, *7*, 4152−4158.

(21) Ito, T.; Sun, L.; Henriquez, R. R.; Crooks, R. M. *Acc. Chem. Res.* **2004**, *37*, 937−945.

(22) Heerema, S. J.; Dekker, C. *Nat. Nanotechnol.* **2016**, *11*, 127−136.

(23) Guerrette, J. P.; Zhang, B. *J. Am. Chem. Soc.* **2010**, *132*, 17088−17091.

(24) Storm, A. J.; Chem, J. H.; Ling, X. S.; Zandbergen, H. W.; Dekker, C. *Nat. Mater.* **2003**, *2*, 537−540.

(25) Li, J.; Stein, D.; McMullan, C.; Branton, D.; Aziz, M. J.; Golovchenko, J. A. *Nature* **2001**, *412*, 166−169.

(26) Kwok, H.; Briggs, K.; Tabard-Cossa, V. *PLoS ONE* **2014**, *9*, e92880.

(27) Grzywna, Z. J.; Siwy, Z.; Bashford, C. L. *J. Membrane Sci.* **1996**, *121*, 261−269.

(28) Kennedy, E.; Dong, Z.; Tennant, C.; Timp, G. *Nat. Nanotech.* **2016**, *11*, 968−976.

(29) Oja, S. M.; Wood, M.; Zhang, B. *Anal. Chem.* **2013**, *85*, 473−486.

(30) Murray, R. W. *Chem. Rev.* **2008**, *108*, 2688−2720.

(31) Piper, J. D.; Clarke, R.W.; Korchev, Y. E,; Ying, L. M,; Klenerman, D. *J. Am. Chem. Soc.* **2006**, *128*, 16462–16463.

(32) Wei, C.; Bard, A. J.; Feldberg, S. W. *Anal. Chem.* **1997**, *69*, 4627–4633.

(33) Chen, C-C.; Zhou, Y.; Baker, L. A. *Annu. Rev. Anal. Chem.* **2012**, *5*, 207−228.

(34) Lee, M. H.; Kumar, A.; Park, K. B.; Cho, S. Y.; Kim, H. M.; Lim, M. C.; Kim, Y. R.; Kim, K. B. *Sci. Rep.* **2014**, *4*, 7448.

(35) Tabard-Cossa, V.; Trivedi, D.; Wiggin, M.; Jetha, N. N.; Marziali, A. *Nanotechnology* **2007**, *18*, 305505.

(36) Levis, R. A. and Rae, J. L. *Biophys J.* **1993**, *65*, 1666–1677.

(37) Perry, D.; Momotenko, D.; Lazenby, R. A.; Kang, M.; Unwin, P. R. *Anal. Chem.* **2016,** *88*, 5523–5530.

(38) Zhang, B.; Wood, M.; Lee, H. *Anal. Chem.* **2009**, *81*, 5541−5548.

(39) Li, Y.; Bergman, D.; Zhang, B. *Anal. Chem.* **2009**, *81*, 5496–5502.

(40) Lanyon, Y. H.; De Marzi, G.; Watson, Y. E.; Quinn, A. J.; Gleeson, J. P.; Redmond, G.; Arrigan, D. W. M. *Anal. Chem.* **2007**, *79*, 3048-3055.

(41) Smeets, R. M. M.; Keyser, U. F.; Dekker, N. H.; Dekker, C. *Proc. Nat. Acad. Sci. U.S.A.* **2008**, *105*, 417−421.

(42) Smeets, R. M. M.; Dekker, N. H.; Dekker, C. *Nanotechnology* **2009**, *20*, 095501.

(43) Davenport, M.; Healy, K.; Pevarnik, M.; Teslich, N.; Cabrini, S.; Morrison, A. P.; Siwy, Z. S., Letant, S. E. *ACS Nano* **2012**, *6*, 8366−8380.

(44) German, S. R.; Luo, L.; White, H. S.; Mega, T. L. *J. Phys. Chem. C*, **2012**, *117*, 703-711.

(45) Ervin, E. N.; White, R. J. and White, H. S. *Anal. Chem.* **2009**, *81*, 533–537.

(46) Lan, W. J.; Kubeil, C.; Xiong, J. W.; Bund, A.; White, H. S. *J. Phys. Chem. C* **2014,** *118*, 2726–2734.

(47) Yusko, E. C.; An, R.; Mayer, M. *ACS Nano*, **2010**, *4*, 477–487.

(48) Wei, C.; Bard, A. J.; Feldberg, S. W. *Anal. Chem.* **1997**, *69*, 4627−4633.

(49) Lan, W. J.; Holden, D. A.; Liu, J.; White, H. S. *J. Phys. Chem. C* **2011**, *115*, 18445-18452.

(50) van Beek, W. M., Mandel, M. *J. Chem. Soc., Faraday Trans. 1* **1977**, 74, 2339−2351.

Bibliography

Abe, H.; Ino, K.; Li, C. Z.; Kanno, Y.; Inoue, K. Y.; Suda, A.; Kunikata, R.; Matsudaira, M.; Takahashi, Y.; Shiku, H.; Matsue, T. *Anal. Chem*. **2015**, *87*, 6364–6370.

Amatore, C.; Deakin, M. R.; Wightman, R. M. *J. Electroanal. Chem.* **1987**, *220*, 49–63.

Amatore, C.; Fosset, B. *Anal. Chem.* **1996**, *68*, 4377-4388.

Amatore, C.; Maisonhaute, E. *Anal. Chem.* **2005**, *77*, 305A–311A.

Amatore, C.; Savéant, J. M.; Tessier, D. *J. Electroanal. Chem.* **1983**, *147*, 39–51.

An, N.; Fleming, A. M.; White, H. S.; Burrows, C. J. *ACS Nano* **2015**, *9*, 4296−4307.

Andrieux, C. P.; Garreau, D.; Hapiot, P.; Savéant, J. M. *J. Electroanal. Chem.* **1988**, *248*, 447–450.

Arrigan, D. W. *Analyst*, **2004**, *129*, 1157–1165.

Ayub, M.; Bayley, H. *Nano Lett*. **2012**, *12*, 5637−5643.

Bard, A. J., Parsons, R., and Jordan, J. *Standard Potentials in Aqueous Solutions,* Marcel Dekker: New York, 1985.

Bard, A. J.; Fan, F.-R. F.; Kwak, J.; Lev, O. *Anal. Chem.* **1989**, *61*, 132-138.

Bard, A. J.; Faulkner, L. R. *Electrochemical Methods*, 2nd ed.; John Wiley & Sons: New York, 2001.

Bayley, H.; Martin, C. R. *Chem. Rev.* **2000**, *100*, 2575-2594.

Berge, L. I.; Feder, J.; Jøssang, T. *Rev. Sci. Instrum*. **1989**, *60*, 2756−2763.

Boika, A.; Thorgaard, S. N.; Bard, A. J. *J. Phys. Chem. B* **2013**, *117*, 4371-4380.

Butt, H.-J.; Cappella, B.; Kappl, M. *Surf. Sci. Rep.* **2005**, *59*, 1-152.

Chen, C.-C.; Zhou, Y.; Baker, L. *Annu. Rev. Anal. Chem.* **2012**, *5*, 207-228.

Chen, L.; He, H.; Jin, Y. *Anal. Chem.* **2015**, *87*, 522-529.

Chen, Q.; McKelvey, K.; Edwards, M. A.; White, H. S. *J. Phys. Chem. C* **2016**, *120*, 17251-17260.

Chen, S.; Kucernak, A. *Electrochem. Commun.* **2002**, *4*, 80-85.

Chen, S.; Kucernak, A. *J. Phys. Chem. B* **2002**, *106*, 9396-9404.

Coulter, W. H. *Means for Counting Particles Suspended in a Fluid* **1953**, US Patent No. 2656508.

Cox, J. T.; Gunderson, C. G.; Zhang, B. *Electroanalysis* **2013**, *25*, 2151-2158.

daRosa, C. P.; Iglesia, E.; Maboudian, R. *Electrochim. Acta* **2009**, *12*, 3270-3277.

Darvish, A.; Goyal, G.; Aneja, R.; Sundaram, R. V. K.; Lee, K.; Ahn, C. W.; Kim, K-B.; Vlahovska, P. M.; Kim, M. J. *Nanoscale* **2016**, *8*, 14420-14431.

Davenport, M.; Healy, K.; Pevarnik, M.; Teslich, N.; Cabrini, S.; Morrison, A. P.; Siwy, Z. S.; Létant, S. E. *ACS Nano* **2012**, *9*, 8366-8380.

Davies, T. J.; Ward-Jones, S.; Banks, C. E.; del Campo, J.; Mas, R.; Muñoz, F. X.; Compton, R. G. *J. Electroanal. Chem.* **2005**, *585*, 51–62.

Day, T. M.; Unwin, P. R.; Macpherson, J. V. *Nano Lett.* **2007**, *7*, 51–57.

Edwards, M. A.; German, S. R.; Dick, J. E.; Bard, A. J.; White, H. S. *ACS Nano* **2015**, *9*, 12274-12282.

Ervin, E. N.; White, R. J. and White, H. S. *Anal. Chem.* **2009**, *81*, 533–537.

Everett, D. H. *Basic Principles of Colloid Science*; The Royal Society of Chemistry: London, 1988.

Feeney, R.; Kounaves, S. P. *Anal. Chem*. **2000**, *72*, 2222–2228.

Gao, C.; Ding, S.; Tan, Q.; Gu, L-Q. *Anal. Chem.* **2009,** *81*, 80-86.

German, S. R.; Luo, L.; White, H. S.; Mega, T. L. *J. Phys. Chem. C* **2013**, *117*, 703-711.

Goodenough, J. B.; Park, K.-S. *J. Am. Chem. Soc.* **2013**, *135*, 1167-1176.

Gosso, S.; Turturici, M.; Franchino, C.; Colombo, E.; Pasquarelli, A.; Carbone, E.; Carabelli, V. *J. Physiol.*, **2014**, *592*, 3215–3230.

Goyal, G.; Darvish, A.; Kim, M. J. *Analyst* **2015**, *140*, 4865-4873.

Grzywna, Z. J.; Siwy, Z.; Bashford, C. L. *J. Membrane Sci.* **1996**, *121*, 261−269.

Guerrette, J. P.; Oja, S. M.; Zhang, B. *Anal. Chem.* **2012**, *84*, 1609-1616.

Guerrette, J. P.; Percival, S. J.; Zhang, B. *J. Am. Chem. Soc.* **2013**, *135*, 855-861.

Guerrette, J. P.; Percival, S. J.; Zhang, B. *Langmuir* **2011**, *27*, 12218–12225.

Guerrette, J. P.; Zhang, B. *J. Am. Chem. Soc.* **2010**, *132*, 17088−17091.

Gutes, A.; Laboriante, I.; Carraro, C.; Maboudian, R. *J. Phys. Chem. C* **2009**, *113*, 16939-16944.

Hafez, I.; Kisler, K.; Berberian, K.; Dernick, G.; Valero, V.; Yong, M. G.; Craighead, H. G.; Lindau, M. *Proc. Natl. Acad. Sci. U. S. A.* **2005**, *102*, 13879–13884.

Harms, Z. D.; Mogensen, K. B.; Nunes, P. S.; Zhou, K.; Hildenbrand, B. W.; Mitra, I.; Tan, Z.; Zlotnick, A.; Kutter, J. P.; Jacobson, S. C. *Anal. Chem.* **2011**, *83*, 9573−9578.

Heerema, S. J.; Dekker, C. *Nat. Nanotechnol.* **2016**, *11*, 127−136.

Heins, E. A.; Siwy, Z. S.; Baker, L. A.; Martin, C. R. *Nano Lett.* **2005**, *5*, 1824−1829.

Heinze, J. *Angew. Chem. Int. Ed. Engl.* **1993**, *32*, 1268-1288.

Holden, D. A.; Hendrickson, G. R.; Lan, W-J.; Lyon, L. A.; White, H. S. *Soft Matter* **2011**, *7*, 8035-8040.

Holden, D. A.; Hendrickson, G.; Lyon, L. A.; White, H. S. *J. Phys. Chem. C* **2011**, *115*, 2999-3004.

Holden, D. A.; Watkins, J. J.; White, H. S. *Langmuir* **2012**, *28*, 7572-7577.

Howell, J. O.; Wightman, R. M. *Anal. Chem.* **1984**, *56*, 524–529.

Huang, X-J.; O'Mahony, A. M.; Compton, R. G. *Small* **2009**, *5*, 776–788.

Ito, T.; Sun, L.; Crooks R. M. *Anal. Chem.* **2003**, *75*, 2399−2406.

Ito, T.; Sun, L.; Henriquez, R. R.; Crooks, R. M. *Acc. Chem. Res.* **2004**, *37*, 937−945.

Jena, B. K.; Raj, C. R. *Anal. Chem.* **2008**, *80*, 4836–4844.

Jonas, E. A.; Knox, R. J.; Kaczmarek, L. K. *Neuron* **1997**, *19*, 7-13.

Kennedy, E.; Dong, Z.; Tennant, C.; Timp, G. *Nat. Nanotech.* **2016**, *11*, 968−976.

Killick, R.; Eckley, I. A. *J. Stat. Soft.* **2014**, *58*, 1-19.

Kim, B.-K.; Boika, A.; Kim, J.; Dick, J. E.; Bard, A. J. *J. Am. Chem. Soc.* **2014**, *136*, 4849−4852.

Kwak, J.; Bard, A. J. *Anal. Chem.* **1989**, *61*, 1221-1227.

Kwok, H.; Briggs, K.; Tabard-Cossa, V. *PLoS ONE* **2014**, *9*, e92880.

Lan, W. J.; Holden, D. A.; Liu, J.; White, H. S. *J. Phys. Chem. C* **2011**, *115*, 18445-18452.

Lan, W. J.; Kubeil, C.; Xiong, J. W.; Bund, A.; White, H. S. *J. Phys. Chem. C* **2014,** *118* (5), 2726-2734.

Lan, W.-J. Holden, D. A.; Zhang, B.; White, H. S. *Anal. Chem.* **2011**, *83*, 3840-3847.

Lanyon, Y. H.; De Marzi, G.; Watson, Y. E.; Quinn, A. J.; Gleeson, J. P.; Redmond, G.; Arrigan, D. W. M. *Anal. Chem.* **2007**, *79*, 3048-3055.

Lee, M. H.; Kumar, A.; Park, K. B.; Cho, S. Y.; Kim, H. M.; Lim, M. C.; Kim, Y. R.; Kim, K. B. *Sci. Rep.* **2014**, *4*, 7448.

Lesch, A., Momotenko, D.; Cortés-Salazar, F.; Wirth, I.; Tefashe, U.M.; Meiners, F.; Vaske, B.; Girault, H.H.; Wittstock, G. *J. Electroanal. Chem*. **2012**, *666*, 52–61.

Levis, R. A. and Rae, J. L. *Biophys J.* **1993**, *65*, 1666–1677.

Li, G.; Zhang, Z.; Lin, X. *Chin. J. Anal. Chem*. **2010**, *38*, 1698−1702.

Li, J.; Stein, D.; McMullan, C.; Branton, D.; Aziz, M. J.; Golovchenko, J. A. *Nature* **2001**, *412*, 166−169.

Li, W.; Gong, L.; Bayley, H. *Agnew. Chem. Int. Ed*. **2013**, *52*, 4350−4355.

Li, Y.; Bergman, D.; Zhang, B. *Anal. Chem.* **2009**, *81*, 5496–5502.

Lima, A. E. B.; Luz, G. E.; Batista, N. C.; Longo, E.; Cavalcante, L. S.; Santos, R. S. *Electroanal*. **2015**, *28*, 985–989.

Liu, H.-Y.; Fan, F.-R. F.; Lin, C. W.; Bard, A. J. *J. Am. Chem. Soc.* **1986**, *108*, 3838-3839.

Lu, J.; Zhang, B. *Anal. Chem.* **2017**, *89*, 2739-2746.

Luo, L.; German, S. R.; Lan, W.-J.; Holden, D. A.; Mega, T. L.; White, H. S. *Annu. Rev. Anal. Chem.* **2014**, *7*, 513-535.

Luo, L.; White, H. S. *Langmuir* **2013**, *29*, 11169-11175.

Magagnin, L.; Maboudian, R.; Carraro, C. *J. Phys. Chem. B* **2002**, *106*, 401-407.

Manrao, E. A.; Derrington, I. M.; Laszlo, A. H.; Langford, K. W.; Hopper, M. K.; Gillgren, N.; Pavlenok, M.; Niederweis, M.; Gundlach, J. H. *Nat. Biotechnol*. **2012**, *30*, 349−354.

Masterton, W. L.; Bolocofsky, D.; Lee, T. P. *J. Phys. Chem.* **1971**, *18*, 2809-2815.

Menon, V. P.; Martin, C. R. *Anal. Chem.* **1995**, *67*, 1920–1928.

Menshykau, D.; Huang, X-J.; Rees, N. V.; del Campo, F. J.; Muñoz, F. X.; Compton, R. G. *Analyst* **2009**, *134*, 343–348.

Mirkin, M. V.; Bard, A. J *Anal. Chem.* **1992**, *64*, 2293– 2302.

Miyake, H.; Ye, S.; Osawa, M. *Electrochem. Commun.* **2002**, *4*, 973-977.

Moeller, K. D. *Tetrahedron* **2000**, *49*, 9527-9554.

Moretto, L. M.; Pepe, N. Ugo, P. *Talanta* **2004**, *62*, 1055–1060.

Morita, M.; Ohmi, T.; Kawakami, H. M.; Ohwada, M. *J. Appl. Phys.* **1990**, *68*, 1272-1281.

Movileanu, L. *Soft Matter* **2008**, *4*, 925−931.

Murray, R. W. *Chem. Rev.* **2008**, *108*, 2688−2720.

Nam, Y.; Chang, J. C.; Wheeler, B. C.; Brewer, G. J. *IEEE Trans. Biomed. Eng.* **2004**, *51*, 158−165.

Oja, S. M.; Fan, Y. S.; Armstrong, C. M.; Defnet, P.; Zhang, B. *Anal. Chem.* **2016**, *88*, 414-430.

Oja, S. M.; Guerrette, J. P.; David, M. R.; Zhang, B. *Anal. Chem.* **2014**, *86*, 6040-6048.

Oja, S. M.; Wood, M.; Zhang, B. *Anal. Chem.* **2013**, *85*, 473−486.

Oldham, K. B. *J. Electroanal. Chem.* **1992**, *337*, 91–126.

P. H. Rieger, Electrochemistry, p. 215-223, Chapman & Hall, Inc., New York, (1994).

Penner, R. M.; Martin, C. R. *Anal. Chem.* **1987**, *59*, 2625–2630.

Perera, R. T.; Fleming, A. M.; Johnson, R. P.; Burrows, C. J.; White, H. S. *Nanotechnology* **2015**, *26*, 074002.

Perry, D.; Momotenko, D.; Lazenby, R. A.; Kang, M.; Unwin, P. R. *Anal. Chem.* **2016,** *88*, 5523–5530.

Pevarnik, M.; Healy, K.; Toimil-Molares, M. E.; Morrison, A.; Létant, S. E.; Siwy, Z. S. *ACS Nano* **2012**, *6*, 7295−7302.

Piper, J. D.; Clarke, R.W.; Korchev, Y. E,; Ying, L. M,; Klenerman, D. *J. Am. Chem. Soc.* **2006**, *128*, 16462–16463.

Potts, P. J. *A Handbook of Silicate Rock Analysis*; Chapman and Hall: London, 1987.

Pust, S. E.; Salomo, M.; Oesterschulze, E.; Wittstock, G. *Nanotechnology* **2010**, *21*, 105709-105721.

Qiu, Y.; Dawid, A.; Siwy, Z. S. *J. Phys. Chem. C* **2017**, *121*, 6255−6263.

Qiu, Y.; Hinkle, P.; Yang, C.; Bakker, H. E.; Schiel, M.; Wang, H.; Siwy, Z. S. *ACS Nano* **2015,** *9* (4), 4390-4397.

Quinn, B. M.; Dekker, C.; Lemay, S. G. *J. Am. Chem. Soc*. **2005**, *127*, 6146–6147.

Randles, J. E. B. *Trans. Faraday Soc*. **1948**, *44*, 322–327.

Salomo, M.; Pust, S. E.; Wittstock, G.; Oesterschulze, E. *Microelectron. Eng.* **2010**, *87*, 1537-1539.

Ševčík, A. *Collect. Czech. Chem. Commun*. **1948**, *13*, 349–377.

Shao, Y. H.; Mirkin, M. V.; Fish, G.; Kokotov, S.; Palanker, D.; Lewis, A. *Anal. Chem.* **1997**, *69*, 1627-1634.

Shi, W.; Friedman, A. K.; Baker, L. A. *Anal. Chem.* **2017**, *89*, 157−188.

Smeets, R. M. M.; Dekker, N. H.; Dekker, C. *Nanotechnology* **2009**, *20*, 095501.

Smeets, R. M. M.; Keyser, U. F.; Dekker, N. H.; Dekker, C. *Proc. Nat. Acad. Sci. U.S.A.* **2008**, *105*, 417−421.

Somerville, J. A.; Willmott, G. R.; Eldridge, J.; Griffiths, M.; McGrath, K. M. *J. Colloid Interface Sci.* **2013**, *394*, 243-251.

Spira, M. E.; Hai, A. *Nat. Nanotechnol*. **2013**, *8*, 83–94.

Sripirom, J.; Noor, S.; Köhler, U.; Schulte, A. *Carbon* **2011**, *49*, 2402-2412.

Storm, A. J.; Chem, J. H.; Ling, X. S.; Zandbergen, H. W.; Dekker, C. *Nat. Mater.* **2003**, *2*, 537−540.

Strein, T. G.; Ewing, A. G. *Anal. Chem.* **1992**, *64*, 1368-1373.

Tabard-Cossa, V.; Trivedi, D.; Wiggin, M.; Jetha, N. N.; Marziali, A. *Nanotechnology* **2007**, *18*, 305505.

Tsutsui, M.; Hongo, S.; He, Y.; Taniguchi, M.; Gemma, N.; Kawai, T. *ACS Nano* **2012**, *6*, 3499−3505.

Ugo, P.; Pepe, N.; Moretto, L. M.; Battagliarin, M. J. *Electroanal. Chem.* **2003**, *560*, 51–58.

van Beek, W. M., Mandel, M. *J. Chem. Soc., Faraday Trans. 1* **1977**, 74, 2339−2351.

van Wolferen, H.; Abelmann, L. Laser Interference Lithography. In *Lithography: Principles, Processes, and Materials;* Hennessey, T. A., Nova Science Publishers, 2011.

Velický, M.; Tam, K. Y.; Dryfe, R. A. W. *Anal. Chem.* **2013**, *86*, 435-442.

Wang, J.; Ewing, A. G. *Analyst* **2014**, *139*, 3290–3295.

Wang, J.; Trouillon, R.; Lin, Y.; Svensson, M. I.; Ewing, A. G. *Anal. Chem*. **2013**, *85*, 5600–5608.

Watkins, J. J.; Chen, J.; White, H. S.; Abruña, H. D.; Maisonhaute, E.; Amatore, C. *Anal. Chem.* **2003**, *75*, 3962– 3971.

Wehmeyer, K. R.; Deakin, M. R.; Wightman, R. M. *Anal. Chem.* **1985**, *57*, 1913-1916.

Wei, C.; Bard, A. J.; Feldberg, S. W. *Anal. Chem.* **1997**, *69*, 4627−4633.

Wigström, J.; Dunevall, J.; Najafinobar, N.; Lovrić, J.; Wang, J.; Ewing, A. G.; Cans, A.-S. *Anal. Chem.* **2016**, *88*, 2080–2087.

William, K. R.; Gupta, K.; Wasilik, M. *J. Microelectromech. S.* **2003**, *6*, 761-778.

Wu, Y. C.; Koch, W. F.; Pratt, K. W. *J. Res. Natl. Inst. Stand. Technol.* **1991**, *96*, 191-201.

Xiao, X. Y.; Bard, A. J. *J. Am. Chem. Soc.* **2007**, *129*, 9610-9612.

Yang, C.; Hinkle, P.; Menestrina, J.; Vlassiouk, I. V.; Siwy, Z. S. *J. Phys. Chem. Lett.* **2016**, *7*, 4152−4158.

Yusko, E. C.; An, R.; Mayer, M. *ACS Nano*, **2010**, *4*, 477–487.

Zhang, B.; Galusha, G.; Shiozawa, P. G.; Wang, G.; Bergren, A. J.; Johns, R. M.; White, R. J.; Ervin, E. N.; Cauley, C. C.; White, H. S. *Anal. Chem.* **2007**, *79*, 4778−4787.

Zhang, B.; Wood, M.; Lee, H. *Anal. Chem.* **2009**, *81*, 5541−5548.

Zhang, B.; Zhang, Y.; White, H. S. *Anal. Chem*. **2004**, *76*, 6229–6438.

Zhang, B.; Zhang, Y.; White, H. S. *Anal. Chem*. **2006**, *78*, 477–483.

Zhang, B.; Adams, K. L.; Luber, S. J.; Eves, D. J.; Heien, M. L.; Ewing, A. G. *Anal. Chem.* **2008**, *80*, 1394–1400.

Zhou, K.; Li, L.; Tan, Z.; Zlotnick, A.; Jacobson, S. C. *J. Am. Chem. Soc*. **2011**, *133*, 1618−1621.

Vita

Christopher G. Gunderson was born and raised in New Jersey before moving to Massachusetts in his final year of high school. After high school, he attended Middlesex Community College in Bedford, MA where he obtained his A. A. in liberal arts and sciences. His achievement at community college allowed him to attend the University of Massachusetts in Amherst, MA where he graduated with two B. S. degrees in chemistry and physics. After graduating, he worked for a year as a scientist at a biomedical company working with electrochemical biosensors. In 2012, he moved to Seattle, WA to attend the University of Washington where he has worked under Professor Bo Zhang to learn about nanoscale electrochemistry while earning a Ph. D in chemistry.